ABSTRACT

THE ASYMMETRY PARAMETER AND BRANCHING RATIO OF SIGMA PLUS RADIATIVE DECAY

Maurice Emile Foucher

Yale University

May 1992

We have measured the asymmetry parameter and branching ratio of the Σ^+ radiative decay. This high statistics experiment (FNAL 761) was performed in the Proton Center charged hyperon beam at Fermi National Accelerator Laboratory in Batavia, Illinois. We find for the asymmetry parameter -0.720 $\pm$ 0.086 $\pm$ 0.045 where the first error is statistical and the second is systematic. This result is based on a sample of 34754 $\pm$ 212 events. We find a preliminary value for the branching ratio $Br(\Sigma^+ \rightarrow p\gamma)/Br(\Sigma^+ \rightarrow p\pi^0) = (2.14 \pm 0.07 \pm 0.11) \times 10^{-3}$ where the first error is statistical and the second is systematic. This result is based on a sample of 31040 $\pm$ 650 events. Both results are in agreement with previous low statistics measurements.

E761

THE ASYMMETRY PARAMETER AND BRANCHING RATIO OF SIGMA PLUS RADIATIVE DECAY

A Dissertation
Presented to the Faculty of the Graduate School
of
Yale University
in Candidacy for the Degree of
Doctor of Philosophy

By
Maurice Emile Foucher
May 1992

Acknowledgements

I wish to thank all of the people who have helped me in achieving this goal. There are so many I cannot possible mention them all here, but I will try.

I wish to thank my advisor Peter Cooper without whose inspiration and patiences this work would never have been completed. He was always an infinite source of ideas.

I wish to thank the rest my thesis committee, Prof. Alan Chodos, Prof. Frank Firk, Prof. Jack Sandweiss and Prof. Michael Zeller. They gave me many helpful suggestions about the thesis. I also like to thank my outside reader Prof. James Russ.

I would like to thank the E761 collaboration. I would like to thank my fellow graduate Antonio Morelos, Ivone Freire Albuquerque and Roberto Mahon. Of course special thanks go to my favorite setter Dong Chen and my bridge partner Tim Dubbs. Both of whom put up with my "crabbiness" over the years. They also made many suggestions to improve the thesis. Special acknowledgement to Philippe Gouffon for all your help over the years. Your help with error analysis and computers has been invaluable. Special thanks to Alexander "Sasha" Denisov for help in the design and building of the trigger. I would also like to thank Joseph Lach and Nicolai Terentyev for all of their help over the years. They have been a source of inspirations and ideas throughout the completion of this work.

I would like to thank all of the special friends that I have met during this work. Very special thanks to Alma Karas. Thanks go to Frank Rotondo for many years of friendship and help throughout my graduate career. I would like to thank all the people from Monday and Friday night (actually sometimes it was every night) volleyball. If nothing else my hitting has improved over the years.

Thanks to my sister and brother-in-law, Helen and Kenneth Hamel. We had so

many good times over the years. So much grazing so little time.

This thesis is dedicated to my parents Rose and Emile Foucher, who gave me the greatest gift of all. They were always encouraging me to do my best. My only wish is that they were here to see what I have accomplished. Thanks, Ma and Dad.

Contents

Acknowledgements ii

List of Figures v

List of Tables vii

1 Introduction 1

1.1 Theoretical Background 4

1.2 Previous Experiments 20

1.2.1 Asymmetry Parameter $\Sigma^+ \rightarrow p\gamma$ 20

1.2.2 Branching Ratio $\Sigma^+ \rightarrow p\gamma$ 24

1.3 Summary 25

2 Experimental Apparatus 27

2.1 Introduction 27

2.2 Proton Center Beamline 28

2.3 Hyperon Magnet and Channel 29

2.4 Hyperon Spectrometer 33

2.5 Baryon Spectrometer 34

2.6 Missing Neutral Mass Squared Resolution 35

2.7 Photon Spectrometer 35

3 Trigger and Data Acquisition System (DAQ) 44

3.1 Trigger 45

3.1.1 T1 45
3.1.2 T2 46
3.1.3 T3 50
3.1.4 Trigger Hardware 51
3.2 DAQ 52
3.3 Summary 53

4 Data Analysis **54**
4.1 Outline 54
4.2 Alignment 54
4.3 Momentum Calibration 56
4.4 Target Reconstruction 56
4.5 Photon Calorimeter Calibration 57
4.6 Pass1 Reconstruction 57
4.7 Data Samples 63

5 Asymmetry Parameter $\Sigma^+ \rightarrow p\gamma$ **66**
5.1 Bias Cancelling Technique 66
5.2 A_0^y, Asymmetry of $\Sigma^+ \rightarrow p\pi^0$ 70
5.3 A_γ^y, Asymmetry of $\Sigma^+ \rightarrow p\gamma$ 72
5.4 Systematic Error 84
5.4.1 A_B^z, z false asymmetry in background 84
5.4.2 TRD algorithm 87
5.4.3 Bias cancelling binning 88
5.4.4 Variation of the cuts 88

6 Branching Ratio $\Sigma^+ \rightarrow p\gamma$ **95**
6.1 Number of $\Sigma^+ \rightarrow p\pi^0$ 96
6.2 Efficiency for $\Sigma^+ \rightarrow p\pi^0$ and $\Sigma^+ \rightarrow p\gamma$ 97
6.3 Number of $\Sigma^+ \rightarrow p\gamma$ 104
6.4 Efficiency of TRD algorithm 107
6.5 Branching ratio $\Sigma^+ \rightarrow p\gamma$ 109

7 Conclusion **111**

List of Figures

1.1 Hyperon radiative decays in spin $\frac{1}{2}$ octet and spin $\frac{3}{2}$ decuplet. 2

1.2 Pole model diagrams for hyperon radiative decays. 5

1.3 K^* pole diagram used by Nardulli [21]. V is a low mass vector meson such as ρ, ω, or ϕ. 6

1.4 Hyperon radiative decay, single quark transition s $\rightarrow$ dγ. 9

1.5 Single quark transition considered by Gilman and Wise [22]. 10

1.6 2-quark transition where the photon can be radiated from any line. . 11

1.7 3-quark transition. 11

1.8 2-quark transitions calculated by Lo Chong-Huah [24]. 12

1.9 Photo-penguin diagram in hyperon radiative decays. 15

1.10 Penguin diagram analyzed by Gaillard, Li and Rudaz. 16

1.11 Żenczykowski's combined symmetry/vector dominance model approach of relating $Y \rightarrow B + \gamma$ to $Y \rightarrow B + \pi$. For hyperon radiative decays the photon couples to the vector mesons, ρ, ω, or ϕ. 19

1.12 Missing-mass-squared distribution, m_x^2 assuming $\Sigma^+ \rightarrow p + x$. from Gershwin *et al* [5]. 20

1.13 Missing-mass-squared distribution, m_x^2 assuming $\Sigma^+ \rightarrow p + x$. from Manz *et al* [4]. 21

1.14 Acoplanarity and dip angle used to isolate $\Sigma^+ \rightarrow p\gamma$ from Kobayashi *et al* [3]. 22

1.15 Dip angle distributions for two sets of data with positive $\cos\theta_p$ and negative $\cos\theta_p$. (θ_p is the center of mass angle between the Σ^+ polarization direction and the proton momentum. From Kobayashi *et al* [3]. . . . 23

1.16 α_γ for $\Sigma^+ \rightarrow p\gamma$ from previous experiments. 24
1.17 Br($\Sigma^+ \rightarrow p\gamma$) from previous experiments, in units of 10^{-3}. 26

2.1 Schematic diagram (plan view) of PC3 enclosure. Positive targeting angle is shown. 28
2.2 E761 experiment (plan view) in Proton Center enclosure 4 (PC4). . . 30
2.3 The one interaction length Cu target. 31
2.4 The hyperon magnet channel [48] used to define the hyperon beam. The channel was embedded inside the hyperon magnet. Figure taken from reference [48]. 32
2.5 The hyperon spectrometer (plan view) used to measure the Σ^+ track. 33
2.6 The baryon spectrometer (plan view) used to measure the proton track. 34
2.7 The photon spectrometer. A photon showers in the steel plates. The position of the photon is measured in PWC and TRD. The photon energy is measured in a lead glass, BGO calorimeter. 36
2.8 Schematic cross section of one module of TRD. Not drawn to scale. . 37
2.9 Average number of transition radiation X-rays, N_γ, detected per module of TRD as a function of Lorentz γ factor for e^- and π^- [49]. . . . 39
2.10 The front lead glass wall. The hole is to let protons pass through. . . 40
2.11 The main lead glass array with BGO lining the hole. The hole lets protons pass through. 42
2.12 The rear lead glass array used to measure the energy of photons that went into the hole of the main lead glass array. 43

3.1 The position of the T1 trigger scintillators within the hyperon spectrometer. T1 was defined as $T1 \equiv B1 \cdot B2 \cdot B3 \cdot \overline{VH2 + VH3}$. 45
3.2 The position of the T2 trigger scintillation counters within the photon spectrometer at the start of the run. Not drawn to scale. 47
3.3 The final position of the T2 trigger scintillators within the photon spectrometer. Not drawn to scale. 48

3.4 Schematic diagram of the E761 DAQ system. Data from the detectors were readout of CAMAC into ACP nodes. Data were then written to 9-track tape. Some of the data were transferred to a VAX 11/780 for monitoring. 52

4.1 Outline of data analysis scheme. 55

4.2 Distribution of hyperon track reduced χ^2,χ^2_Y/ν. The average number of degrees-of-freedom is $\nu = 4$. The position of the cut is shown by the arrow. 58

4.3 Distribution of baryon track reduced χ^2,χ^2_B/ν. The average number of degrees-of-freedom is $\nu = 25$. The position of the cut is shown by the arrow. 59

4.4 Hyperon momentum (GeV/c) distribution for positive targeting angle. The momentum cut shown by the arrows was made in the analysis. . 59

4.5 Distribution of TY angle (radians) of hyperon for positive(left) and negative(right) targeting angle. 60

4.6 Distribution of TX angle (radians) of hyperon for positive(left) and negative(right) targeting angle. 61

4.7 z vertex(cm) distribution of hyperon with respect to SD3. SD3 is at the origin on this plot. The peak at 1400 cm (WA) is due to decays downstream of WA for which the offline program assigned the wrong z vertex position. We make the cut shown by the arrows. 61

4.8 θ_{op} (radians) - versus - r for a small sample of our data. The curved band is the decay $\Sigma^+ \rightarrow p\pi^0$ 62

4.9 Schematic representation of θ_{op} (mrad) - versus - r plot for expected decay modes in E761. This is NOT data. 64

4.10 Missing-mass-squared (GeV$^2/c^4$) m_x^2 assuming $\Sigma^+ \rightarrow pX$ for our full data sample. There are 48×10^6 $\Sigma^+ \rightarrow p\pi^0$, 67×10^3 $\Sigma^+ \rightarrow p\gamma$ and 250×10^3 $K^+ \rightarrow \pi^+\pi^0$ 65

5.1 Acceptance as a function of $\cos\theta^y$ for $\Sigma^+ \rightarrow p\gamma$. Solid is data and dashed is Monte Carlo. The plots are normalized to equal area. The average acceptance is 64%. 68
5.2 Acceptance as a function of $\cos\theta^y$ for $\Sigma^+ \rightarrow p\pi^0$. Solid is data and dashed is Monte Carlo. The plots are normalized to equal area. The average acceptance is 85%. 68
5.3 x position (cm) of the hyperon track at the target for positive (left) and negative (right) targeting angle for the PRE sample. The cuts shown by the arrows were made. 71
5.4 y position (cm) of the hyperon track at the target for the PRE sample. The cuts shown by the arrows were made. 71
5.5 Missing-mass-squared (GeV^2/c^4) m_x^2 assuming $K^+ \rightarrow \pi^+X$ for the PRE sample. We removed events between the arrows. 72
5.6 Missing-mass-squared (GeV^2/c^4) m_x^2 assuming $\Sigma^+ \rightarrow pX$ for the PRE sample. The cut shown by the arrows was made. 73
5.7 x position (cm) of the hyperon track at the target for positive (left) and negative (right) targeting angle for the PGAM sample. The cuts shown by the arrows were made. 74
5.8 y position (cm) of the hyperon track at the target for the PGAM sample. The cuts shown by the arrows were made. 75
5.9 Missing-mass-squared (GeV^2/c^4) m_x^2 assuming $K^+ \rightarrow \pi^+X$ for the PGAM sample. We removed events between the arrows. 76
5.10 Single event display of half of the photon spectrometer for a $\Sigma^+ \rightarrow p\gamma$ event. The missing-mass-squared in the event is 7.43×10^{-4} GeV^2/c^4. The TRD $\chi^2 = 0.15$. The solid line is the proton track and the dashed line is the missing neutral or photon in this case. 77
5.11 Single event display of half of the photon spectrometer for a $\Sigma^+ \rightarrow p\pi^0$ event. The missing-mass-squared in the event is 0.0164 GeV^2/c^4. The TRD $\chi^2 = 50$. The solid line is the proton track and the dashed line is the missing neutral or π^0 in this case. 78

5.12 TRD χ^2 versus missing-mass-squared m_x^2 (GeV^2/c^4) assuming $\Sigma^+ \rightarrow pX$. There is a clear excess of events at $m_\gamma^2 = 0$. These are $\Sigma^+ \rightarrow p\gamma$. The 4 regions defined are used to extract the A_γ. 81
5.13 M_x^2 (GeV^2/c^4) assuming $\Sigma^+ \rightarrow pX$ for events with TRD $\chi^2 \leq 1$ (solid) and background TRD $\chi^2 \geq 4$. These 2 distributions are normalized to equal area in the region $0.0072 \leq m_x^2 \leq 0.0100$ GeV^2/c^4. 82
5.14 α_γ versus A_B^z. The typical error bars on each point are $\pm$ 0.09 for α_γ and $\pm$ 0.007 for A_B^z. The dashed line is the estimated systematic error from A_B^z. The solid line is our measured value of α_γ. 86
5.15 Number of cases versus α_γ for different number of bins used in the bias cancelling technique. The σ of the distribution is 0.025. 89
5.16 X position of the proton (cm) at the first steel plate in the photon spectrometer for the PGAM sample. This distribution has been divided into 8 bins shown by the lines. 90
5.17 α_γ versus x position of the proton at the first steel plate. The weighted mean is the solid line. The χ^2 for the fit to a constant is 6.44 for $\nu =$ 7 degrees-of-freedom. 91
5.18 Ths χ^2 distribution for variation studies (solid line.) The dashed curve is the expected χ^2 distribution for 17 studies and 7 degrees-of-freedom. The mean of the data is 7.50 $\pm$ 1.14. The mean of the expected curve is 7. 93

6.1 x distribution (cm) of the proton at the first steel plate for positive targeting angle for $\Sigma^+ \rightarrow p\pi^0$. The cut shown by the lines was made. 97
6.2 Missing-mass-squared distribution (GeV^2/c^4) m_x^2, $\Sigma^+ \rightarrow pX$, for positive targeting angle. The linear background is shown. 98
6.3 $\Sigma^+ \rightarrow p\pi^0$ data versus Monte Carlo positive targeting angle, Hyperon reduced χ^2 distribution (left) and baryon reduced χ^2 distribution (right.) Solid is data and dashed is Monte Carlo. We make the cuts and normalization at the arrows. 99

6.4 $\Sigma^+ \rightarrow p\pi^0$ data versus Monte Carlo positive targeting angle, TX (radians) of Σ^+ (left) and TX (radians) of proton (right.) Solid is data and dashed is Monte Carlo. 99
6.5 $\Sigma^+ \rightarrow p\pi^0$ data versus Monte Carlo positive targeting angle, m_x^2 (GeV$^2/c^4$) $\Sigma^+ \rightarrow pX$ (left) and momentum (GeV/c) of Σ^+ (right.) Solid is data and dashed is Monte Carlo. 100
6.6 $\Sigma^+ \rightarrow p\pi^0$ data versus Monte Carlo positive targeting angle, z vertex (cm) distribution (left) and x position (cm) of proton at the first steel plate (right.) Solid is data and dashed is Monte Carlo. We make the cuts and normalization at the arrows. 100
6.7 $\Sigma^+ \rightarrow p\gamma$ data versus Monte Carlo positive targeting angle, Hyperon reduced χ^2 distribution (left) and baryon reduced χ^2 distribution (right.) Solid is data and dashed is Monte Carlo. We make the cuts and normalization at the arrows. 102
6.8 $\Sigma^+ \rightarrow p\gamma$ data versus Monte Carlo positive targeting angle, TX (radians) of proton (left) and momentum (GeV/c) of Σ^+ (right.) Solid is data and dashed is Monte Carlo. 102
6.9 $\Sigma^+ \rightarrow p\gamma$ data versus Monte Carlo positive targeting angle, x position (cm) of proton at the first steel plate. Solid is data and dashed is Monte Carlo. We make the cuts and normalization at the arrows. . . 103
6.10 $\Sigma^+ \rightarrow p\gamma$ data versus Monte Carlo positive targeting angle, TX (radians) of Σ^+. Solid is data and dashed is Monte Carlo. 103
6.11 $\Sigma^+ \rightarrow p\gamma$ data versus Monte Carlo positive targeting angle, z vertex (cm) distribution. Solid is data and dashed is Monte Carlo. We make the cuts and normalization at the arrows. 104
6.12 Position cut on the photon from $\Sigma^+ \rightarrow p\gamma$. The photon had to be inside of 5 cm of the outer edge of the TRD active area and outside of 3 cm of the hole in the steel plate. 105

6.13 Missing-mass-squared distribution (GeV^2/c^4) m_x^2, $\Sigma^+ \rightarrow \mathrm{p}X$, for a TRD $\chi^2 \leq 500$ and local sum cut of 50% for positive targeting angle (data points with error bars.) The fit with gaussian is the curve through the points. 106

6.14 Single photon event topology. The event is a $\Sigma^+ \rightarrow \mathrm{p}\pi^0$, $\pi^0 \rightarrow \gamma_1\gamma_2$ where one photon goes into the rear lead glass array and one photon goes into the photon calorimeter. 108

7.1 Comparison of our asymmetry parameter of $\Sigma^+ \rightarrow \mathrm{p}\gamma$ result with the 3 previous experiments. 112

7.2 Comparison of our branching ratio $\Sigma^+ \rightarrow \mathrm{p}\gamma$ result with the previous experiments. The units are 10^{-3}. 112

List of Tables

1.1 A summary of hyperon radiative decay data. 3

1.2 Theoretical predictions for the branching ratios of radiative decays of hyperons (units of 10^{-3}) in the pole model. 7

1.3 Theoretical predictions for the asymmetry parameters of radiative decays of hyperons in the pole model. 8

1.4 Gilman and Wise [22] predictions for hyperon radiative decay branching ratios. 10

1.5 Kamal and Verma [25] predictions for hyperon radiative decay branching ratios (units of 10^{-3}) and asymmetries. The symbol * means the value was used as input. 13

1.6 Predicted branching ratios (units of 10^{-3}) from Verma and Sharma [26]. These results included both single and two-quark transitions. 14

1.7 Predicted asymmetries from Verma and Sharma [26]. These results included both single and two-quark transitions. 14

1.8 Predictions of Gaillard, Li and Rudaz [34]. 16

1.9 QCD sum rule predictions for branching ratios of hyperon radiative decays in units of 10^{-3}. 17

1.10 QCD sum rule predictions for asymmetry parameters of hyperon radiative decays. 17

1.11 Best results of fit to hyperon radiative decay data from the combined symmetry/vector dominance model of Żenczykowski [39]. The branching ratios are in units of 10^{-3}. 18

5.1 Asymmetries of $\Sigma^+ \rightarrow p\pi^0$, A_0. 73

5.2 Definition of the 4 regions S, B, N and T. 80
5.3 Asymmetry components for each sample. The Σ^+ polarization is in the y direction so that A^x and A^z are false asymmetries which should be 0. 83
5.4 α_γ for different TRD algorithms. 87
5.5 List of χ^2 for variation of α_γ with the cuts listed. The number of degrees-of-freedom is $\nu = 7$. 92
5.6 The four contributions to the systematic error of α_γ. The resultant systematic error is just the four errors added in quadrature, $\pm$ 0.045. 92

6.1 The branching ratio $Br(\Sigma^+ \rightarrow p\gamma)/Br(\Sigma^+ \rightarrow p\pi^0)$ for positive and negative targeting angle. 109

Chapter 1

Introduction

Hyperon radiative decays represent a class of baryon decays which require strong, weak and electromagnetic contributions. These decays allow us to test the interplay of weak and electromagnetic interactions as applied to the underlying quark structure of baryons. The mechanism of these decays is related to other topics of interest in particle physics today for example the $\Delta I = \frac{1}{2}$ rule and the ϵ'/ϵ ratio in neutral kaon decays. The non-leptonic Hamiltonian for these classes of problems are closely related. Any information determined about one class may shed light on the other problems.

There are 7 electroweak ($\Delta S = 1$) radiative decays. Drawn in Fig. 1.1 are the 7 hyperon radiative decay transitions in terms of the spin $\frac{1}{2}$ octet and spin $\frac{3}{2}$ decuplet. The decay $\Sigma^0 \rightarrow n\gamma$ is not included because it is experimentally inaccessable. The decay is overwhelmed by the purely electromagnetic transition $\Sigma^0 \rightarrow \Lambda\gamma$.

We measure two quantities in hyperon radiative decays, the branching ratio, BR and the asymmetry parameter, α. Consider, for example the decay $\Sigma^+ \rightarrow p\gamma$. The branching ratio is the probability that a Σ^+ will decay to $p\gamma$ compared to all other decays modes. If the initial Σ^+ is polarized the asymmetry parameter or α parameter can be measured from the angular distribution of the decay proton. The α parameter measures the correlation between the direction of emission of the proton and the initial hyperon polarization direction. In the rest frame of the polarized Σ^+, the

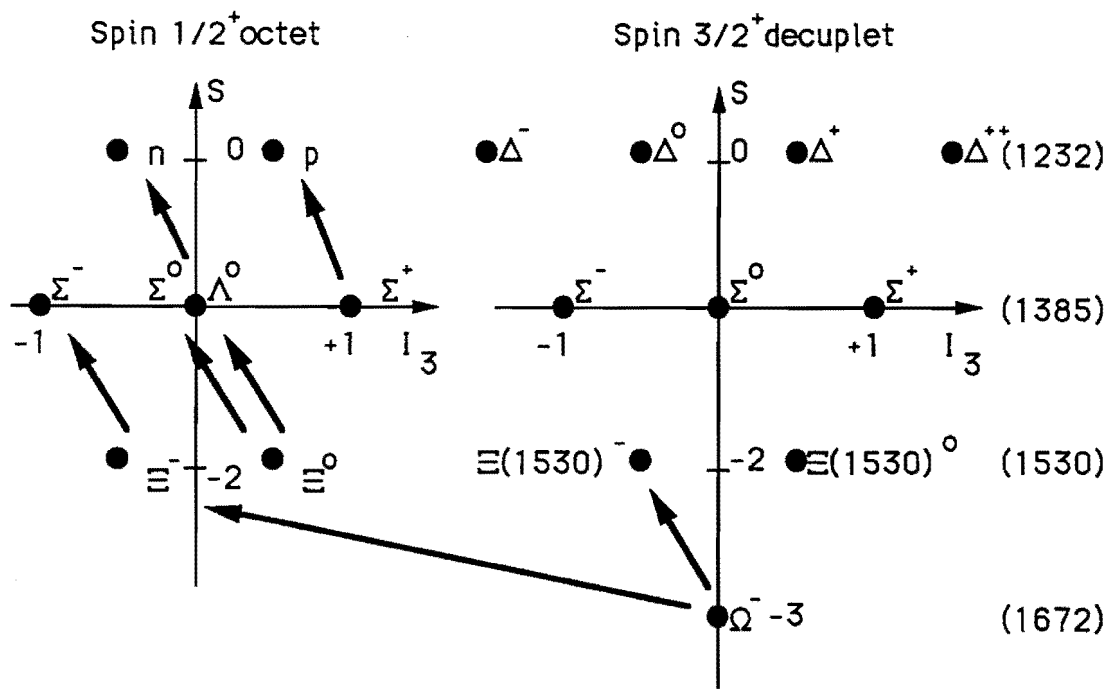

Figure 1.1: Hyperon radiative decays in spin $\frac{1}{2}$ octet and spin $\frac{3}{2}$ decuplet.

angular distribution of the decay proton is given [1] by

$$\frac{dN}{d\Omega} = \frac{N}{4\pi}(1 + \alpha_\gamma \vec{P}_\Sigma \cdot \hat{p}) \tag{1.1}$$

where N is the number of events, Ω is the solid angle into which the decay proton is emitted, α_γ is the $\Sigma^+ \rightarrow p\gamma$ decay asymmetry parameter, $\vec{P}_\Sigma$ is the polarization of the Σ^+ and $\hat{p}$ is a unit vector in the direction of the proton momentum in the Σ^+ rest frame.

The experimental data on hyperon radiative decays is meager. Shown in Table 1.1 is a review of the current experimental status of hyperon radiative decays from the Particle Data Group [2]. For the decay with the largest data sample, $\Sigma^+ \rightarrow p\gamma$, there are 297 events total from 3 experiments [3, 4, 5] for the α parameter, and a total of 899 events from 7 experiments [3, 4, 5, 6, 7, 8, 9] measuring the branching ratio. One problem associated with these experiments is the small branching ratio for the decays. For example the branching ratio for $\Sigma^+ \rightarrow p\gamma$ is 1.25×10^{-3}. This makes it difficult to produce high-precision results. Even more challenging is that the primary background in the decay $\Sigma^+ \rightarrow p\gamma$ is $\Sigma^+ \rightarrow p\pi^0$ with $\pi^0 \rightarrow \gamma\gamma$. The branching ratio

decay	branching ratio	total events	α	total events
$\Sigma^+ \rightarrow p\gamma$	$1.25 \pm 0.07 \times 10^{-3}$	899	-0.83 ± 0.12	297
$\Xi^- \rightarrow \Sigma^-\gamma$	$2.3 \pm 1.0 \times 10^{-4}$	9		
$\Xi^0 \rightarrow \Lambda\gamma$	$1.06 \pm 0.16 \times 10^{-3}$	116	+0.43 ± 0.44	87
$\Xi^0 \rightarrow \Sigma^0\gamma$	$3.56 \pm 0.43 \times 10^{-3}$	85	+0.20 ± 0.32	85
$\Lambda \rightarrow n\gamma$	$1.02 \pm 0.33 \times 10^{-3}$	24		
$\Omega^- \rightarrow \Xi^-\gamma$	$<2.2 \times 10^{-3}$			
$\Omega^- \rightarrow \Xi(1530)^-\gamma$				

Table 1.1: A summary of hyperon radiative decay data.

for this decay mode occurs at a rate 400 times that of $\Sigma^+ \rightarrow p\gamma$. The background has similar kinematics and differs from the decay $\Sigma^+ \rightarrow p\gamma$ by only the addition of one photon. The α parameter [2] in the radiative decay $\Sigma^+ \rightarrow p\gamma$ is α_γ = -0.83 ± 0.12. The α parameter [2] in the hadronic decay $\Sigma^+ \rightarrow p\pi^0$ is α_0 = -0.980 ± 0.016. This raises the concern that a small excess of hadronic background in the $\Sigma^+ \rightarrow p\gamma$ sample could produce a negative asymmetry parameter for $\Sigma^+ \rightarrow p\gamma$.

In general theorists have had great difficulty in reproducing both the observed branching ratios and asymmetry parameters of the hyperon radiative decays. The decays have been analyzed using pole models, single quark transitions, 2-quark transitions, 3-quark transitions, symmetry principles, penguins and QCD sum rules.

In 1985 (when this experiment was proposed) there were only two measurements of the asymmetry parameter of $\Sigma^+ \rightarrow p\gamma$, Gershwin *et al* [5] and Manz *et al* [4]. Their combined value of the asymmetry parameter of $\Sigma^+ \rightarrow p\gamma$ was -0.72 ± 0.29 based on a total of 107 events. Their result suggested a large negative asymmetry parameter but with a large statistical error. At the time, basic symmetry principles were used to predict that the asymmetry parameter should be 0. In 1987, while this experiment was being prepared, Kobayashi *et al* [3] published a result for the asymmetry parameter of $\Sigma^+ \rightarrow p\gamma$ of -0.86 ± 0.13 (statistical) ± 0.04 (systematic), based on 190 events. This experiment still had low statistics therefore raising the concern of possible contamination from the decay $\Sigma^+ \rightarrow p\pi^0$.

For these reasons, Fermilab experiment 761 [10] was performed to study three of these hyperon radiative decays, $\Sigma^+ \rightarrow p\gamma$, $\Xi^- \rightarrow \Sigma^-\gamma$ and $\Omega^- \rightarrow \Xi^-\gamma$. The primary goal of the experiment was a high-statistics measurement of the asymmetry parameter of $\Sigma^+ \rightarrow p\gamma$. Results for the asymmetry parameter (α parameter) and the branching ratio for $\Sigma^+ \rightarrow p\gamma$ are presented in this work.

1.1 Theoretical Background

The transition matrix element, T, for a general radiative decay

$$Y(p) \rightarrow B(p') + \gamma(q)$$

where Y is a hyperon of momentum p, B is a baryon of momentum p' and γ is a photon of momentum q is given by [11]

$$T \propto \epsilon_\nu \bar{u}(p')(A + B\gamma_5)\sigma_{\mu\nu} q_\mu u(p)$$

where $\bar{u}(p')$ and $u(p)$ are the spinor wave functions of the hyperon and baryon, respectively, ϵ_ν is the polarization vector of the photon, A and B are the parity-conserving and parity-violating amplitudes, $\sigma_{\mu\nu}$ is the antisymmetric combination of two Dirac gamma matrices and γ_5 is the usual product of Dirac gamma matrices. The decay rate, Γ, can be written in terms of the two amplitudes A and B, in units where $\hbar =$ c $= 1$, as

$$\Gamma = \frac{G_F^2 e^2 q^2}{\pi}(|A|^2 + |B|^2)$$

where G_F is the Fermi coupling constant and e is the electric charge. The asymmetry parameter, α is given by

$$\alpha = \frac{2\mathrm{Re}(A^* B)}{|A|^2 + |B|^2}$$

The asymmetry parameter measures the interference between the parity-conserving and parity-violating amplitudes. If either one of these is zero then the asymmetry parameter is zero.

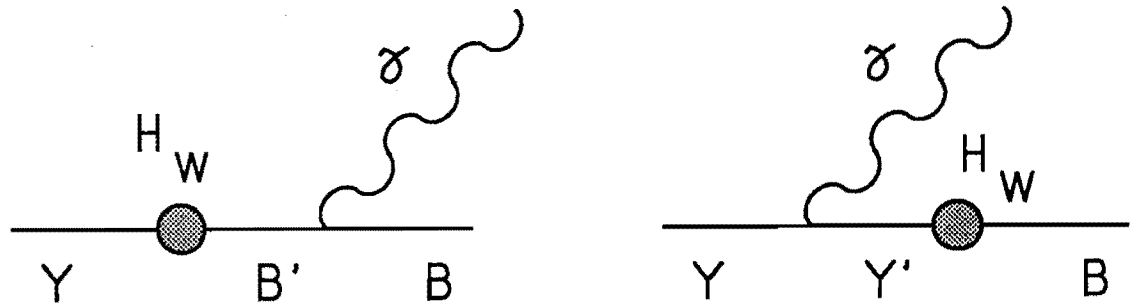

Figure 1.2: Pole model diagrams for hyperon radiative decays.

Symmetry principles can be used to impose important constraints on hyperon radiative decays. Hara [12] showed, in 1964, that the parity-violating amplitude, B, is zero under the following assumptions: CP conservation, U-spin symmetry and left-handed current-current form of the weak interaction. Therefore $\alpha = 0$ for both $\Sigma^+ \rightarrow p\gamma$ and $\Xi^- \rightarrow \Sigma^-\gamma$. If we relax U-spin symmetry and take into account the mass difference between the s and d quarks [13] the alpha parameter can be written as

$$\alpha = \frac{m_s^2 - m_d^2}{m_s^2 + m_d^2} \sim +0.5$$

where m_s and m_d are the mass of the s and d quarks respectively. This prediction contradicts current experimental results.

The first attempt to calculate a branching ratio and asymmetry parameter for hyperon radiative decays used the pole model. Shown in Fig. 1.2 are the pole model diagrams that contribute to hyperon radiative decays. In this model, one separates the decay into an electromagnetic vertex and a weak vertex, H_W. The intermediate states Y′ and B′ are spin $\frac{1}{2}$ baryons with positive or negative parity assuming Y and B are spin $\frac{1}{2}$ baryons. Under SU(3) flavor symmetry, intermediate states of positive parity contribute to the parity-conserving amplitude, A, and negative parity states to the parity-violating amplitude, B. The parameters used in pole model calculations are the baryon non-leptonic transition matrix elements, baryon magnetic moments and the photo-production matrix elements for the electromagnetic transition. See Table 1.2 for a summary of the pole model predictions for the branching ratios of

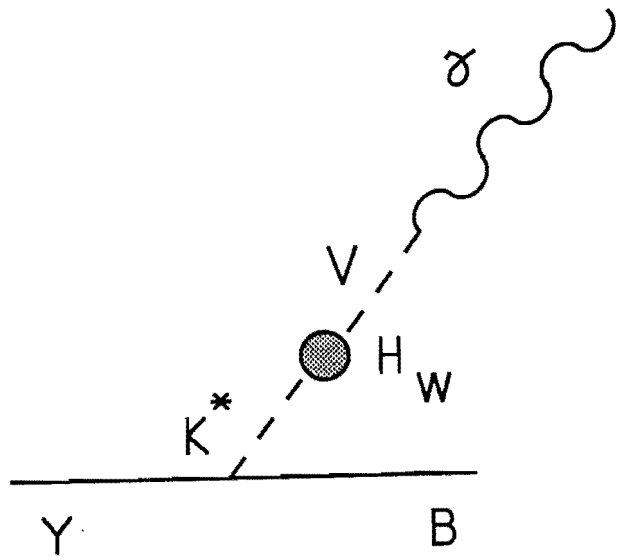

Figure 1.3: K^* pole diagram used by Nardulli [21]. V is a low mass vector meson such as ρ, ω, or ϕ.

hyperon radiative decays and Table 1.3 for a summary of the pole model predictions for the asymmetry parameters of hyperon radiative decays.

Graham and Pakvasa [14] use SU(3) symmetry to relate the hyperon radiative decays to the non-leptonic decays of the hyperons. They use the SU(3) predictions for the magnetic moments of the hyperons. Farrar [15] used only the lowest lying $\frac{1}{2}^+$ baryons as intermediate states. The large errors are due to the large errors (at the time) in the measured magnetic moments of the hyperons. Scadron and Thebaud [16] included the $\frac{3}{2}^+$ intermediate states in their pole model. Gavela *et al*, Close and Rubinstein [17] and Rauh [19] included the $\frac{1}{2}^+$ $(56,0^+)$ intermediate states for the parity-conserving amplitude and the $\frac{1}{2}^-$ $(70,1^-)$ intermediate states for the parity-violating amplitude. Scadron and Visinescu [20] included $\frac{3}{2}^+$ intermediate states and related the amplitudes for $\Sigma^+ \rightarrow p\gamma$ to Ω^- non-leptonic decays. Nardulli included meson pole diagrams such as the one shown in Fig. 1.3.

The constituent quark model works well ($\sim$ 20%) in predicting the baryon magnetic moments. One can look at hyperon radiative decays in this context. Hyperon radiative decays are then just the single quark transition $s \rightarrow d\gamma$ shown in Fig. 1.4. The other two quarks in the hyperon are considered spectators. Gilman and Wise [22]

Reference	year	$\Sigma^+ \to p\gamma$	$\Lambda \to n\gamma$	$\Xi^0 \to \Lambda\gamma$	$\Xi^0 \to \Sigma^0\gamma$	$\Xi^- \to \Sigma^-\gamma$
Graham [14]	1965	1.4	0.75	0.3	1.1	0.02
Farrar [15]	1971	0.34 ± 1.25	1.9 ± 0.8			
Scadron [16]	1973	0.78	1.5	15.	10.	0
Gavela [18]	1981	$0.92\ ^{+.26}_{-.14}$	0.62	3.	7.2	
Rauh [19]	1981	$0.82\ ^{+.41}_{-.31}$	1.02	2.29	5.87	
Scadron [20]	1983	0.66				
Nardulli [21]	1988	1.05	0.17	0.72	2.4	0.51
Measured [2]	1990	1.25 ± 0.07	1.02 ± 0.33	1.06 ± 0.16	3.56 ± 0.43	0.23 ± 0.10

Table 1.2: Theoretical predictions for the branching ratios of radiative decays of hyperons (units of 10^{-3}) in the pole model.

Reference	year	$\Sigma^+ \to p\gamma$	$\Lambda \to n\gamma$	$\Xi^0 \to \Lambda\gamma$	$\Xi^0 \to \Sigma^0\gamma$	$\Xi^- \to \Sigma^-\gamma$
Graham [14]	1965	+0.061	+0.25	-0.25	+0.031	-0.37
Farrar [15]	1971	$+0.8\ ^{+.2}_{-1.1}$	-0.5 ± 0.4			
Scadron [16]	1973	-0.2 → -0.5	-0.995	-0.95	-0.90	0
Close [17]	1980	-0.6 → -1.	small	small	-0.3	
Gavela [18]	1981	$-0.80\ ^{+.32}_{-.19}$	-0.49	-0.78	-0.96	
Rauh [19]	1981	$-0.86\ ^{+.11}_{-.13}$	-0.10	-0.41	-0.58	
Scadron [20]	1983	-0.38				
Nardulli [21]	1988	-1.	-0.72	+0.11	-0.54	0
Measured [2]	1990	-0.83 ± 0.12		+0.43 ± 0.44	+0.20 ± 0.32	

Table 1.3: Theoretical predictions for the asymmetry parameters of radiative decays of hyperons in the pole model.

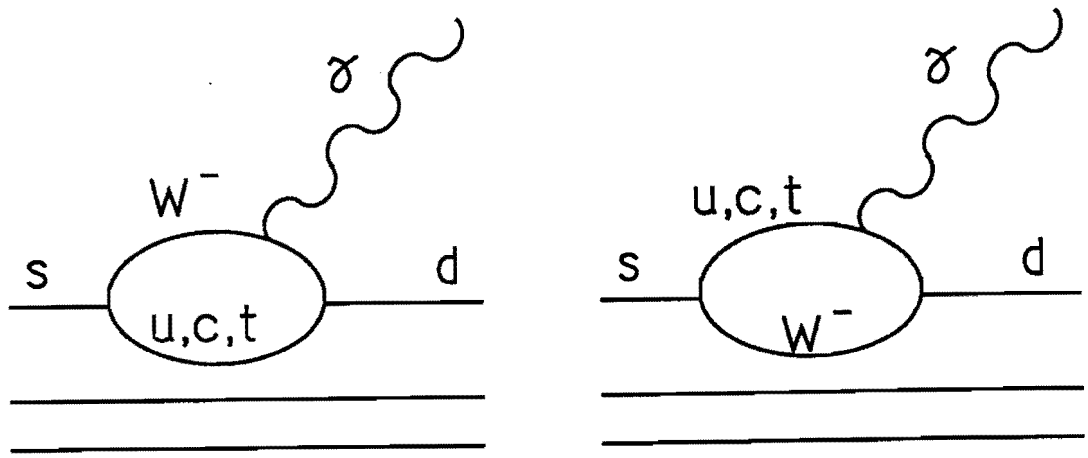

Figure 1.4: Hyperon radiative decay, single quark transition s $\rightarrow$ dγ.

considered the diagram in Fig. 1.5. They used the most general form for the amplitude and found a relationship among the radiative decays. They normalized all of their branching ratios to the measured branching ratio of $\Sigma^+ \rightarrow p\gamma$ (1.24×10^{-3}.) The results are shown in Table 1.4. It is clear that the measured rates are not consistent with the predictions in this picture. Kogan and Shifman [23] calculated a rate for $\Sigma^+ \rightarrow p\gamma$ assuming the single quark transition s $\rightarrow$ dγ. They found the branching ratio for $\Sigma^+ \rightarrow p\gamma$ is $\sim 2 \times 10^{-6}$. This is about 3 orders of magnitude below the experimentally measured value. They concluded that "the mechanism of Fig. 1.4 cannot play an important role in weak radiative decays" [23].

One can also look at the effects of the two-quark transition shown in Fig. 1.6. These diagrams can contribute to all hyperon radiative decays except $\Xi^- \rightarrow \Sigma^-\gamma$, $\Omega^- \rightarrow \Xi^-\gamma$ and $\Omega^- \rightarrow \Xi(1530)^-\gamma$ because the initial states contain no u quark. Lo Chong-Huah [24] studied at the amplitude of the diagram shown in Fig 1.5 and found it to be negligible compared to the two quark transition. Lo Chong-Huah also considered the three-quark transition of Fig. 1.7. This was also found to be negligible with respect to the two-quark transition. Lo Chong-Huah then used the second-quantized MIT bag model to calculate the two-quark transition amplitudes show in Fig 1.8. The prediction for the asymmetry parameter for $\Sigma^+ \rightarrow p\gamma$ is α_γ = -0.154.

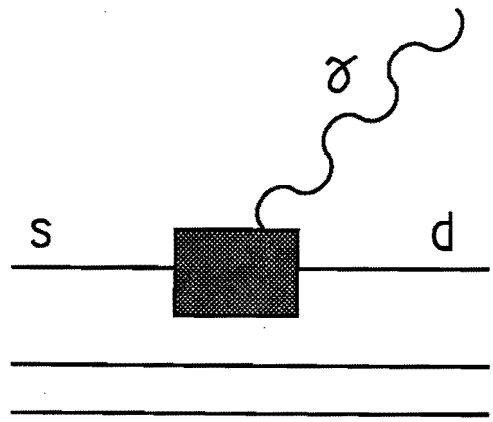

Figure 1.5: Single quark transition considered by Gilman and Wise [22].

Decay	Predicted branching ratio	Measured [2] branching ratio
$\Sigma^+ \to p\gamma$	1.24×10^{-3} (input)	$1.25 \pm 0.07 \times 10^{-3}$
$\Lambda \to n\gamma$	2.2×10^{-2}	$1.02 \pm 0.33 \times 10^{-3}$
$\Xi^0 \to \Sigma^0\gamma$	9.1×10^{-3}	$3.56 \pm 0.43 \times 10^{-3}$
$\Xi^0 \to \Lambda\gamma$	4.0×10^{-3}	$1.06 \pm 0.16 \times 10^{-3}$
$\Xi^- \to \Sigma^-\gamma$	1.1×10^{-2}	$2.3 \pm 1.0 \times 10^{-4}$
$\Omega^- \to \Xi^-\gamma$	4.1×10^{-2}	$<2.2 \times 10^{-3}$
$\Omega^- \to \Xi(1530)^-\gamma$	4.5×10^{-3}	

Table 1.4: Gilman and Wise [22] predictions for hyperon radiative decay branching ratios.

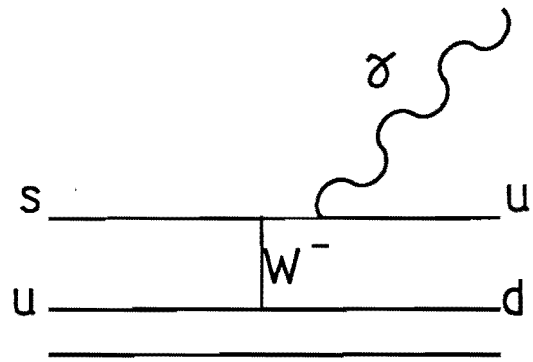

Figure 1.6: 2-quark transition where the photon can be radiated from any line.

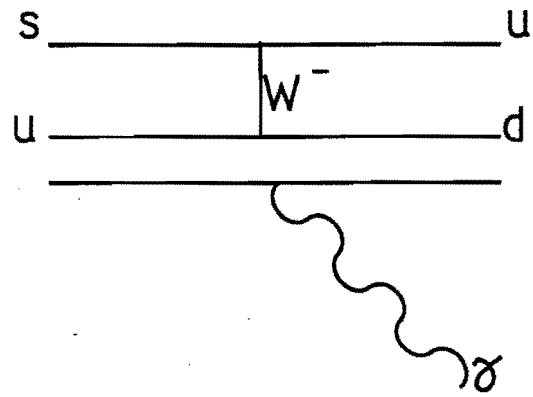

Figure 1.7: 3-quark transition.

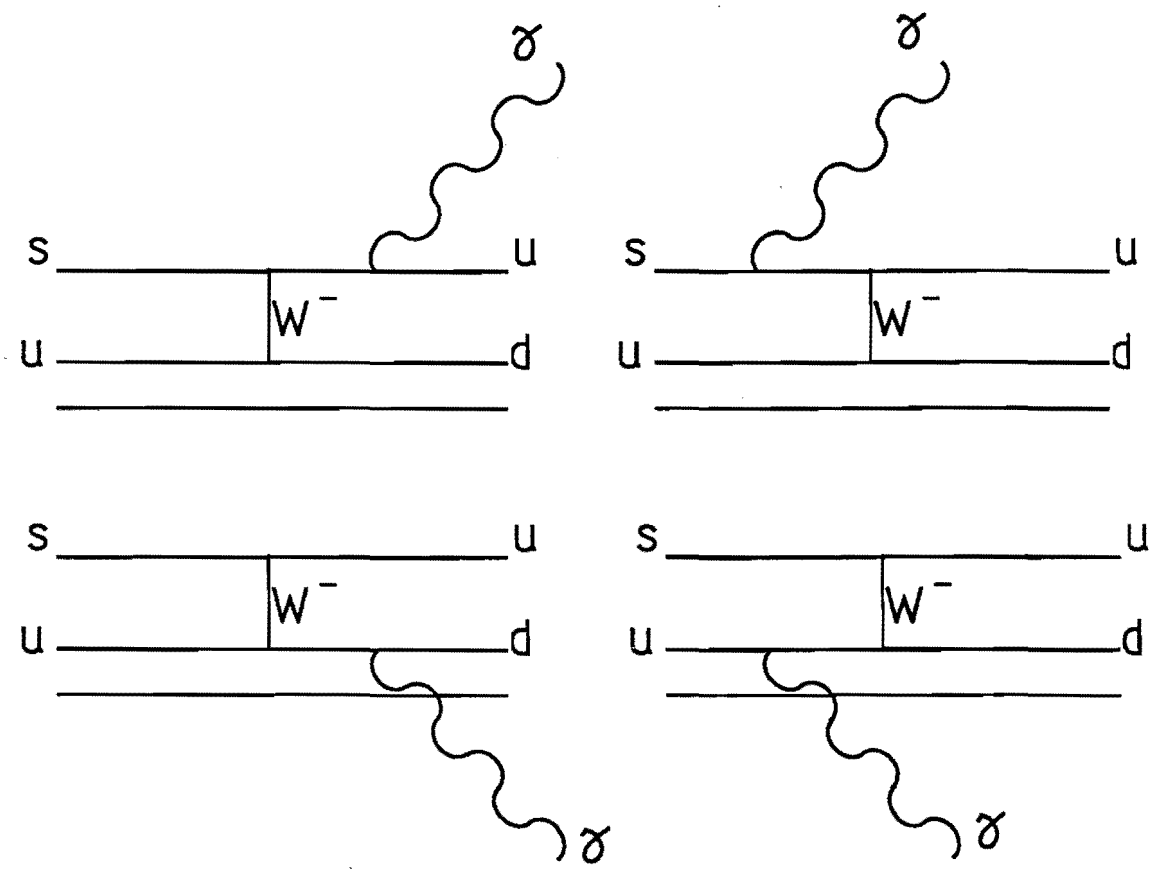

Figure 1.8: 2-quark transitions calculated by Lo Chong-Huah [24].

Decay	Calculated BR Sol'n. A	Calculated BR Sol'n. B	Calculated α Sol'n. A	Calculated α Sol'n. B	Measured [2] BR	Measured [2] α
$\Sigma^+ \to p\gamma$	1.24 *	1.24 *	-0.5 *	-0.5 *	1.25 ± 0.07	-0.83 ± 0.12
$\Xi^- \to \Sigma^-\gamma$	1.20 *	1.20	-0.87	+0.56	0.23 ± 0.10	
$\Lambda \to n\gamma$	5.97	1.70	-0.87	+0.25	1.02 ± 0.33	
$\Xi^0 \to \Sigma^0\gamma$	1.48	0.23	-0.3	-0.99	3.56 ± 0.43	$+0.20 \pm 0.32$
$\Xi^0 \to \Lambda\gamma$	1.80	1.36	-0.96	-0.45	1.06 ± 0.16	$+0.43 \pm 0.44$
$\Omega^- \to \Xi^-\gamma$	0.6	0.6	-0.87	+0.56	< 2.2	

Table 1.5: Kamal and Verma [25] predictions for hyperon radiative decay branching ratios (units of 10^{-3}) and asymmetries. The symbol * means the value was used as input.

This is in disagreement with experiment [2]($\alpha_\gamma = -0.83 \pm 0.12$).

Kamal and Verma [25] use a model involving the single quark transition, $s \to d\gamma$ (Fig. 1.5) and the two-quark transitions (Fig. 1.8.) They construct a three parameter model using the known branching ratio and asymmetry parameter of $\Sigma^+ \to p\gamma$ and the then upper limit on the branching ratio of $\Xi^- \to \Sigma^-\gamma$ (branching ratio $< 1.20 \times 10^{-3}$.) In their model, they *saturate* the rate $\Gamma(\Xi^- \to \Sigma^-\gamma$.) Due to a quadratic ambiguity in their model they get two sets of solutions. These are listed in Table 1.5. There is a discrepancy with the branching ratios and asymmetry parameters for both $\Xi^0 \to \Sigma^0\gamma$ and $\Xi^0 \to \Lambda\gamma$.

Verma and Sharma [26] reinvestigated the single- and two-quark transitions contributing to hyperon radiative decays. They calculated the combined effect of the diagrams in Fig 1.4 and Fig 1.6. The two parameters in the model are determined by three different approaches, electroweak gauge theory, QCD effects and long-distance effects. Each approach gives a different ratio of the two parameters. The branching ratio of $\Xi^- \to \Sigma^-\gamma$ is used to fix one of these parameters. Therefore for each of the approaches both parameters are determined. The results are given in Table 1.6 and Table 1.7.

Decay	pure two-quark transitions	electroweak gauge theory	QCD effects	long distance effects	Measured [2]
$\Sigma^+ \rightarrow p\gamma$	1.20	1.20	1.01	1.37	1.25 ± 0.07
$\Lambda \rightarrow n\gamma$	1.28	0.95	0.357	1.66	1.02 ± 0.33
$\Xi^0 \rightarrow \Lambda\gamma$	0.70	0.36	0.29	0.57	1.06 ± 0.16
$\Xi^0 \rightarrow \Sigma^0\gamma$	2.62	4.43	4.58	4.06	3.56 ± 0.43
$\Omega^- \rightarrow \Xi^-\gamma$	0	0.52	0.52	0.52	<2.2

Table 1.6: Predicted branching ratios (units of 10^{-3}) from Verma and Sharma [26]. These results included both single and two-quark transitions.

Decay	pure two-quark transitions	electroweak gauge theory	QCD effects	long distance effects	Measured [2]
$\Sigma^+ \rightarrow p\gamma$	-0.30	-0.59	-0.56	-0.55	-0.83 ± 0.12
$\Lambda \rightarrow n\gamma$	+0.58	-0.66	-0.51	-0.52	
$\Xi^0 \rightarrow \Lambda\gamma$	+1.00	+0.87	+1.00	+0.74	$+0.43 \pm 0.44$
$\Xi^0 \rightarrow \Sigma^0\gamma$	+0.96	+0.90	+0.97	+0.81	$+0.20 \pm 0.32$
$\Xi^- \rightarrow \Sigma^-\gamma$	0	+0.44	+1.00	-0.44	
$\Omega^- \rightarrow \Xi^-\gamma$	0	+0.44	+1.00	-.044	

Table 1.7: Predicted asymmetries from Verma and Sharma [26]. These results included both single and two-quark transitions.

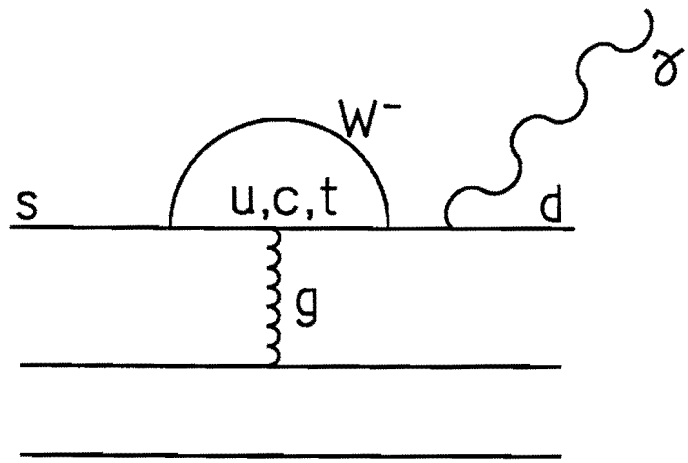

Figure 1.9: Photo-penguin diagram in hyperon radiative decays.

There is another class of diagrams that can contribute to hyperon radiative decays. These are the variants of the penguin diagrams called photo-penguins, shown in Fig. 1.9. It has been suggested [27, 28, 29, 30, 31] that penguin diagrams are believed to play a role in the $\Delta I = \frac{1}{2}$ rule and ϵ'/ϵ ratio in neutral kaon decays. Kamath [32] calculates the contribution of the penguin diagram of Fig. 1.9 to the decays $\Xi^- \rightarrow \Sigma^-\gamma$ and $\Omega^- \rightarrow \Xi^-\gamma$. Kamath uses a non-relativistic quark model with negative parity baryons. The results are that the branching ratio of $\Xi^- \rightarrow \Sigma^-\gamma$ is $1.257\alpha^2(\mu) \times 10^{-5}$ and the branching ratio of $\Omega^- \rightarrow \Xi^-\gamma$ is $0.53\ \alpha^2(\mu) \times 10^{-3}$, where $\alpha(\mu)$ is an enhancement coefficient which depends on the renormalization mass. The value of $\alpha(\mu)$ can not be calculated with great accuracy but is estimated to be about -0.08. This gives for a branching ratio for $\Xi^- \rightarrow \Sigma^-\gamma$ of $\sim 10^{-7}$ and for $\Omega^- \rightarrow \Xi^-\gamma \sim 10^{-5}$. The measured [2] branching ratio of $\Xi^- \rightarrow \Sigma^-\gamma$, $(2.3\pm1.0) \times 10^{-4}$, is in disagreement with these calculations. Eeg [33] also calculates the contribution of the penguin diagrams in Fig. 1.9 to the branching ratio of $\Xi^- \rightarrow \Sigma^-\gamma$ and $\Omega^- \rightarrow \Xi^-\gamma$. Eeg uses a pole model calculation with negative parity resonances and bag model matrix elements. The results are similar to Kamath, the branching ratio of $\Xi^- \rightarrow \Sigma^-\gamma$ is $\sim 10^{-8}$ - 10^{-7} and the branching ratio of $\Omega^- \rightarrow \Xi^-\gamma$ is $\sim 10^{-5}$ - 10^{-4}.

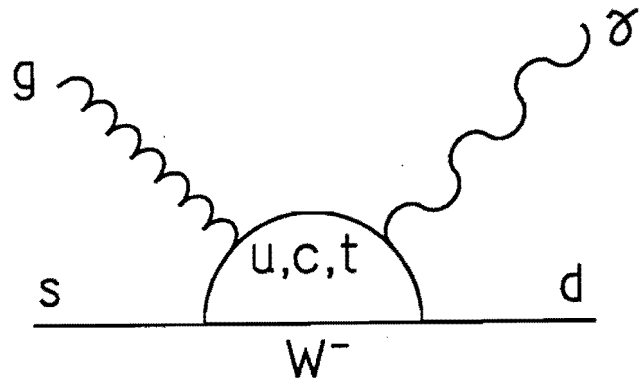

Figure 1.10: Penguin diagram analyzed by Gaillard, Li and Rudaz.

	$BR(\Sigma^+ \to p\gamma)$	$\alpha_{\Sigma^+\to p\gamma}$	$\frac{BR(\Sigma^+\to p\gamma)}{BR(\Xi^-\to\Sigma^-\gamma)}$	$\alpha_{\Xi^-\to\Sigma^-\gamma}$
case 1	2×10^{-9} - 10^{-6}	-0.6 - -0.3	0.4 - 0.2	-0.7
case 2	2×10^{-9} - 10^{-6}	-0.84	0.7	+0.47
Measured [2]	$1.25 \pm 0.07 \times 10^{-3}$	-0.83 ± 0.12	3.6 - 10.2	

Table 1.8: Predictions of Gaillard, Li and Rudaz [34].

Gaillard, Li and Rudaz [34] studied the contribution from the diagram in Fig. 1.10. They used the MIT bag model with a range of values of the strong coupling constant, $\alpha_s = 0.5$ - 10 (case 1.) They also used a more complicated model taking into account the static color field (case 2.) For case 2, the results are evaluated at $\alpha_s = 3$. The results are given in Table 1.8

Hyperon radiative decays can also be analyzed in terms of QCD sum rules. Goldman and Escobar [35] look at the short distance contribution $s \to d\gamma$ in the decays $\Sigma^+ \to p\gamma$ and $\Xi^- \to \Sigma^-\gamma$. Khatsymovsky [36, 37] and Balitsky, Braun and Kolesnichenko [38] also use QCD sum rules to calculate branching ratios and asymmetries of hyperon radiative decays. The results are given in Table 1.9 and Table 1.10. Balitsky's *et al* [38] predictions agree well with the current experimental values.

Żenczykowski [39] used a combined symmetry/vector dominance model to predict branching ratios and asymmetry parameters for hyperon radiative decays. He relates

Reference	$\Sigma^+ \to p\gamma$	$\Xi^- \to \Sigma^-\gamma$	$\Xi^0 \to \Lambda\gamma$	$\Lambda \to n\gamma$	$\Omega^- \to \Xi^-\gamma$
Goldman [35]	0.047	0.002			
Khats. [36]	0.08	0.20			0.23
Khats. [37]			1.1	2 - 3	
Balitsky [38]	0.5 - 1.5				
Measured [2]	1.25 ± 0.07	0.23 ± 0.10	1.06 ± 0.16	1.02 ± 0.33	< 2.2

Table 1.9: QCD sum rule predictions for branching ratios of hyperon radiative decays in units of 10^{-3}.

Reference	$\Sigma^+ \to p\gamma$	$\Xi^- \to \Sigma^-\gamma$	$\Xi^0 \to \Lambda\gamma$	$\Lambda \to n\gamma$
Goldman [35]	-1.0	+0.9		
Khatsymovsky [36]	+1.0	+0.4		
Khatsymovsky [37]			+0.9	+0.10 - +0.15
Balitsky [38]	-0.85 ± 0.15			
Measured [2]	-0.83 ± 0.12		+0.43 ± 0.44	

Table 1.10: QCD sum rule predictions for asymmetry parameters of hyperon radiative decays.

Decay	Predicted		Measured [2]	
	branching ratio	α	branching ratio	α
$\Sigma^+ \rightarrow p\gamma$	1.33	-0.96	1.25 ± 0.07	-0.83 ± 0.12
$\Lambda \rightarrow n\gamma$	0.86	+0.83	1.02 ± 0.33	
$\Xi^0 \rightarrow \Lambda\gamma$	0.86	+0.71	1.06 ± 0.16	+0.43 ± 0.44
$\Xi^0 \rightarrow \Sigma^0\gamma$	3.17	-0.41	3.56 ± 0.43	+0.20 ± 0.32
$\Xi^- \rightarrow \Sigma^-\gamma$	0.27	+0.59	0.23 ± 0.10	

Table 1.11: Best results of fit to hyperon radiative decay data from the combined symmetry/vector dominance model of Żenczykowski [39]. The branching ratios are in units of 10^{-3}.

hyperon radiative decays $Y \rightarrow B + \gamma$ to hyperon non-leptonic decays $Y \rightarrow B + \pi$. See Fig. 1.11 which shows the quark diagrams relating these two processes. Non-leptonic decays of the hyperons determine two of the three parameters in the parity-violating amplitudes. The third parameter is determined by a fit to the data of the eight measurements of hyperon radiative decays. The results of the best fit are given in Table 1.11. The value of χ^2 for the fit is 7.9 for 7 degrees-of-freedom. The model does quite well in describing the data. The largest deviation is a 2 standard deviation effect in α for $\Xi^0 \rightarrow \Sigma^0\gamma$.

It has been suggested by Ahmed and Ross [40] and Vasanti [13] that hyperon radiative decays might be a likely place to search for right-handed currents. Shifman, Vainshtein and Zakharov [41] found that the coefficients occurring in the operator product expansion for right-handed currents are small. They concluded that right-handed currents are unimportant in hyperon radiative decays.

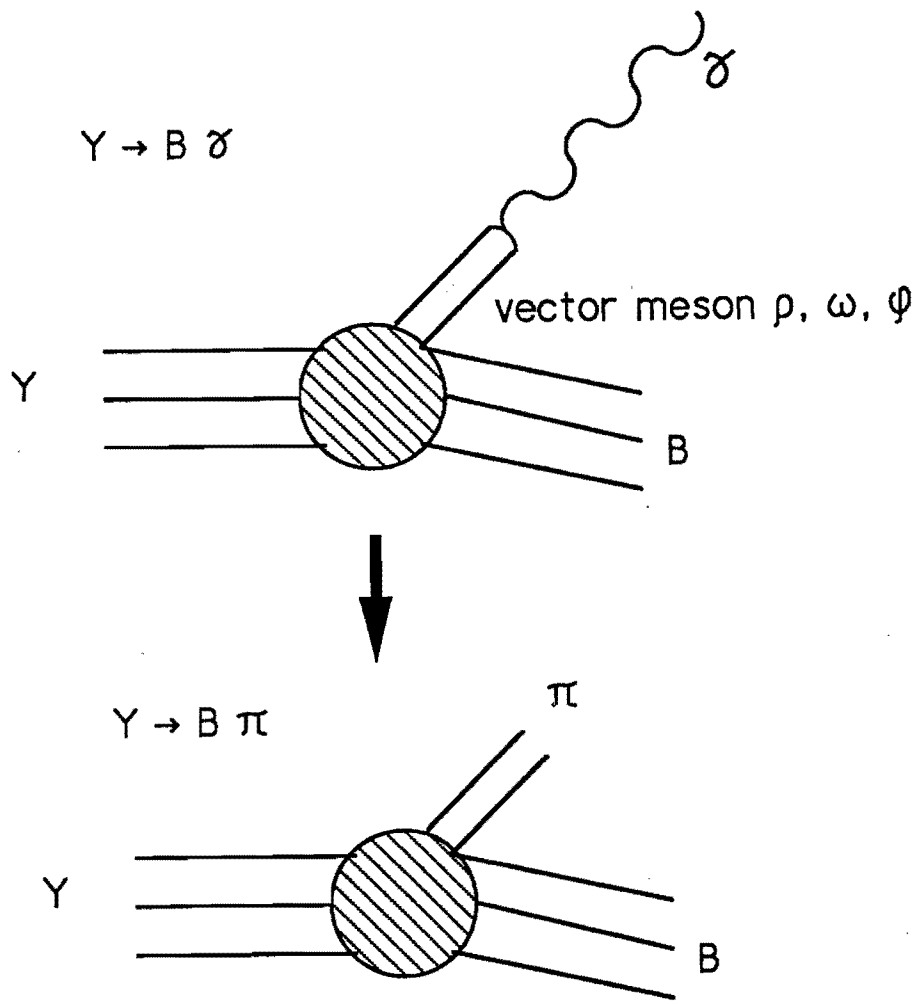

Figure 1.11: Żenczykowski's combined symmetry/vector dominance model approach of relating $Y \to B + \gamma$ to $Y \to B + \pi$. For hyperon radiative decays the photon couples to the vector mesons, ρ, ω, or ϕ.

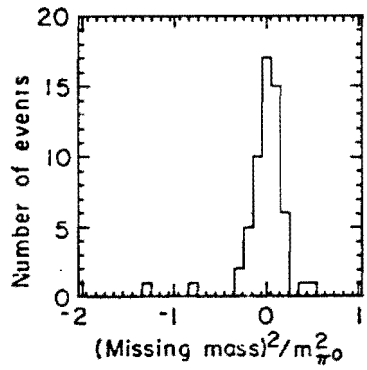

$(MM)^2$ distribution for 59 of the 61 $\Sigma^+ \rightarrow p\gamma$ events used in determining α.

Figure 1.12: Missing-mass-squared distribution, m_x^2 assuming $\Sigma^+ \rightarrow p + x$. from Gershwin *et al* [5].

1.2 Previous Experiments

1.2.1 Asymmetry Parameter $\Sigma^+ \rightarrow p\gamma$

The first experiment to report on the asymmetry parameter for $\Sigma^+ \rightarrow p\gamma$ was Gershwin *et al* [5] in 1969. This experiment was performed in the Berkeley 25-inch hydrogen bubble chamber. The Σ^+ were produced by stopping K^- in the hydrogen bubble chamber target via the reaction

$$K^- p \rightarrow \Lambda(1520) \rightarrow \Sigma^+ \pi^-$$

The momentum range of the K^- was 290 - 470 MeV/c but most of the events were around 390 MeV/c. The Σ^+ were produced polarized by the interference of the resonant D-wave amplitude and S-wave background. The polarization was ~40%. They took 1.3×10^6 pictures of which 57,000 were of the form $\Sigma^+ \rightarrow p + neutral$. They had a final sample of 61 $\Sigma^+ \rightarrow p\gamma$ events. The missing-mass-squared distribution (m_x^2 assuming $\Sigma^+ \rightarrow p + x$.) is shown in Fig. 1.12. The resolution in missing-mass-squared was 0.0018 - 0.0036 GeV^2/c^4 depending on whether the decay proton was stopped in the bubble chamber. They found $\alpha_\gamma = -1.03^{+0.52}_{-0.42}$.

Manz *et al* [4] in 1980 reported a second measurement of α_γ. This experiment was performed at the CERN PS using the HYperon BUbble Chamber(HYBUC.) The bubble chamber was 11 cm in diameter and 32 cm long and filled with hydrogen. The

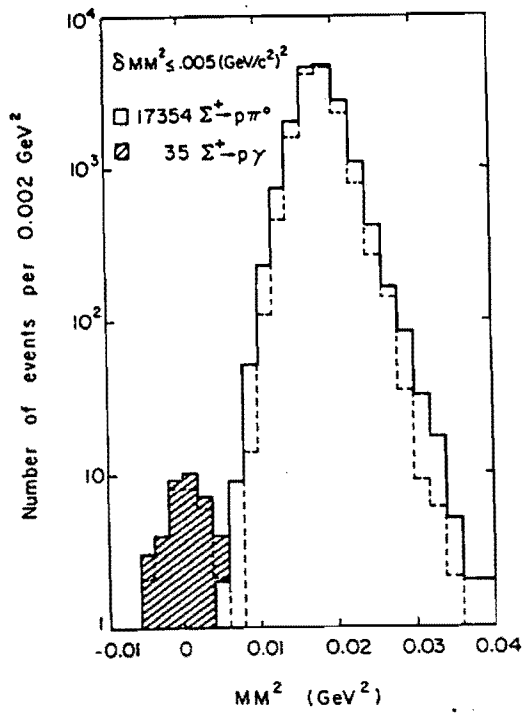

The decay missing mass squared distribution for the $\Sigma^+ \to p\pi^0$ (open) and $\Sigma^+ \to p\gamma$ (shaded) samples, for events with $\delta MM^2 < 0.005$ GeV^2. The dashed line shows the events having $\delta MM^2 < 0.004$ GeV^2.

Figure 1.13: Missing-mass-squared distribution, m_x^2 assuming $\Sigma^+ \to p + x$. from Manz *et al* [4].

Σ^+ were produced in the reaction

$$K^- p \to \Sigma^+ \pi^-$$

with a K^- momentum of 420 - 500 MeV/c. They took 2×10^6 pictures of which 35,832 fitted the hypothesis $\Sigma^+ \to p + neutral$. Their missing-mass-squared distribution is shown in Fig. 1.13. They had a missing-mass-squared resolution of 0.005 GeV$^2/c^4$. They collected a total of 46 $\Sigma^+ \to p\gamma$ events and found $\alpha_\gamma = -0.53^{+0.38}_{-0.36}$.

The latest experiment to report a value of α_γ is Kobayashi *et al* [3] in 1987. This was the first experiment to use counter techniques to measure the asymmetry parameter. They produced polarized Σ^+ in the reaction

$$\pi^+ p \to \Sigma^+ K^+$$

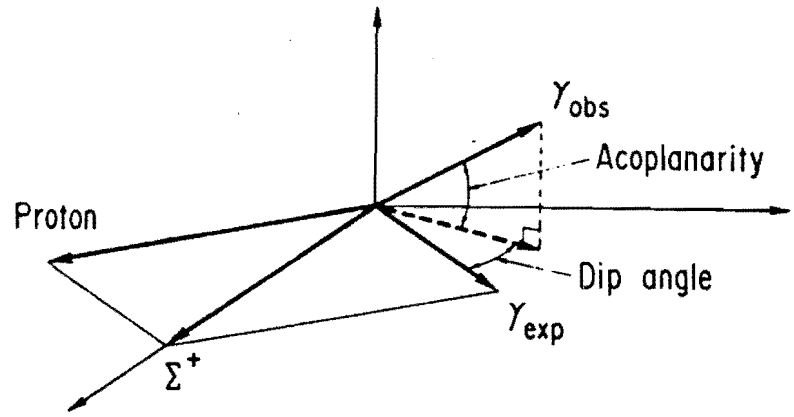

Definition of acoplanarity and dip angle. γ_{obs}: direction of the observed γ ray; γ_{exp}: direction of the γ ray kinematically expected from the observed proton and Σ^+ momenta. The decay plane is defined by the directions of proton and Σ^+.

Figure 1.14: Acoplanarity and dip angle used to isolate $\Sigma^+ \rightarrow p\gamma$ from Kobayashi *et al* [3].

inside a liquid hydrogen target. The momentum of the π^+ was 1.7 GeV/c. The polarization was ~87%. They isolated a signal using the mass of the missing neutral and the direction of photon as measured in the apparatus. See Fig. 1.14. The direction of the photon as measured, γ_{obs}, defines two quantities, the acoplanarity and dip angle. The acoplanarity measures the angle between the observed photon direction and the plane defined by the Σ^+ and proton tracks. The dip angle measures the angle in the plane of the Σ^+ and proton between the observed photon direction and the expected direction of the photon assuming the decay $\Sigma^+ \rightarrow p\gamma$. One expects to find $\Sigma^+ \rightarrow p\gamma$ events to be concentrated at the origin of the dip angle - acoplanarity plane. Shown in Fig. 1.15 is the dip angle distributions of $\Sigma^+ \rightarrow p\gamma$. As can be seen, there are peaks at a value of zero corresponding to the decay $\Sigma^+ \rightarrow p\gamma$. The upper distribution is for positive $\cos\theta_p$ and the lower for negative $\cos\theta_p$. The angle θ_p is the angle between the momentum of the proton and the Σ^+ polarization in the center of mass. They obtained a total sample of 190 events and found $\alpha_\gamma = -0.86 \pm 0.13$(statistical) $\pm$ 0.04 (systematic).

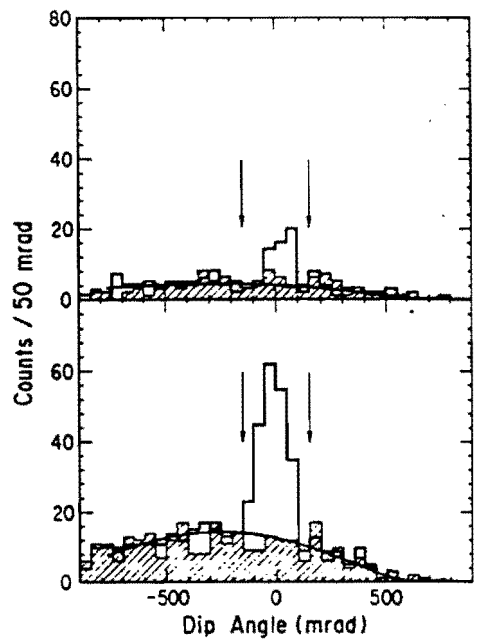

Dip-angle distributions of the γ rays after the acoplanarity cut selecting the events with |acoplanarity| < 120 mrad. Two subsets of the data with positive $\cos\vartheta_p$ (above) and with negative $\cos\vartheta_p$ (below) are shown together with the estimated background shapes (solid lines) and the distributions of events after the "off-centered" acoplanarity cut (hatched distributions). See text for details.

Figure 1.15: Dip angle distributions for two sets of data with positive $\cos\theta_p$ and negative $\cos\theta_p$. (θ_p is the center of mass angle between the Σ^+ polarization direction and the proton momentum. From Kobayashi *et al* [3].

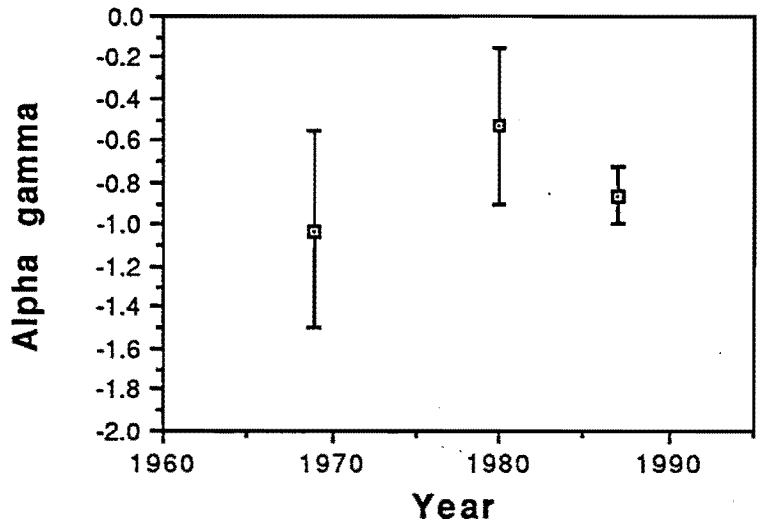

Figure 1.16: α_γ for $\Sigma^+ \rightarrow p\gamma$ from previous experiments.

These three experiments are summarized in Fig. 1.16. Kobayashi *et al* performed quite a good experiment considering they had a total of 190 events. The large polarization of the Σ^+ is the reason for such a small error in α_γ.

1.2.2 Branching Ratio $\Sigma^+ \rightarrow p\gamma$

The first experiment to report a value for the branching ratio of $\Sigma^+ \rightarrow p\gamma$ was that of Bazin *et al* [9] in 1965. They produced Σ^+ using stopped K^- via the reaction

$$K^- p \rightarrow \Sigma^+ \pi^-$$

The experiment was performed in the 30-inch Columbia-Brookhaven bubble chamber. They found a total of 24 events and a branching ratio of $(1.91 \pm 0.41) \times 10^{-3}$. All of these experiments (except Kobayashi *et al* [3]) actually measure the ratio of branching ratios $Br(\Sigma^+ \rightarrow p\gamma)/Br(\Sigma^+ \rightarrow p\pi^0)$. These have been converted to $Br(\Sigma^+ \rightarrow p\gamma)$ for clarity.

Gershwin *et al* [5] (described in section 1.2.1) also reported a value for the branching ratio. They found $Br(\Sigma^+ \rightarrow p\gamma) = (1.42 \pm 0.26) \times 10^{-3}$ from a sample of 31 $\Sigma^+ \rightarrow p\gamma$ events.

Ang *et al* [8] in 1969 measured Br($\Sigma^+ \rightarrow p\gamma$) and obtained a value of (1.08 $\pm$ 0.15) $\times$ 10^{-3}. They also produced Σ^+ using a stopped K^- beam in the reaction

$$K^- p \rightarrow \Sigma^+ \pi^-$$

Their experiment was performed in the 81-cm CERN-Saclay bubble chamber. They observed a total of 45 $\Sigma^+ \rightarrow p\gamma$ events

Manz *et al* [4], described before in section 1.2.1, found Br($\Sigma^+ \rightarrow p\gamma$) = (1.09 $\pm$ 0.20) $\times$ 10^{-3} using 46 events.

The first counter experiment, Biagi *et al* [7], to measure the branching ratio of $\Sigma^+ \rightarrow p\gamma$ reported a result in 1985. This experiment was performed in the CERN SPS charged hyperon beam. They measured a total of 155 events which yields Br($\Sigma^+ \rightarrow p\gamma$) = (1.27 $\pm$ 0.17) $\times$ 10^{-3}.

Kobayashi *et al* [3], described before in section 1.2.1, found Br($\Sigma^+ \rightarrow p\gamma$) = (1.30 $\pm$ 0.15) $\times$ 10^{-3} from 190 events.

Hessey *et al* [6] collected a sample of 408 $\Sigma^+ \rightarrow p\gamma$ events in 1989. They produced Σ^+ by stopping K^- in a liquid hydrogen target via the reaction

$$K^- p \rightarrow \Sigma^+ \pi^-$$

They found a value of the Br($\Sigma^+ \rightarrow p\gamma$)= (1.45 $\pm$ 0.26) $\times$ 10^{-3}.

The results of these seven experiments are summarized in Fig. 1.17.

1.3 Summary

Current theoretical models are not sufficiently well-rounded to describe, quantitatively, the decay $\Sigma^+ \rightarrow p\gamma$, and other hyperon radiative decays. Many theories of other forms of radiative decays require accurate values of the branching ratio and asymmetry parameter for the decay $\Sigma^+ \rightarrow p\gamma$ as parameters. It is important that greatly improved values of the branching ratio and the asymmetry parameter for the decay $\Sigma^+ \rightarrow p\gamma$ be obtained by carrying out a new experiment with high statistical accuracy and low systematic errors.

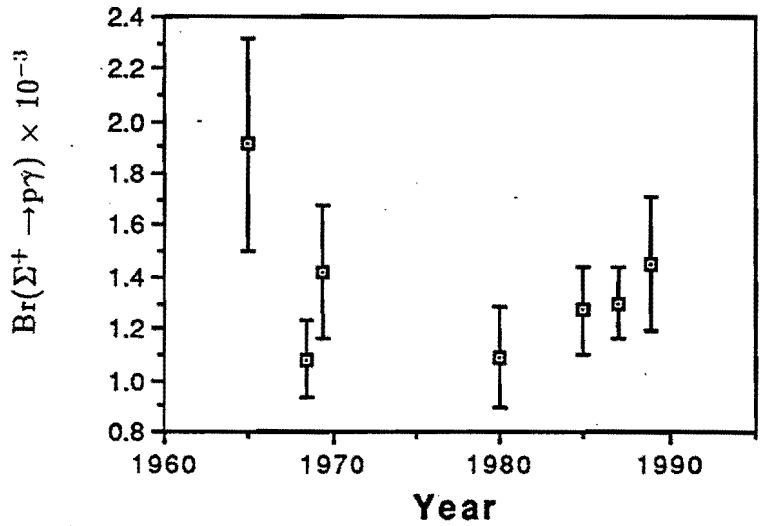

Figure 1.17: $Br(\Sigma^+ \rightarrow p\gamma)$ from previous experiments, in units of 10^{-3}.

Chapter 2

Experimental Apparatus

2.1 Introduction

The goal of the experiment was a high-precision measurement of the asymmetry parameter and branching ratio for the decay $\Sigma^+ \rightarrow p\gamma$. Before the experiment was performed we knew that the primary background would be from the decay $\Sigma^+ \rightarrow p\pi^0$ followed by $\pi^0 \rightarrow \gamma\gamma$. This background occurs at a rate about four hundred times the rate for $\Sigma^+ \rightarrow p\gamma$. The decay modes have similar kinematics and differ only by the additional photon. This experiment was specifically designed to overcome these difficulties. We produced polarized Σ^+ in the high rate ($\sim$ 2 KHz Σ^+) Fermilab proton center charged hyperon beam. The polarization could be reversed thus allowing biases in the apparatus to be cancelled. The mean Σ^+ momentum was 375 GeV/c. This corresponds to a mean decay length of 7.6 meters. This allowed us to measure the Σ^+ track with precision. We constructed high resolution spectrometers for both the Σ^+- and p-tracks from $\Sigma^+ \rightarrow p\gamma$. This gave us excellent missing-mass-resolution. A separate photon spectrometer was used to separate single photon events from two-photon events.

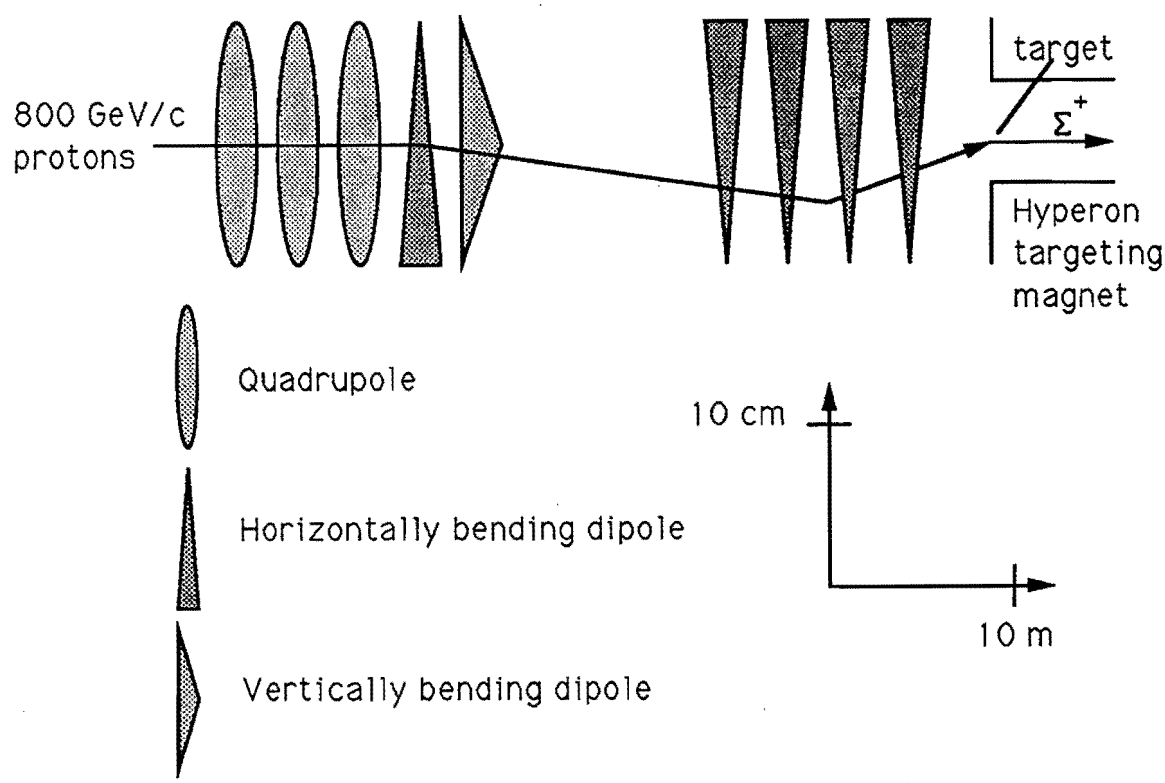

Figure 2.1: Schematic diagram (plan view) of PC3 enclosure. Positive targeting angle is shown.

2.2 Proton Center Beamline

The experiment was set up in the Proton Center beamline at Fermilab. A schematic diagram of the pre-target (PC3) area is given in Fig. 2.1. A series of quadrupole magnets focused the 800 GeV/c proton beam onto our target (described later.) The beam spot size of 0.5 mm horizontally and 1 mm vertically matched well the size of our target. Experiment 761 ran with $\sim 8 \times 10^{11}$ protons/spill on target. Each beam pulse was 23 sec long and occurred every 57 sec (40% duty factor).

To measure the asymmetry we needed a polarized beam of Σ^+ particles. We produced polarized Σ^+ in the inclusive reaction

$$p + Cu \rightarrow \Sigma^+ + anything$$

by steering the incoming proton beam onto the production target at a finite production angle (which we called the targeting angle.) Hyperon polarization in inclusive reactions was first observed [42] in Λ production. Many experiments have been performed since then that have studied hyperon polarization [43, 44, 45, 46]. It is observed that the production polarization is consistent with parity conservation of the strong interaction. That is, the polarization direction, $\vec{P}$, is along the direction given by the cross product

$$\vec{P} \propto \vec{p_p} \times \vec{p_Y} \tag{2.1}$$

where $\vec{p_p}$ is the incoming proton momentum direction and $\vec{p_Y}$ is the outgoing hyperon momentum direction. The Basel convention [47] defines that positive polarization is along the direction given in equation 2.1.

We obtained a finite targeting angle by bending the proton beam with the first dipole magnet. Then, with the four dipoles near the target,the beam was bent in the opposite direction back onto the target. Positive targeting angle by our convention is shown in Fig. 2.1. In our experiment data were taken with complimentary horizontal targeting angles near 4 mrad. This provided two sets of data with the Σ^+ polarization up and down. We could then cancel instrumental false asymmetries (biases) by averaging over the two data sets.

2.3 Hyperon Magnet and Channel

An overview of the full experimental setup is shown in Fig 2.2. Also shown in Fig 2.2 is the coordinate system used in E761. The z-axis pointed along the Σ^+ beam direction. The y-axis pointed up (opposite to the local direction of gravity.) The x-axis pointed in a direction to form a right-handed coordinate system ($\hat{x} \times \hat{y} = \hat{z}$.) That is the x-axis pointed left (west) while looking downstream. The z-origin was at the location of SD3.

The 800 GeV/c proton beam struck the one-interaction length Cu target at a finite targeting angle. The target is shown in Fig 2.3. The target was 2 mm high vertically and 0.6 mm wide horizontally. The width of the target was made narrow horizontally (bend plane) to achieve good momentum resolution. Requiring that the

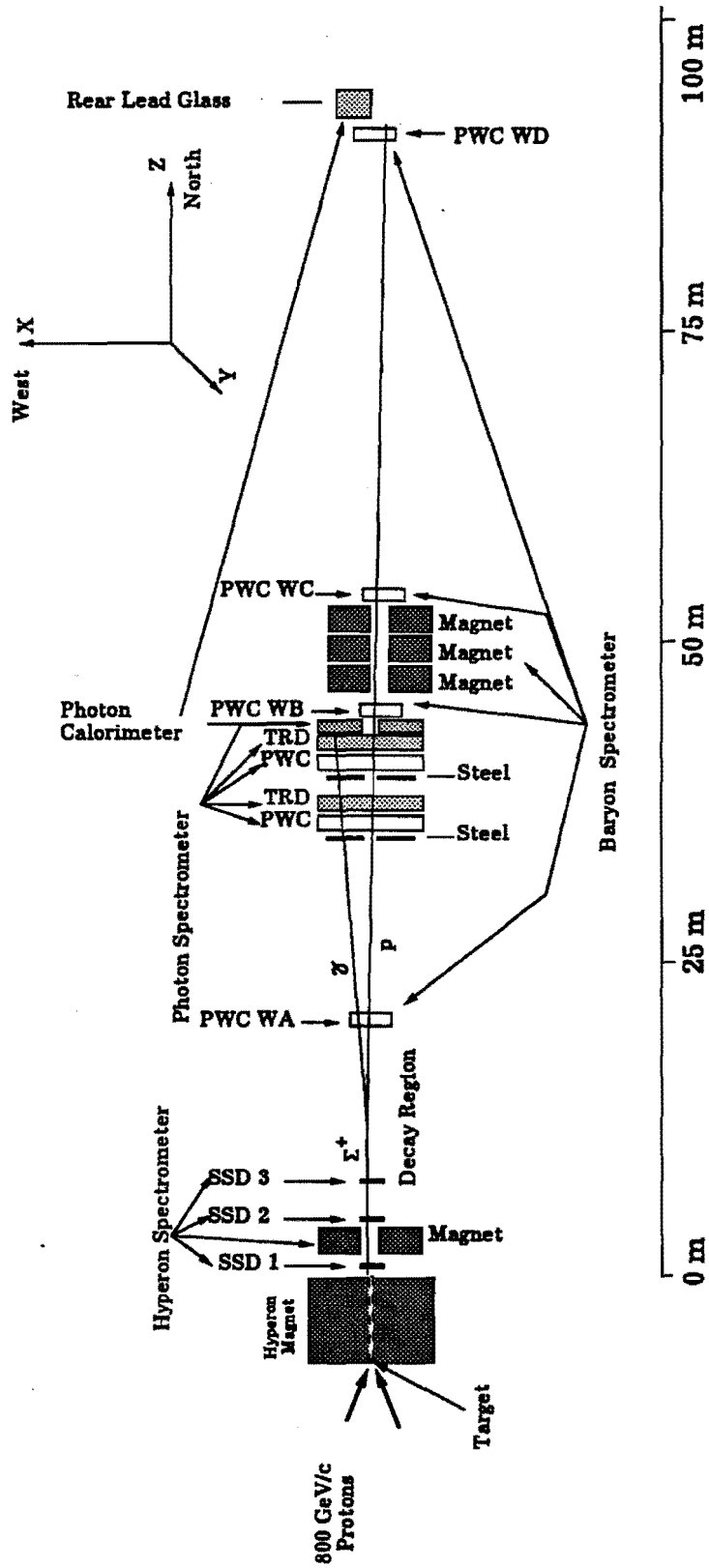

Figure 2.2: E761 experiment (plan view) in Proton Center enclosure 4 (PC4).

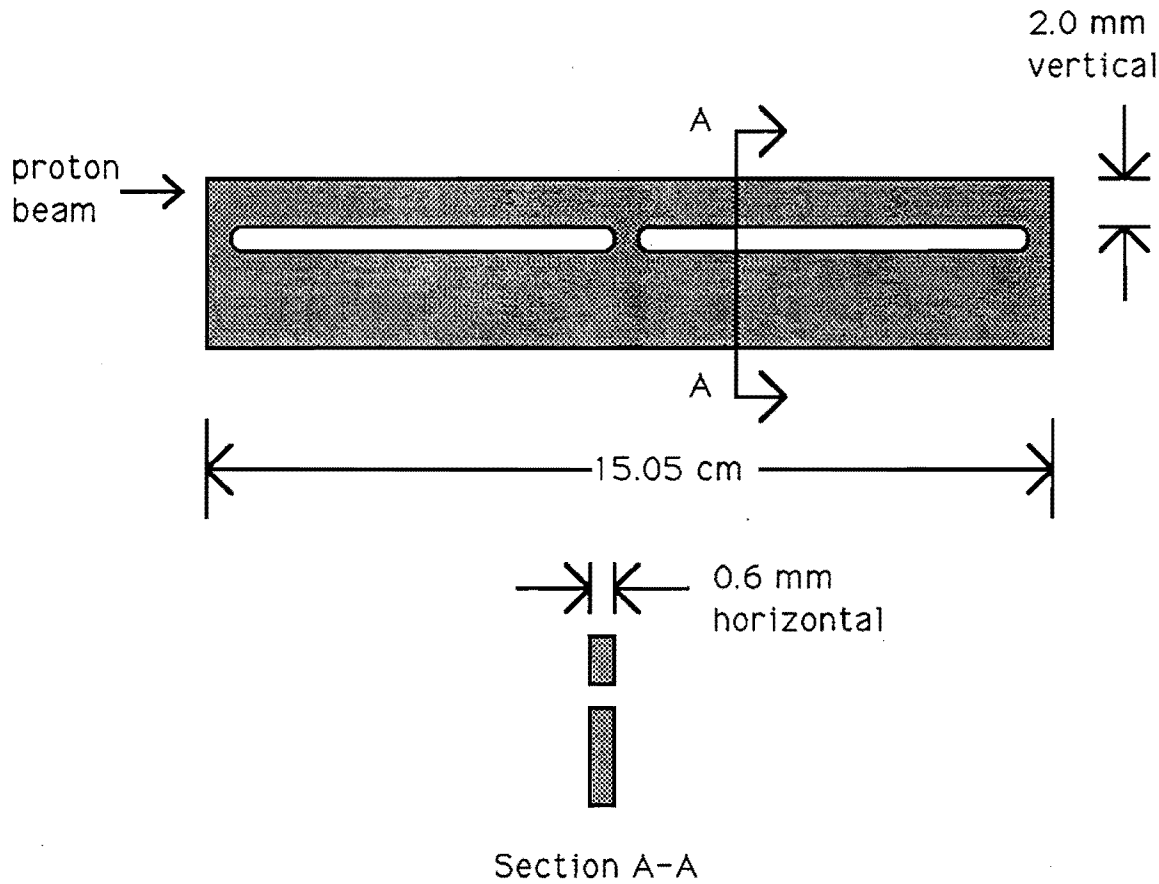

Figure 2.3: The one interaction length Cu target.

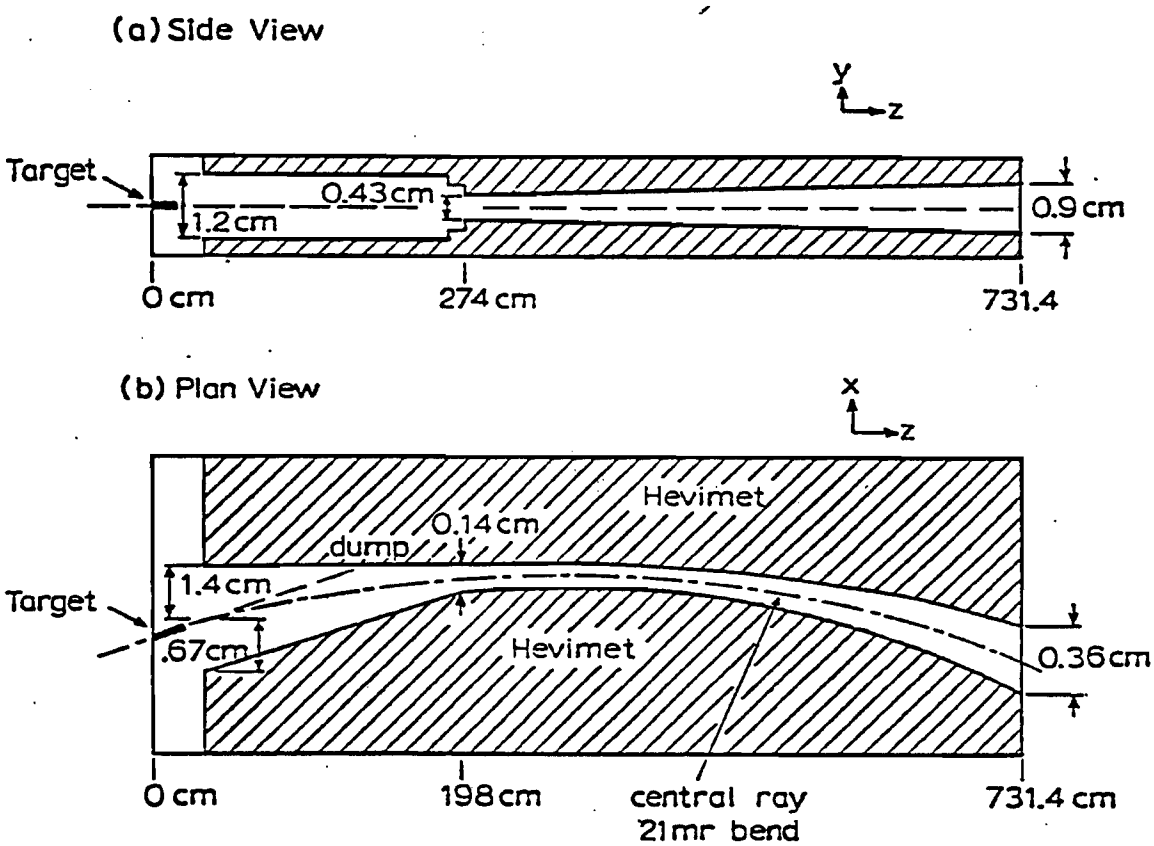

Figure 2.4: The hyperon magnet channel [48] used to define the hyperon beam. The channel was embedded inside the hyperon magnet. Figure taken from reference [48].

particles be produced in the target improved the momentum resolution by about a factor of two.

The hyperon beam was collimated by the hyperon magnet channel [48]. A diagram of the channel is given in Fig 2.4. The channel was embedded within the hyperon magnet. The hyperon magnet is a 7.3 m long dipole magnet which we ran at a field of ~35 kG (p_t kick ~-7.5 GeV/c.) At that field, the secondary hyperon momentum had a central momentum ~375 GeV/c. At the channel exit the beam momentum spread was $\Delta p/p = 14\%$ (full width at the base.) The size of the beam at the exit was 0.9 cm (y) × 0.36 cm (x.) The beam subtended a solid angle of 0.64 μsr. There were 2% Σ^+ in the beam at the exit of the channel with the rest of the beam mostly being made up of long-lived particles such as protons and pions.

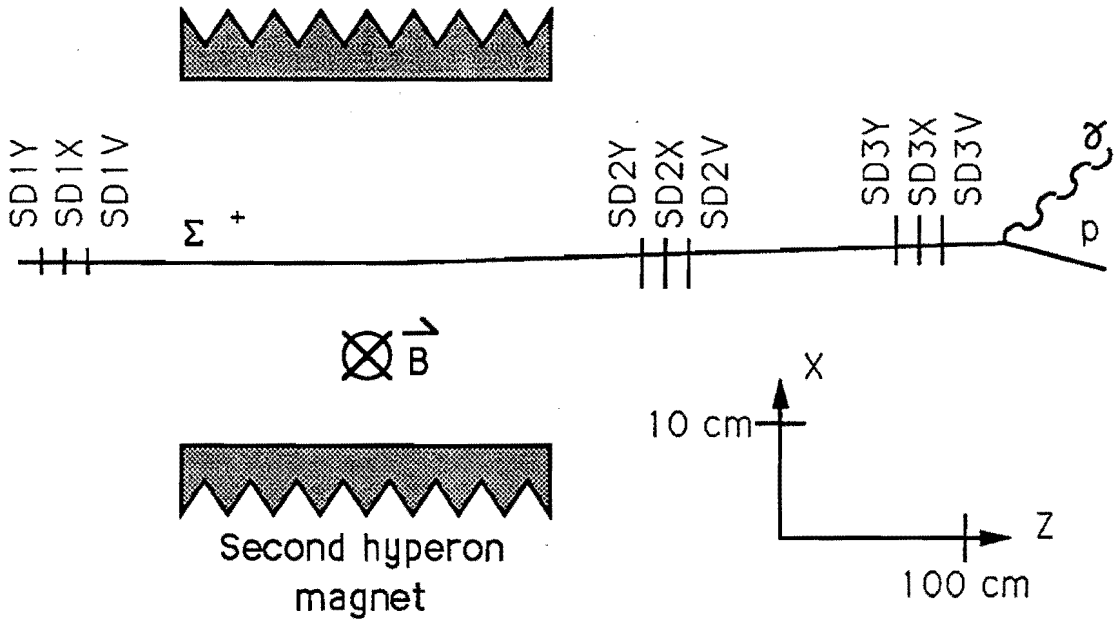

Figure 2.5: The hyperon spectrometer (plan view) used to measure the Σ^+ track.

2.4 Hyperon Spectrometer

The hyperon spectrometer was used to measure the Σ^+ track and momentum. A schematic diagram of the hyperon spectrometer is given in Fig 2.5. It is made up of three stations of silicon strip detector (SD1, SD2 and SD3) and 1 BM109 magnet (second hyperon magnet.) A BM109 magnet is a 2 m Fermilab magnet with a horizontal aperture of 61 cm and a vertical aperture of 20 cm. Each SD station was made up of 3 planes of detector, X, Y and V, where the V plane is rotated $\pm 45°$ with respect to X and Y. The silicon planes were 300μm thick with 50μm pitch. The p_t kick of the second hyperon magnet was 1.43 GeV/c. The momentum resolution (σ_p/p) of the hyperon spectrometer was 0.7%. The angular resolution (σ) was 12 μrad in horizontal (x) angle and 5 μrad in vertical (y) angle. These resolutions are the errors determined from the error matrix of the fit tracks appropriately increased by the square root of reduced χ^2. The resolution of each plane used in the fit is the strip spacing divided by $\sqrt{12}$.

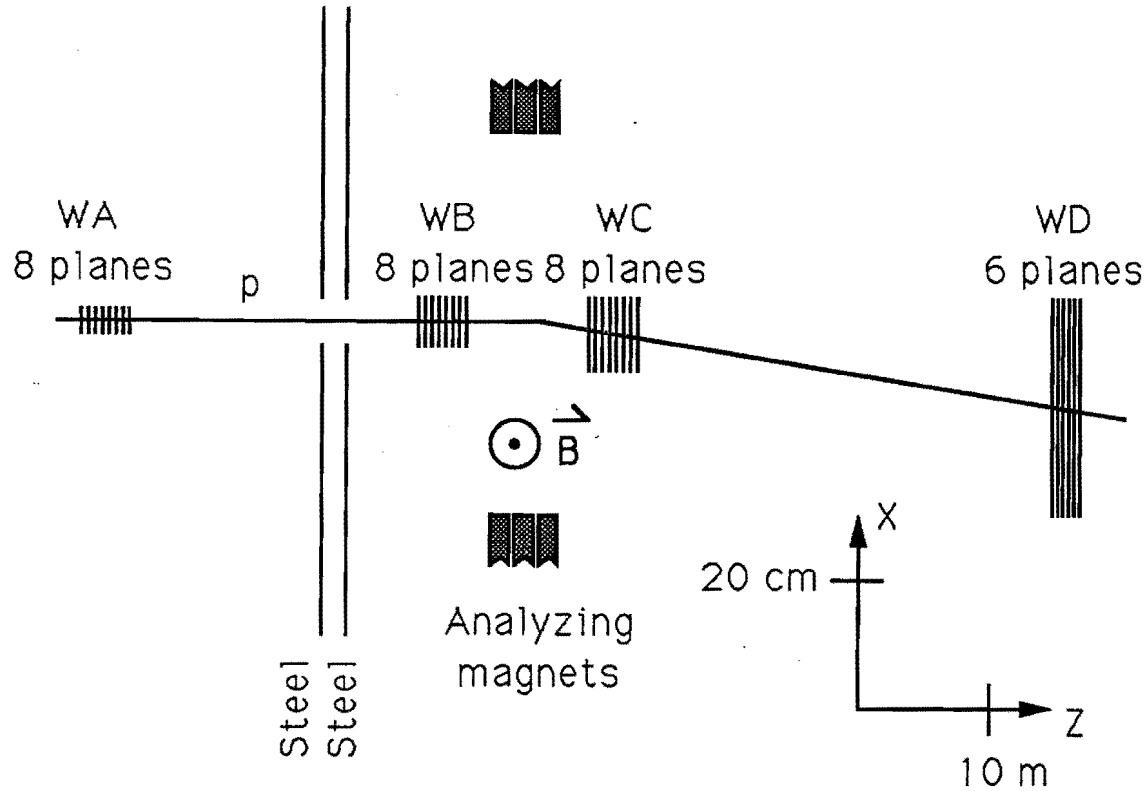

Figure 2.6: The baryon spectrometer (plan view) used to measure the proton track.

2.5 Baryon Spectrometer

The baryon spectrometer was used to measure the proton track and momentum. A schematic diagram of the baryon spectrometer is given in Fig 2.6. It is made up of four stations of proportional wire chamber (WA, WB, WC and WD) and three BM109 magnets (analyzing magnets.) The three stations, WA, WB and WC were each made up eight planes of proportional wire chamber X, Y, X, Y, U, V, U and V where U and V were rotated $\pm 45°$ with respect to X and Y. The wire spacing for WA, WB and WC was 1 mm. The WD station was made up of six planes X, Y, X, Y, U and V. The wire spacing for the WD station was 2 mm. The combined p_t kick of the analyzing magnets was -2.46 GeV/c. The momentum resolution (σ_p/p) of the baryon spectrometer was 0.2%. The angular resolution (σ) was 9 μrad in horizontal

(x) angle and 6 μrad in vertical (y) angle. These resolutions are the errors determined from the error matrix of the fit tracks appropriately increased by the square root of reduced χ^2. The resolution of each plane used in the fit is the wire spacing divided by $\sqrt{12}$.

2.6 Missing Neutral Mass Squared Resolution

Using a Monte Carlo calculation of our apparatus to simulate the experiment we can reconstruct the missing neutral (π^0 or γ) mass squared assuming $\Sigma^+ \rightarrow pX$. The resolution from the Monte Carlo calculation using only the hyperon and baryon spectrometers was 0.0026 GeV^2/c^4. There was a seven standard deviation separation between $m^2_{\pi^0}$ and m^2_γ. However, we expected in the real data, there would be non-Gaussian contributions in the tails making this separation much less clear.

2.7 Photon Spectrometer

The photon spectrometer was used to measure the photon position and energy. It was a separated-function detector, that is, the energy measurement and the position measurement were made in different detectors. A diagram of the photon spectrometer is given in Fig 2.7. The photon would initiate a shower in one of two 1 inch thick steel plates. Each steel plate was 1.44 radiation lengths thick. The probability of a photon initiating a shower in the steel plates was about 89conversion length or 9/7 times the radiation length. This was confirmed by the Electromagnetic Gamma Shower (EGS3) Monte Carlo. We used steel instead of lead because steel was much easier to work with than lead. For the size of steel we wanted lead would not have been as self-supporting as steel. We could also get steel in a uniform thickness of any size. There was a 7.5 $\times$ 7.5 cm^2 hole in each steel plate to let the protons pass through. Behind each steel plate was one proportional wire chamber (PWC) and two modules of transition radiation detector (TRD.) Each PWC was a normal wire chamber (XY readout) with 2 mm wire spacing. The TRD were special chambers plus radiators used to measure the position of the high-energy charged component of

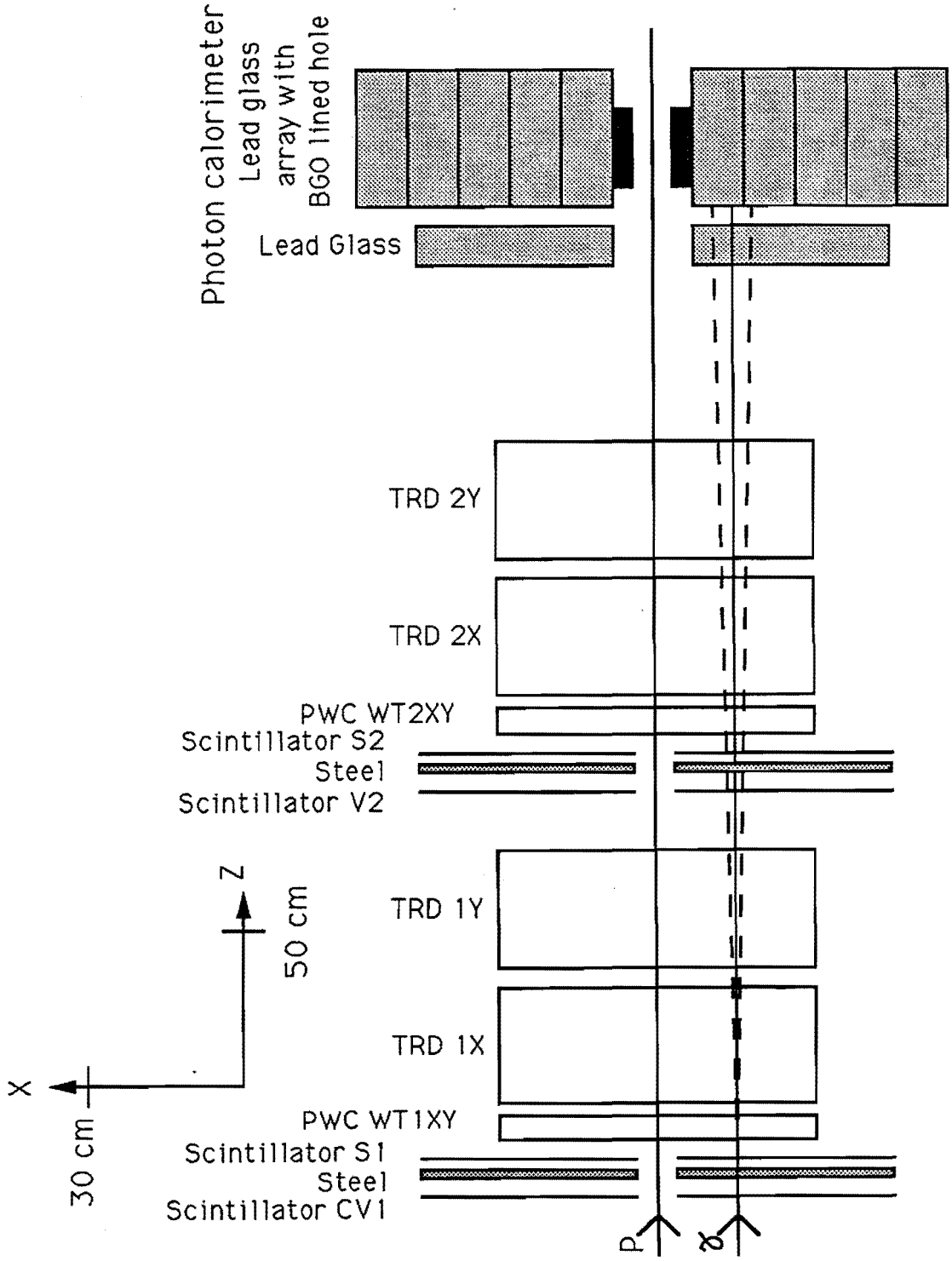

Figure 2.7: The photon spectrometer. A photon showers in the steel plates. The position of the photon is measured in PWC and TRD. The photon energy is measured in a lead glass, BGO calorimeter.

the shower [49]. A schematic diagram of one module of TRD is shown in Fig 2.8.

The position of the photon was measured by initiating an electromagnetic shower in one of the steel plates. Within this shower there was usually a high-energy e^- (in this section when e^- is written this also means e^+) produced. This e^- follows closely the original photon direction. The angle between the e^- and the original photon direction is $\sim m_e/E_e$ where m_e is the mass of the electron and E_e is the energy of the e^-. When a high-energy charged particle (e^- in this case) crosses a dielectric media boundary, it produces transition radiation X-rays. In E761 the dielectric media was a radiator consisting of 210 polypropylene foils 17 μm thick with 1 mm air gaps between them. The transition radiation X-rays also follow closely the e^- trajectory. The angle between the transition radiation X-rays and the original photon direction is $\sim m_e/E_e$. The position of these X-rays was measured in wire chambers that used a gas mixture of 70% Xe and 30% CH_4. To insure uniform gas gain throughout the chamber we used special compensating gas volumes. CO_2 was flowed at a slightly higher pressure on both sides of the cathode planes. This prevented the cathode planes from bulging out due to the higher density of Xe with respect to air. The response of one module of TRD versus Lorentz γ factor [49] is given in Fig 2.9. As can be seen the TRD is sensitive to e^- with energies above 2.5 GeV. The average energy of the photon for $\Sigma^+ \rightarrow p\gamma$ is $\sim$ 50 GeV. From Fig 2.9 the average number of pulses from an e^- with an energy greater than 2.5 GeV is $\sim$2. Each module of TRD measured either X or Y and had 2 mm wire spacing. The normal PWC was used to supplement the information from the TRD. There was a total of 8 planes of PWC and TRD in the photon spectrometer. The active area of these chambers was 57.6×57.6 cm^2.

The photon energy was measured in a photon calorimeter and a rear lead glass array. The photon calorimeter consisted of 3 arrays, front lead glass, main lead glass and BGO. See Fig 2.2.

The front lead glass consisted of 16 blocks of lead glass arranged as a wall shown in Fig. 2.10. The F2 type blocks were $10.08 \times 10.08 \times 38.4$ cm^3. The radiation length of the blocks was 3.2 cm. The array covered an area approximately 80×80 cm^2. The thickness of the array along the beam direction was 10.08 cm. There was a hole 12.5×12.5 cm^2 in the front wall to let the protons pass through.

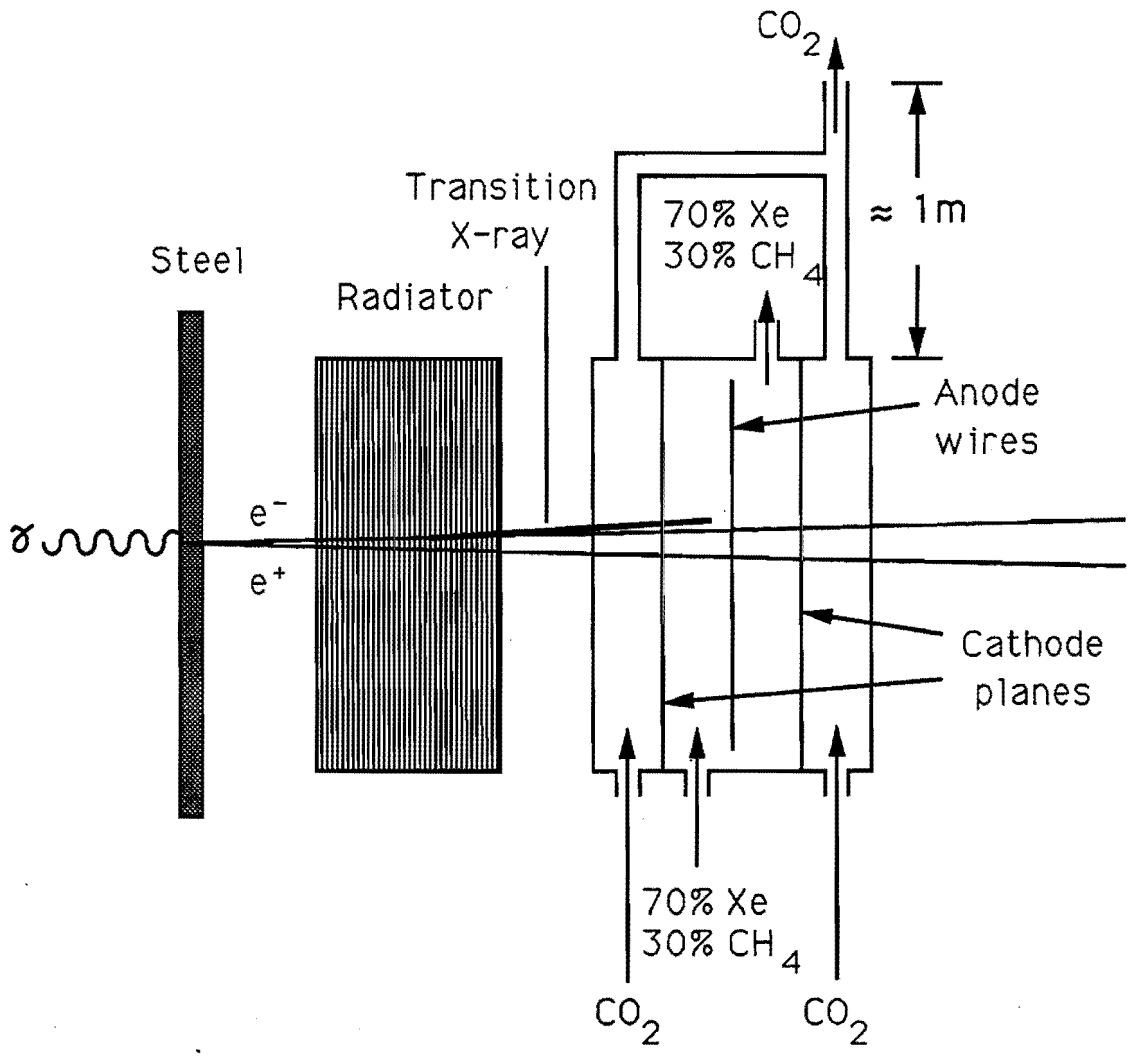

Figure 2.8: Schematic cross section of one module of TRD. Not drawn to scale.

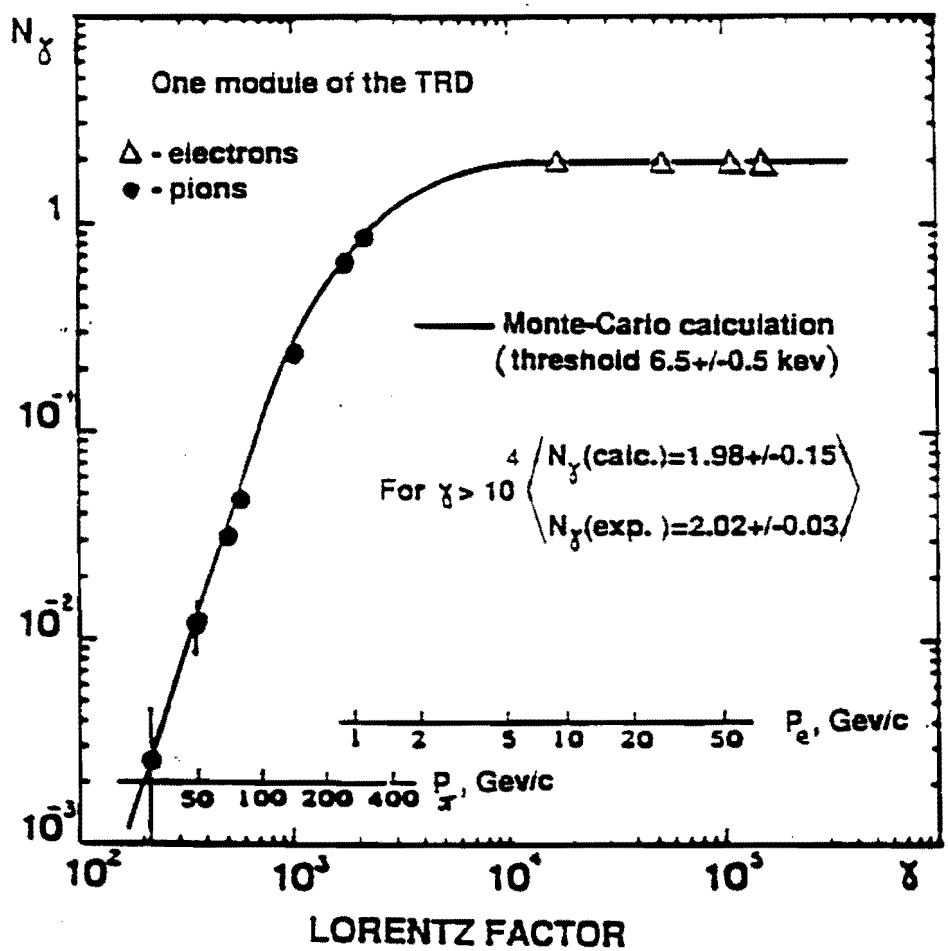

Figure 2.9: Average number of transition radiation X-rays, N_γ, detected per module of TRD as a function of Lorentz γ factor for e^- and π^- [49].

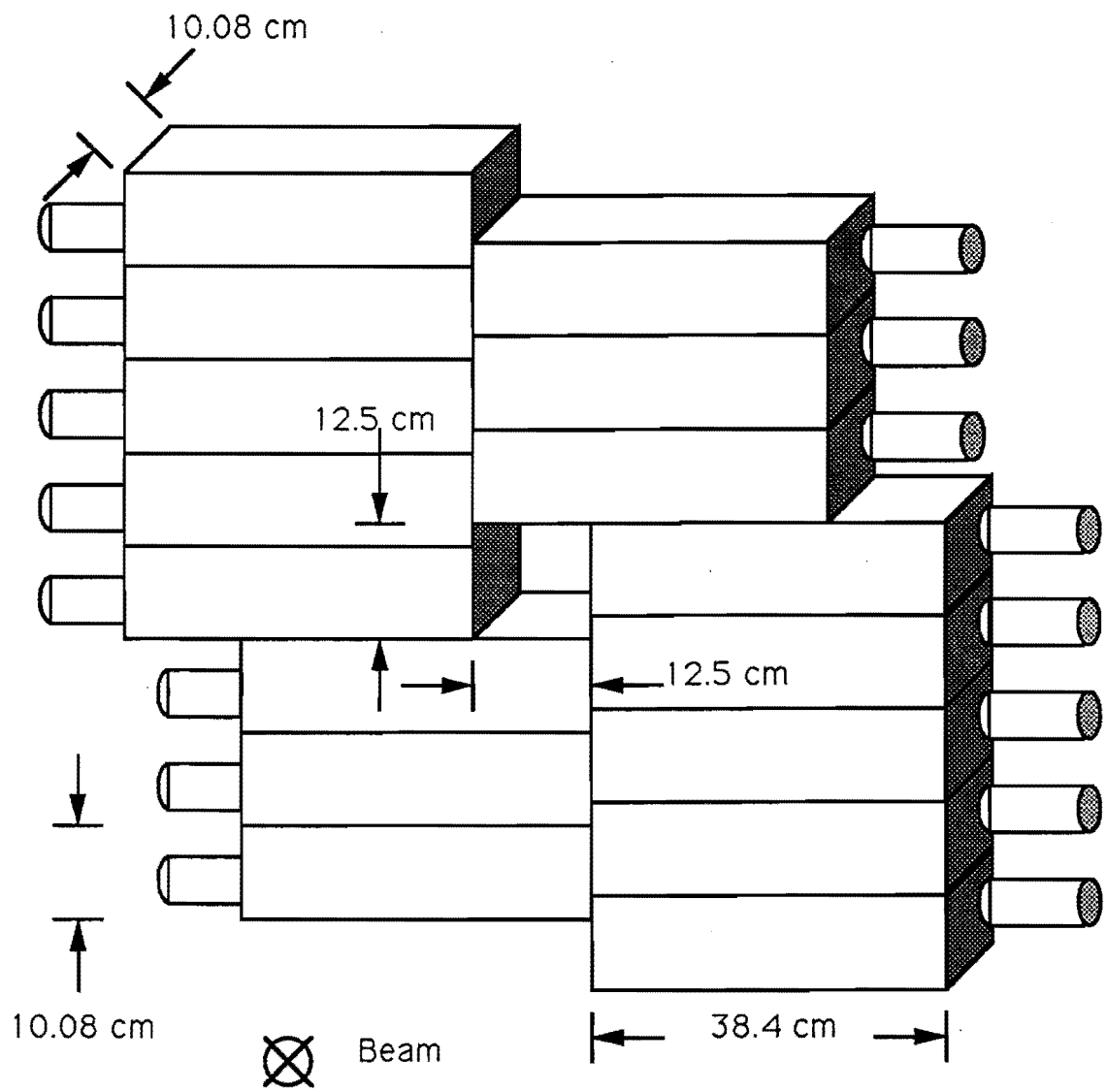

Figure 2.10: The front lead glass wall. The hole is to let protons pass through.

The main array lead glass consisted of 76 lead glass blocks arranged as in Fig. 2.11. These blocks are of the same type as for the front lead glass array. For the main array the blocks were stacked with their long axis along the beam direction. This array covered an area approximately 90 $\times$ 90 cm^2. The thickness of the array along the beam direction was 12 radiation lengths plus 3.2 radiation lengths for the front wall. We would like to thank the Rutgers group for loaning us their lead glass.

There was a hole 12.5 $\times$ 12.5 cm^2 within the main lead glass array. This hole was lined with BGO ($Bi_4Ge_3O_{12}$) crystals. The crystals were 2.50 $\times$ 2.50 $\times$ 20.0 cm^3. The long axis of the crystals was along the beam direction. The radiation length of BGO is 1.12 cm. This means that there was 17.9 radiation lengths of BGO along the beam direction. There was a hole in the BGO array 7.5 $\times$ 7.5 cm^2 to let the protons pass through.

The size of the hole in the steel plates and the BGO was determined as follows. In the laboratory frame the angular distribution of the decay proton and photon is centered about the hole. Because the photon has zero rest mass its decay cone is a full sphere. That is a photon can come off at any angle in the laboratory frame. The proton distribution on the other hand has a maximum opening angle. Using a Monte Carlo calculation the size of the hole was determined that maximized the number of decay protons that go into the hole and the number of photons that are outside the hole. This size was found to be 7.5 $\times$ 7.5 cm^2. BGO was used to line the hole because of its short radiation length. The BGO could contain showers that initiated much closer to the hole than if lead glass were used.

For photons that did go into the hole a rear lead glass array was set up $\sim$53 m downstream of the main lead glass array. A diagram of the rear lead glass array is given in Fig. 2.12. Just downstream of the main lead glass array were 3 magnets with a horizontal aperture of 61 cm and a vertical aperture of 20 cm. These magnets swept the protons away from the photons. Therefore the rear lead glass array would not intercept any of these protons. The rear lead glass array consisted of 4 blocks 20 $\times$ 20 $\times$ 40 cm^3 each. The long axis was along the beam direction.

Helium-filled polyethylene bags were placed within the decay volume (between

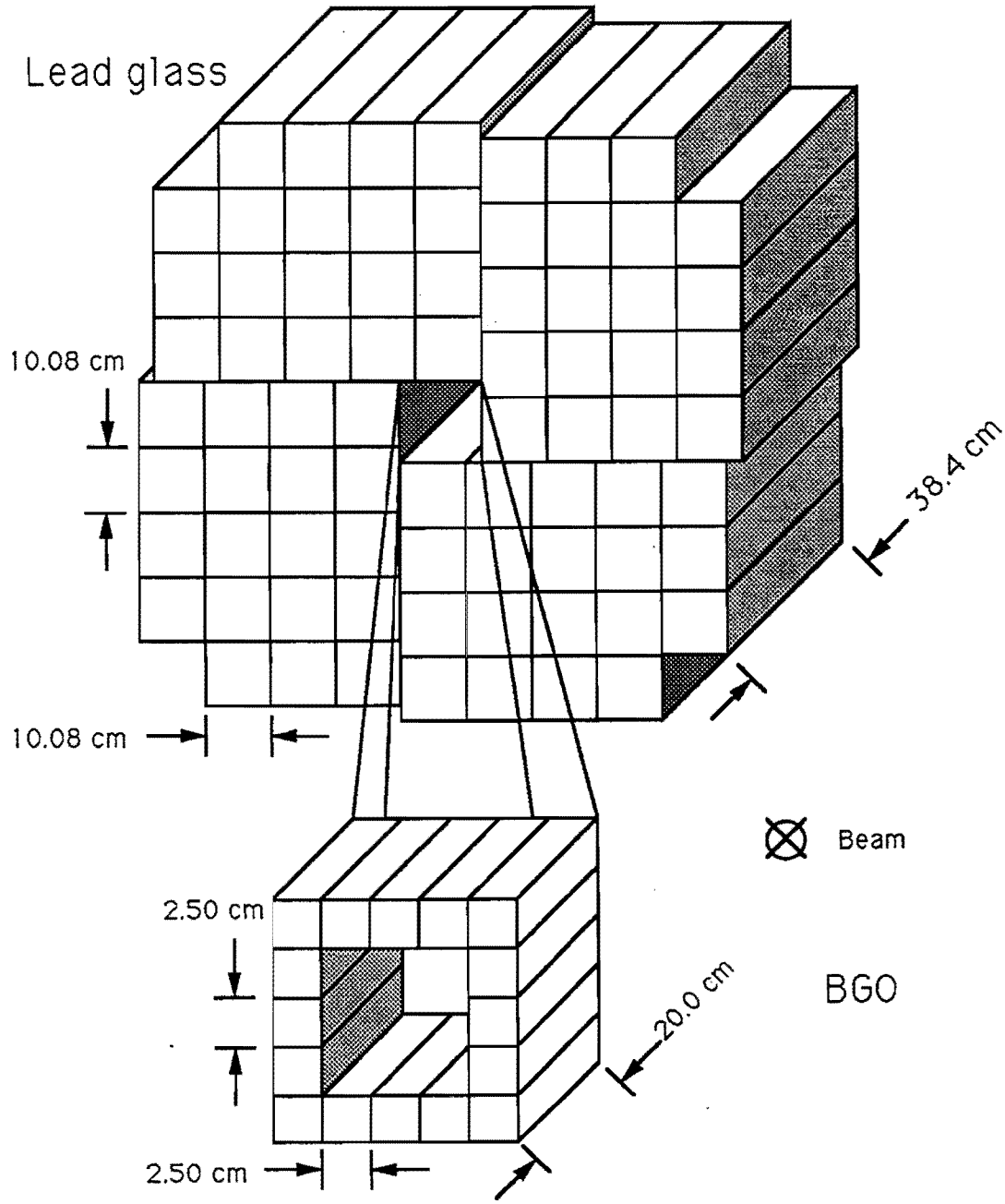

Figure 2.11: The main lead glass array with BGO lining the hole. The hole lets protons pass through.

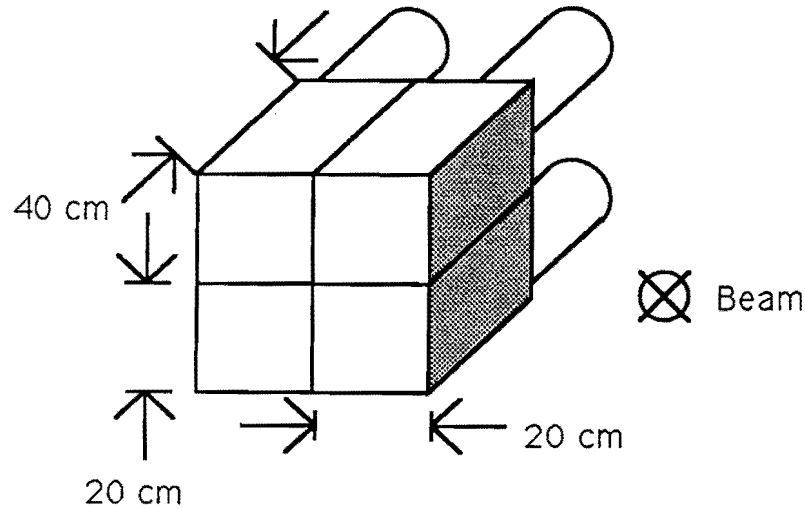

Figure 2.12: The rear lead glass array used to measure the energy of photons that went into the hole of the main lead glass array.

SD3 and WA) and between WA station and the first steel plate in the photon spectrometer. These were used to reduce the effects of multiple coulomb scattering thereby improving the resolution of the baryon spectrometer. It also reduced the number of interactions that could produce photon triggers.

Chapter 3

Trigger and Data Acquisition System (DAQ)

The goal of the experiment was a high precision measurement of the asymmetry parameter and branching ratio of $\Sigma^+ \rightarrow p\gamma$. The dominant background at the trigger level was interactions producing photons and $\Sigma^+ \rightarrow p\pi^0$ with $\pi^0 \rightarrow \gamma\gamma$ decays. They were approximately equal at the trigger level. After event reconstruction the dominant background was $\Sigma^+ \rightarrow p\pi^0$ with $\pi^0 \rightarrow \gamma\gamma$. The $\Sigma^+ \rightarrow p\pi^0$ background was useful for 3 reasons. One, we needed it to measure the polarization of the Σ^+ beam. The α parameter for the decay $\Sigma^+ \rightarrow p\pi^0$ is known. Therefore the polarization can be determined from the angular distribution of the decay proton given by equation 1.1. Two, it was needed as the normalization for the branching ratio. By measuring the number of $\Sigma^+ \rightarrow p\pi^0$ decays we could determine the number of Σ^+ in the beam given the known branching ratio of $\Sigma^+ \rightarrow p\pi^0$. Three, it was useful to perform systematics studies. It was also useful for studying detector response. For these reasons our philosophy for the trigger was to make no online cuts to remove $\Sigma^+ \rightarrow p\pi^0$ events. The Data Acquisition system (DAQ) was built such that it could record the large rate of interactions and $\Sigma^+ \rightarrow p\pi^0$ decays to tape along with the small number of $\Sigma^+ \rightarrow p\gamma$.

The idea of the trigger was to require each particle in the decay $\Sigma^+ \rightarrow p\gamma$. We used scintillation counters to require a particle go through the hyperon and baryon

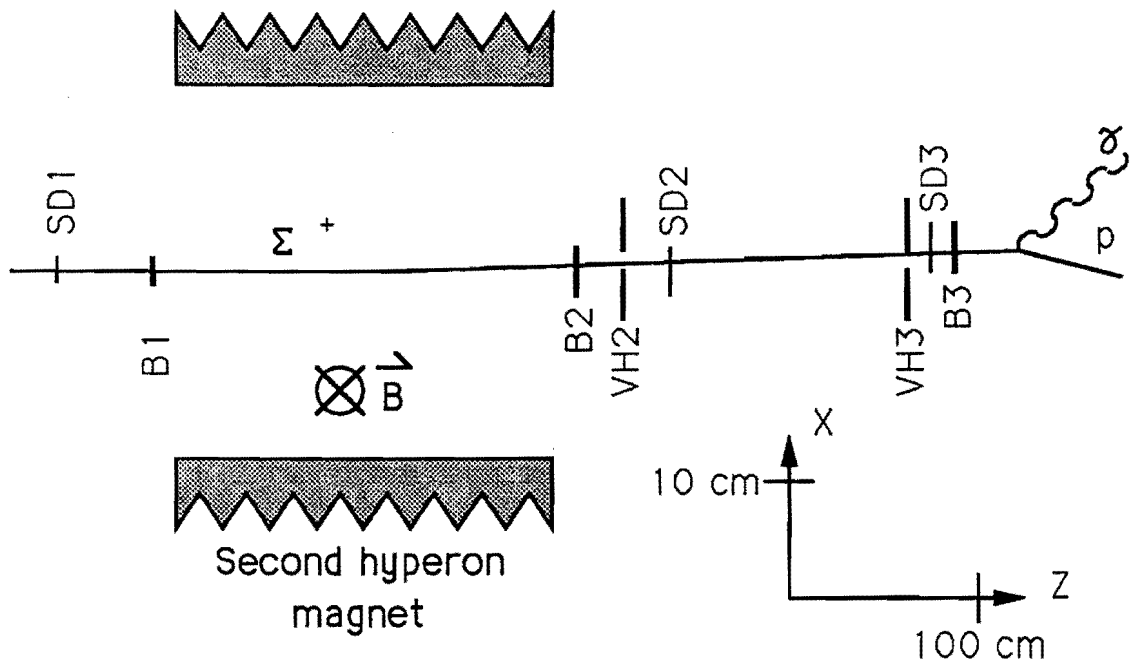

Figure 3.1: The position of the T1 trigger scintillators within the hyperon spectrometer. T1 was defined as $T1 \equiv B1 \cdot B2 \cdot B3 \cdot \overline{VH2 + VH3}$.

spectrometers. We required a neutral shower start in the steel plates. We demanded there be >5 GeV of energy in the photon calorimeter. We also accepted about ~1% of beam tracks for alignment checks and studies.

3.1 Trigger

The trigger was set up in a three level system, T1, T2 and T3. Each level was a requirement that there be one particle from the decay $\Sigma^+ \rightarrow p\gamma$. Each level of the trigger required the previous level to fire. A T3 trigger finally caused the event to be readout.

3.1.1 T1

The T1 trigger is shown in Fig. 3.1. The T1 trigger was a coincidence of scintillation

counters requiring a beam track within the phase space of the beam exiting the hyperon magnet channel. The T1 trigger was defined as

$$T1 \equiv B1 \cdot B2 \cdot B3 \cdot \overline{VH2 + VH3}$$

where B1, B2, B3, VH2 and VH3 were scintillation counters within the hyperon spectrometer. We ran the experiment with ~100,000 T1 triggers per second through the apparatus.

3.1.2 T2

The second level trigger, T2, required a photon in the event. At first the trigger counters were placed in the configuration shown in Fig. 3.2 This preliminary T2 trigger was defined as

$$\begin{aligned} T2 \equiv T1 \quad \cdot \quad & [(\overline{CV1} \cdot CS3) + \\ & (\overline{CV1} \cdot \overline{CS3} \cdot (> 10\text{GeV rear lead glass}))] \end{aligned}$$

where CV1 and CS3 are scintillation counters in the photon spectrometer and >10 GeV rear lead glass means there must be more than 10 GeV of energy deposited in the rear lead glass array. The trigger rate for this trigger was 7% of the beam rate (T1.) This was much too high to perform the experiment. Most of these events were interactions and thus not useful. We started with this trigger because it would be very efficient for photons. There were 3 radiation lengths of steel and 3 radiation lengths of lead glass before the trigger scintillation counter CS3. Therefore virtually all photons would have converted by CS3. What we found was that there were too many interactions of the beam in the material after the veto counter CV1 and before CS3. Also there were many interactions that deposited energy in the rear lead glass array.

The first trigger improvement was to place the trigger counters on either side of the steel plates. See Fig. 3.3 for a diagram of the final position of the T2 trigger counters. A T2 trigger was now defined as

$$T2 \equiv T1 \quad \cdot \quad [(\overline{CV1} \cdot S1) +$$

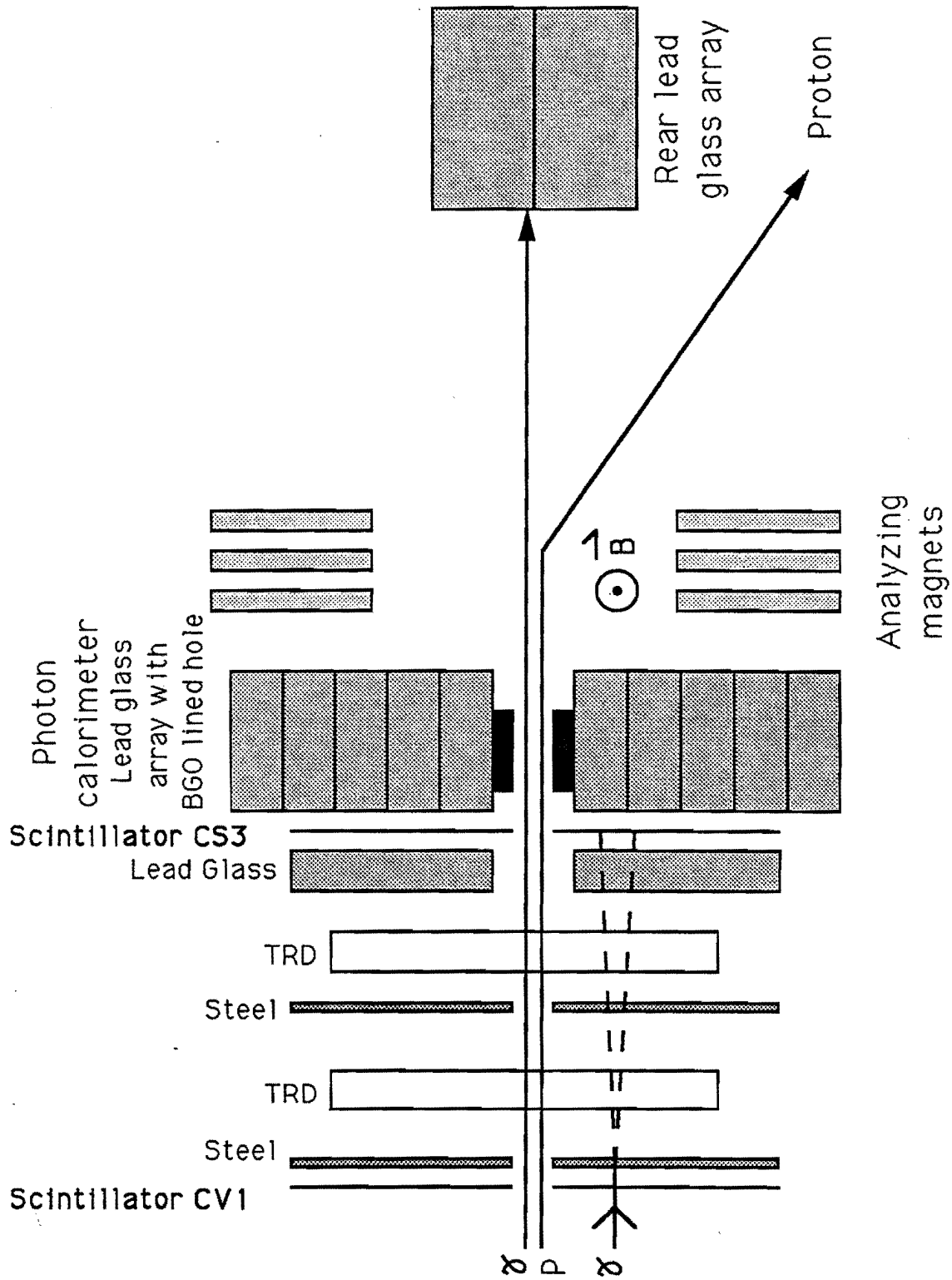

Figure 3.2: The position of the T2 trigger scintillation counters within the photon spectrometer at the start of the run. Not drawn to scale.

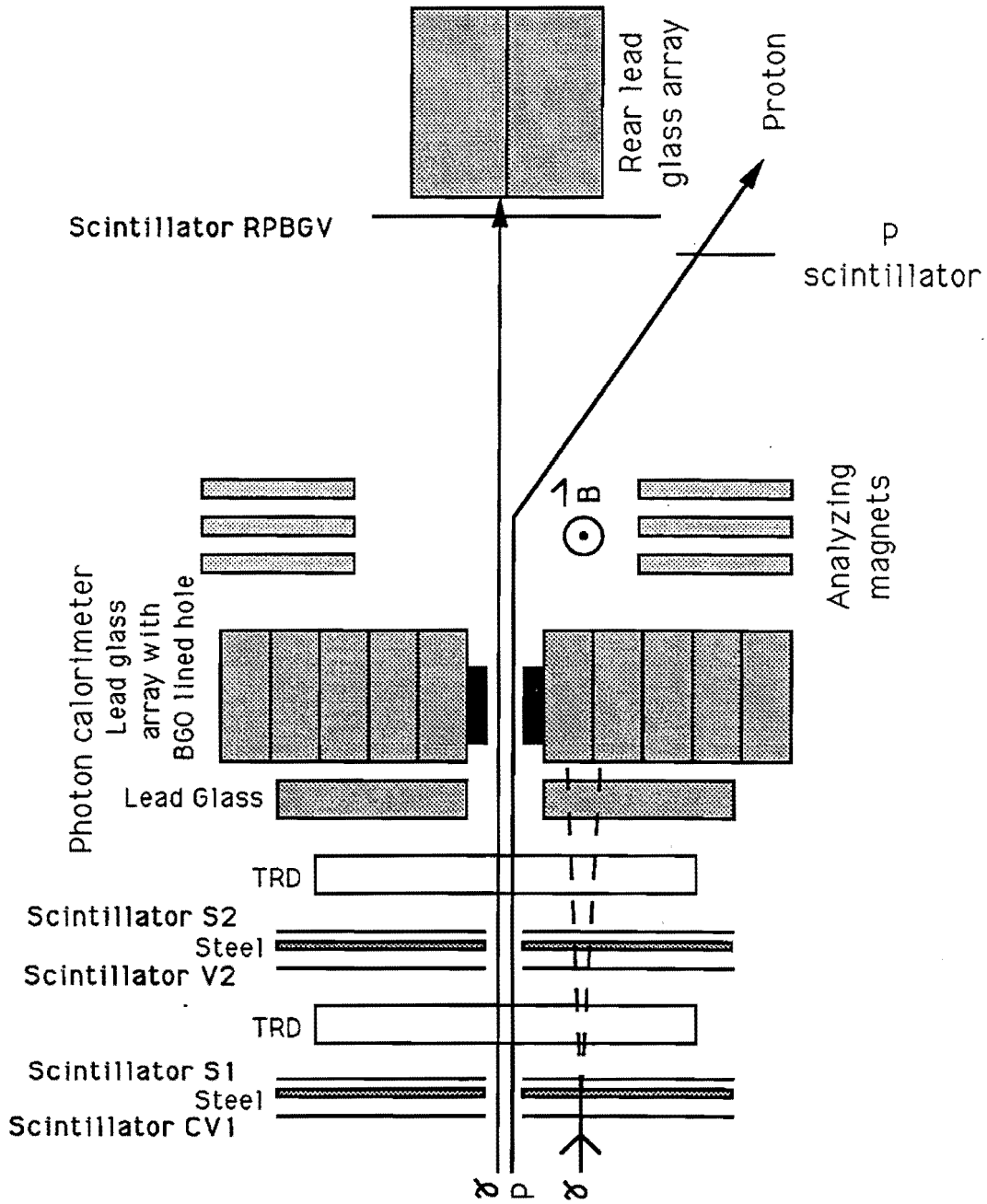

Figure 3.3: The final position of the T2 trigger scintillators within the photon spectrometer. Not drawn to scale.

$$(\overline{V2} \cdot S2) +$$
$$(\overline{CV1} \cdot \overline{S1} \cdot \overline{V2} \cdot \overline{S2} \cdot (> 10\text{GeV rear lead glass}))]$$

where CV1, S1, V2 and S2 are scintillation counters shown in Fig. 3.3. The trigger rate was now 4% of the beam rate. This now required a neutral particle to shower in the steel plates. One problem with this trigger was that interactions downstream of the analyzing magnets would deposit energy in the rear lead glass array. To remove at least charged particles depositing energy in the rear lead glass array we installed a scintillation counter, RPBGV, in front of the rear lead glass array. We put it in veto in the third component of the T2 trigger, ie

$$\begin{aligned} T2 \equiv T1 \quad \cdot \quad & [(\overline{CV1} \cdot S1) + \\ & (\overline{V2} \cdot S2) + \\ & (\overline{CV1} \cdot \overline{S1} \cdot \overline{V2} \cdot \overline{S2} \cdot \overline{RPBGV} \cdot (> 10\text{GeV rear lead glass}))] \end{aligned}$$

The trigger rate of this trigger was then 2.5% of the beam rate.

Another problem we had with the trigger was scraping of the beam on the steel plates. This was a problem because the size of the beam was the same size horizontally as the hole in the steel plates. A particle would miss the veto counter scintillator, CV1, near the edge but hit the edge of the steel plate. This would initiate a shower and mimic the trigger. To remove these events we made the hole in the CV1 veto counter smaller horizontally by installing a small counter just at the edge of the hole. This smaller scintillator was put in OR with CV1. The hole in the scintillator was made 65 mm horizontally and the size of the hole in the steel plate was 75 mm. CV1 veto was also put in veto for showers in the second piece of steel, ie

$$\begin{aligned} T2 \equiv T1 \quad \cdot \quad & [(\overline{CV1} \cdot S1) + \\ & (\overline{CV1} \cdot \overline{V2} \cdot S2) + \\ & (\overline{CV1} \cdot \overline{S1} \cdot \overline{V2} \cdot \overline{S2} \cdot \overline{RPBGV} \cdot (> 10\text{GeV rear lead glass}))] \end{aligned}$$

The trigger rate for this trigger was 2% of the beam rate.

The next improvement in the trigger was the addition of a P (for proton) scintillation counter in the level three trigger. See next section on T3 trigger. The trigger

would require a high momentum charged track, a proton from the decay $\Sigma^+ \rightarrow p\gamma$ or $\Sigma^+ \rightarrow p\pi^0$. See Fig. 3.3 for the position of the P counter. The kinematics of $\Sigma^+ \rightarrow p\gamma$ and $\Sigma^+ \rightarrow p\pi^0$ are so similar that the phase space of the protons overlap for both decays. The resulting trigger rate was 1.7% of the beam rate.

We determined that the rear photon trigger, ie the component of the T2 trigger

$$\overline{\mathrm{CV1}} \cdot \overline{\mathrm{S1}} \cdot \overline{\mathrm{V2}} \cdot \overline{\mathrm{S2}} \cdot \overline{\mathrm{RPBGV}} \cdot (> 10\mathrm{GeV\ rear\ lead\ glass})$$

did not contain much useful physics. We analyzed these events during the run and found that many of the events did not reconstruct as $\Sigma^+ \rightarrow p\pi^0$. These triggers were dominated by interactions in the air upstream of the rear lead glass array. For the asymmetry parameter measurement they were useless. A rear photon trigger from $\Sigma^+ \rightarrow p\gamma$ means the decay proton went backwards in the center of mass ($\cos\theta_z^{cm} \approx -1$). θ_z^{cm} is the angle between the z-axis and the proton direction in the center of mass. If $\cos\theta_z^{cm} \approx -1$ then $\cos\theta_y^{cm} \approx 0$. The asymmetry parameter measures the slope in the $\cos\theta_y^{cm}$ plot. Events at $\cos\theta_y^{cm} = 0$ have no analyzing power in the determination the slope of the distribution. Also, because the photon went into the hole in the steel plate, the TRD can not be used to measure the position of the photon. It would be difficult to isolate $\Sigma^+ \rightarrow p\gamma$ in rear photon triggers. For these reasons we prescaled rear photon triggers by a factor of four. We accepted one in every four rear photon events. The final T2 trigger was

$$\begin{aligned} \mathrm{T2} \equiv \mathrm{T1} \ \cdot \ & [(\overline{\mathrm{CV1}} \cdot \mathrm{S1}) + \\ & (\overline{\mathrm{CV1}} \cdot \overline{\mathrm{V2}} \cdot \mathrm{S2}) + \\ & (\overline{\mathrm{CV1}} \cdot \overline{\mathrm{S1}} \cdot \overline{\mathrm{V2}} \cdot \overline{\mathrm{S2}} \cdot \overline{\mathrm{RPBGV}} \cdot (> 10\mathrm{GeV\ rear\ lead\ glass}))\mathrm{prescaled\ 4}] \end{aligned}$$

This gave a final trigger rate of 1.4% of the beam rate.

3.1.3 T3

The T3 level trigger would begin the readout of the event. The T3 trigger required a high momentum downstream track. The T3 trigger started out as

$$\mathrm{T3} \equiv [\mathrm{T2} \cdot \mathrm{P} \cdot \mathrm{RATP}] + \mathrm{T1PS}$$

where P is a scintillation counter behind wire chamber WD where the protons went, RATP is the rationer and T1PS is a T1 prescale event (1 in 8192 T1 triggers.) The P counter required a particle in the baryon spectrometer. The rationer, RATP, was used to require that 2 particles did not go through the apparatus within a 400 nsec time window. The 400 nsec time window was to cover the drift time in the TRD. The T1PS trigger rate was ~1% of the T3 trigger rate and thus caused no problem in terms of deadtime. We used The T1PS events for alignment and detector studies.

The last improvement to the trigger was to add to level T3 a minimum energy cut on the energy deposited in the photon calorimeter and rear lead glass array. We required > 5 GeV energy in the photon calorimeter or the rear lead glass array. The final T3 trigger was

$$\mathrm{T3} \equiv [\mathrm{T2} \cdot \mathrm{P} \cdot \mathrm{RATP} \cdot > 5\mathrm{GeV\ energy\ in\ photon\ calorimeter}] + \mathrm{T1PS}$$

This removed events where a low energy photon was produced in an interaction. The final T3 trigger rate was ~0.8% of the beam rate. Twenty-four percent of T3 triggers reconstructed as good $\Sigma^+ \rightarrow p\pi^0$.

3.1.4 Trigger Hardware

The first and second level of trigger were set up in the experimental enclosure (PC4) with the detector. This made it impossible to make adjustments to the trigger while the proton beam was on. The first level trigger would need to make a decision within 900 nsec of a particle passing through the SSD. The time 900 nsec is the maximum amount of time that the data from the SSD and PWC could be stored in the readout electronics. This did not allow us enough time to send the signals to the counting room and back to the SSD and PWC. Therefore the first and second level triggers was placed next to the apparatus. The third level trigger was set up in the counting room where one could make adjustments while the proton beam was on.

The trigger was constructed around a LeCroy model 4508 Programmable Lookup Unit (PLU) [50]. This unit was a programmable CAMAC module under control from a Digital Equipment Corporation VAX 11/780 computer. See Fig. 3.4. Changing the trigger involved running a program on the VAX to download a different trigger to the

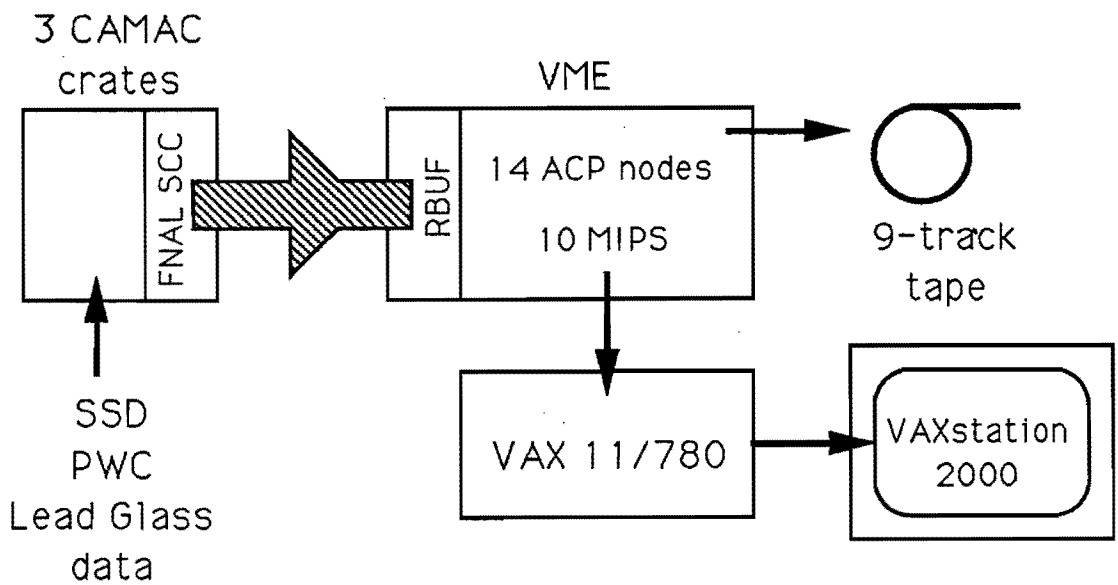

Figure 3.4: Schematic diagram of the E761 DAQ system. Data from the detectors were readout of CAMAC into ACP nodes. Data were then written to 9-track tape. Some of the data were transferred to a VAX 11/780 for monitoring.

PLU. A new trigger could be downloaded between beam spills (~40 sec) This was a convenient and quick way to change the trigger.

3.2 DAQ

E761 ran during the first half of the Fermilab 1990-1992 fixed target run. The data for the results presented here were collected during one month of running in May 1990. A schematic diagram of the the Data Acquisition (DAQ) system is shown in Fig. 3.4. There were ~5,000 channels of silicon strip detector (SSD) and ~5,500 channels of proportional wire chamber (PWC) data read into our Chamber ReadOut System (CROS.) The CROS was a CAMAC based readout system built by the St. Petersburg Nuclear Physics Institute. There was 112 channels of photon calorimeter Analog to Digital Converters (ADC), 72 channels of scalers and ~60 channels of miscellaneous ADC, Time to Digital Converters (TDC) and latches.

A T3 trigger began the readout of an event. Data were read from CAMAC

by a Fermilab Smart Crate Controller (SCC) [51, 52, 53, 54] to a buffer memory (RBUF) [55, 56] in a VME crate. Each event was ~600 bytes long and took ~600 μsec to readout. We were able to readout ~15,000 events per 23 second spill at 50% deadtime.

Data were transferred from the RBUF into 1 of 14 ACP (Advanced Computer Program) [57, 58] nodes. Each node was running a version of the offline reconstruction. We were able to do a full reconstruction of ~10% of the data online. This was invaluable in helping to monitor detector performance. This ACP "farm" had ~10 Million Instructions Per Second (MIPS) of compute power. Analyzed events were then sent to a VAX 11/780 and a VAXstation 2000 for monitoring the experiment.

All data were written out to 6250 bpi 9-track tape. We were able to write 2-3 tapes per hour. Runs were taken in the following cycle, +, -, - and + targeting angle. Each run was 3 tapes long. Once a day we would take alignment runs. These were runs where the trigger was just a beam particle (T1 trigger.) Alignment runs were taken with all combinations of the magnets on and off. These runs were used to align the apparatus. In one month of running we wrote 872 tapes (221 million triggers) at + and - targeting angles.

3.3 Summary

We made many improvements to the trigger before we started taking data. As we made improvements, the trigger rate would go down and thus we would increase the intensity of the proton beam on the target to get more decays. At first we started with 4×10^{10} protons/spill on target. When we had the final trigger we were able to run at 8×10^{11} protons/spill on target with reasonable deadtime. We stopped here because we had reached our goal of 15,000 $\Sigma^+ \rightarrow p\gamma$ per week. Also we could no longer increase the intensity of the beam because we were limited to 1×10^{12} protons/spill because of radiation in our counting rooms.

Chapter 4

Data Analysis

4.1 Outline

The data analysis scheme is shown in Fig. 4.1. The first step was to align the Silicon Strip Detectors (SSD), Proportional Wire Chambers (PWC) and the Transition Radiation Detectors (TRD.) The next step was to perform the momentum calibration of the magnets. This involved assigning to each magnet its p_t kick (magnetic field integral.) Finally the energy calibration of the photon calorimeter was performed. This involved determining the constants to multiply the signal from the calorimeter blocks to yield the energy in each block. After these jobs were completed the data were analyzed on the Amdahl mainframe computer at Fermilab. This analysis, Pass 1, took about 5 weeks to complete.

4.2 Alignment

The goal of the alignment was to bring all of the planes (SSD, PWC and TRD) into one overall consistent coordinate system [59, 60]. See Fig 2.2 and section 2.3 for a discussion of the coordinate system used. This involved an iterative process of changing the alignment constants and then reanalyzing the data again to check the alignment. When the procedure converged the alignment was complete. At first a track was constructed from hits on the 4 planes SD2X, SD2Y, WB2X and WB2Y.

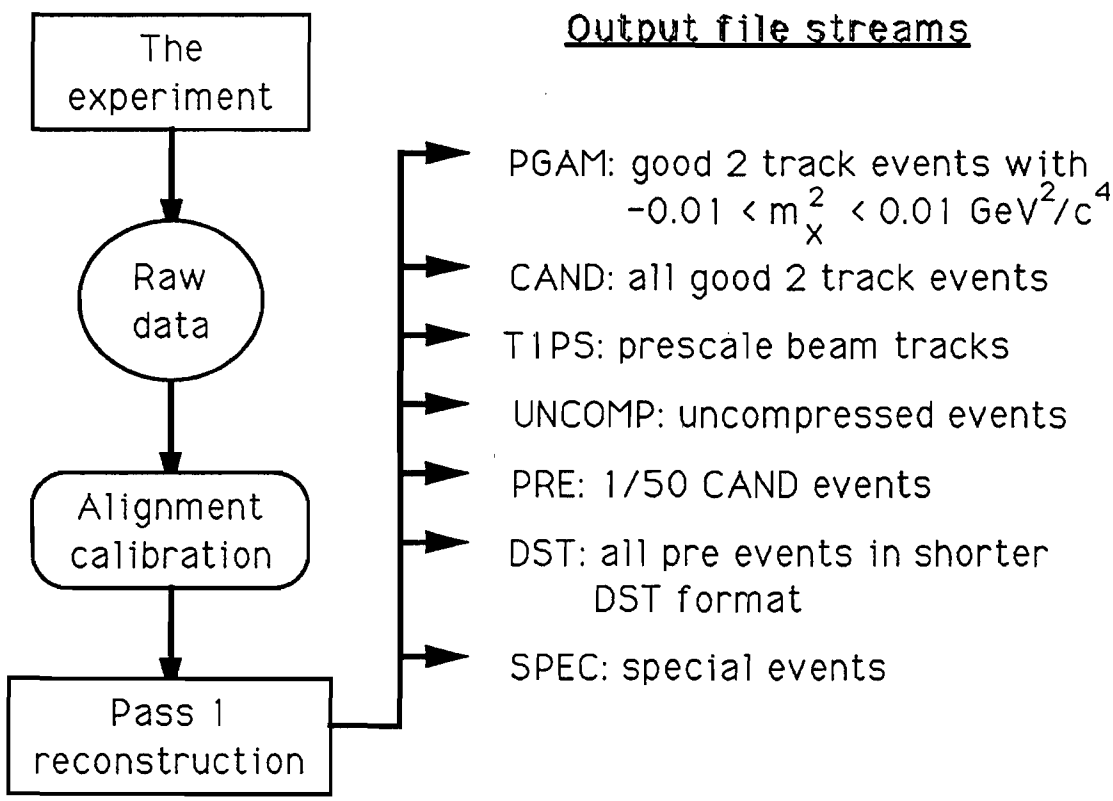

Figure 4.1: Outline of data analysis scheme.

Undecayed beam tracks were used for this. The residual (the difference between the track position and hit) was plotted for each of the planes SD2U, SD3 planes, WA planes, WT planes, TRD planes and the rest of the WB planes. From the residuals distribution, offsets were determined. These offsets were input back into the constants and the alignment procedure performed again. The alignment was complete when all the residuals distribution were 0. The remaining planes in SD1, WC and WD were aligned similarly using data with the second hyperon magnet and 3 analyzing magnets off. The average value of the residual for all of the planes was 0.05σ where σ is the strip spacing or wire spacing divided by the $\sqrt{12}$. The largest residual was 0.17σ.

4.3 Momentum Calibration

To measure the momentum of particles the magnetic field of each of the magnets must be known. Before the experiment was performed field maps were taken of each of the magnets in the experiment. Magnetic field integrals ($\int Bdl$) were then calculated using these data for each magnet. These field integrals were translated into effective p_t kicks of the magnets. To determine the relative calibration of the p_t kicks we measured the momentum of undecayed beam tracks. The momentum measured by the hyperon spectrometer and baryon spectrometer was adjusted to be the same. The absolute momentum calibration was good to 0.3%. This was determined by using the decays $\Sigma^+ \rightarrow p\pi^0$ and reconstructing the missing-mass-squared of the π^0 from the Σ^+ and proton track. The missing-mass-squared was examined as a function of the ratio of proton momentum to Σ^+ momentum. From this method the absolute momentum calibration could be checked.

4.4 Target Reconstruction

Before the experiment was performed the position of our target and the hyperon targeting magnet was measured using accurate surveying instruments. This was then used to determine the position of the target and hyperon magnet in the overall coordinate system of the chambers. The p_t kick of the hyperon magnet was determined

by requiring undecayed beam tracks to originate from the target.

4.5 Photon Calorimeter Calibration

The first step in the calibration of the photon calorimeter lead glass and BGO was to set the high voltage on each block such that 1 minimum ionizing particle would deposit energy equivalent to a certain value of the pulse height from the block in the photon calorimeter (10 counts above pedestal.) Using $\Sigma^+ \rightarrow p\pi^0$, $\pi^0 \rightarrow \gamma\gamma$ events, the gain of each of the blocks was adjusted such that the total energy in the photon calorimeter was equal to the momentum of the π^0 calculated from the Σ^+ and proton tracks. The energy resolution (σ_E/E) of the photon calorimeter was $73\%/\sqrt{E(GeV)}$. The energy resolution of the photon calorimeter is poor compared to what is expected from an ideal lead glass calorimeter, $5\%/\sqrt{E(GeV)}$ [61]. This is not surprising. The gain adjustments used were preliminary and have not been fine tuned. Also our calorimeter was hardly optimized for the best energy resolution. Some of the problems causing the poor performance include; only 18 radiation lengths of material, the first 3 radiation lengths (steel plates) were passive, a hole in the center of the calorimeter and the escape of part of the total energy from the sides.

4.6 Pass1 Reconstruction

Pass1 reconstruction involved reconstructing one hyperon track in the hyperon spectrometer and one baryon track in the baryon spectrometer. A total of 299 runs (872 tapes), 153 at negative targeting angle and 146 at positive targeting angle were analyzed on the Amdahl computer at Fermilab. The analysis took five weeks of real time to perform or 320 Amdahl CPU hours.

For each event, the offline reconstruction program tried to find one track in the hyperon spectrometer and one track in the baryon spectrometer. Each track had associated with it a reduced χ^2 (χ^2/ν) which indicated its goodness-of-fit. The reduced χ^2 for the hyperon track, χ^2_Y/ν, is shown in Fig. 4.2. The average number of degrees-of-freedom of the hyperon spectrometer is $\nu = 4$. For the analysis of the data

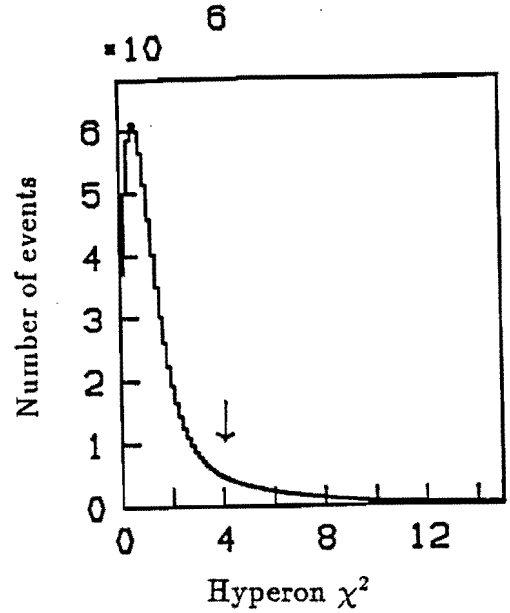

Figure 4.2: Distribution of hyperon track reduced χ^2,χ^2_Y/ν. The average number of degrees-of-freedom is $\nu = 4$. The position of the cut is shown by the arrow.

we made a cut shown in Fig. 4.2 of $\chi^2_Y/\nu < 4$. The reduced χ^2 for the baryon track, χ^2_B/ν, is shown in Fig. 4.3. The average number of degrees-of-freedom of the baryon spectrometer is $\nu = 25$. For the analysis of the data we made a cut shown in Fig. 4.3 of $\chi^2_B/\nu < 2$. The average number of degrees-of-freedom is determined by subtracting the number of parameters determined for each track (five) from the number of planes with a hit found on the track (9 for SSD, and 30 for PWC).

The momentum distribution of the hyperon beam for positive targeting angle is shown in Fig. 4.4. We made a cut in momentum of the hyperon beam of 325 < hyperon momentum < 425 GeV/c.

There are two variables that will be important in the analysis of the asymmetry parameter, TY and TX. TY(TX) is the tangent of the laboratory angle between the hyperon track and the z-axis in the y(x) - z plane at SD3. TY(TX) is also equal to $P_y/P_z(P_x/P_z)$ where P_x, P_y and P_z are the three components of the momentum vector. See Fig. 2.2 and section 2.3 for the definition of the E761 coordinate system used in the offline analysis. The TY distributions for both positive and negative targeting angle are shown in Fig. 4.5. These distributions are very similar. The TX distributions for both positive and negative targeting angle are shown in Fig. 4.6.

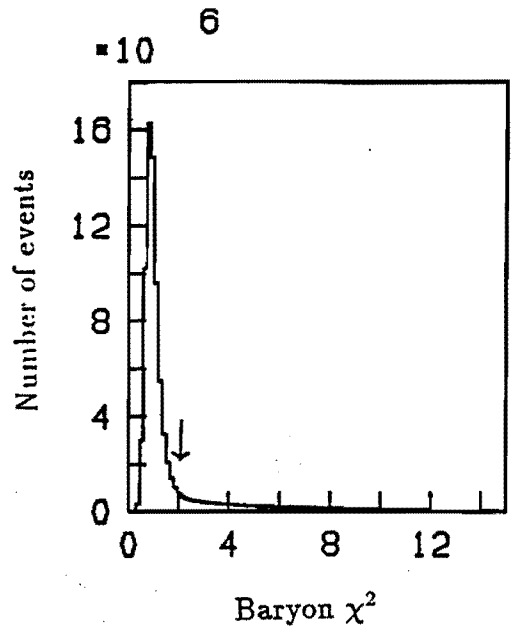

Figure 4.3: Distribution of baryon track reduced χ^2,χ^2_B/ν. The average number of degrees-of-freedom is $\nu = 25$. The position of the cut is shown by the arrow.

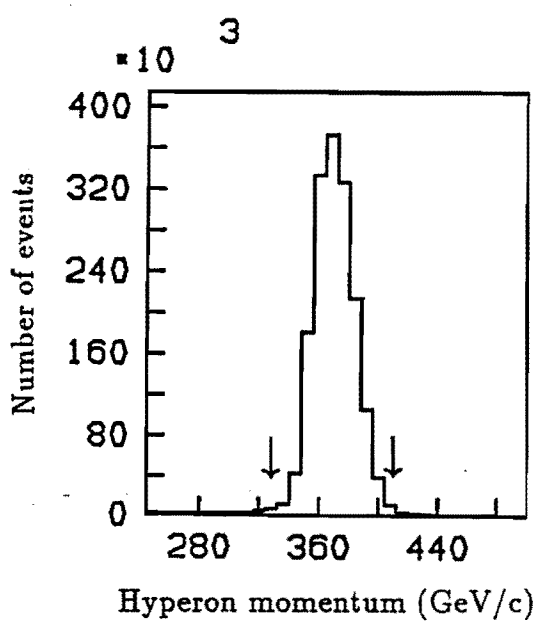

Figure 4.4: Hyperon momentum (GeV/c) distribution for positive targeting angle. The momentum cut shown by the arrows was made in the analysis.

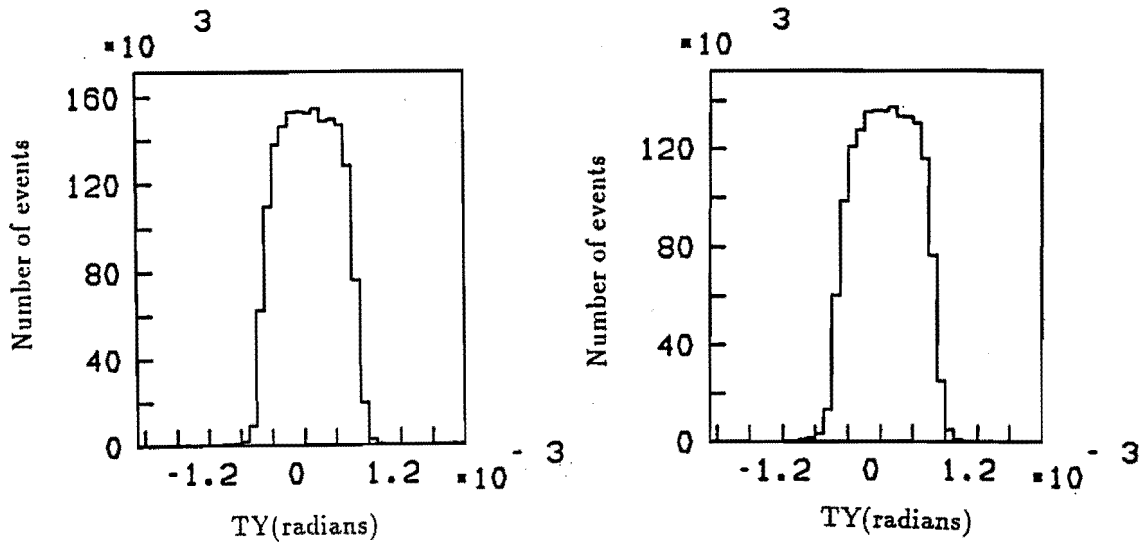

Figure 4.5: Distribution of TY angle (radians) of hyperon for positive(left) and negative(right) targeting angle.

These distributions are quite different. There is a negative(positive) slope for the positive(negative) targeting angle distribution. This is due to the different targeting angles. The different slopes in the TX distributions are caused by the difference in production spectrum for the two targeting angles and the dispersion caused by the hyperon magnet.

The z vertex (z position of the decay of the hyperon track) is defined as the z position of the distance of closest approach of the hyperon and baryon tracks. The z vertex distribution is shown in Fig. 4.7 with respect to SD3, ie SD3 is at $z = 0$ on the plot. The peak at 1400 cm (WA) is due to decays downstream of WA for which the offline reconstruction program assigns the wrong z vertex position. The decay volume is between SD3 and WA. See Fig. 2.2 for a diagram of where the decay volume is located. We make a cut on z vertex of $0 < z$ vertex ≤ 1200 cm.

Another useful plot that we use many times is the θ_{op} - versus - r plot. θ_{op} is the opening angle between the hyperon and baryon track and r is the ratio of the baryon momentum to hyperon momentum. Plotted in Fig. 4.8 is θ_{op} - versus - r for a small sample of our data. Two-body decays are characterized by a curved band distribution in the θ_{op} - versus - r plot. See Fig. 4.9 for a schematic representation of the θ_{op} -

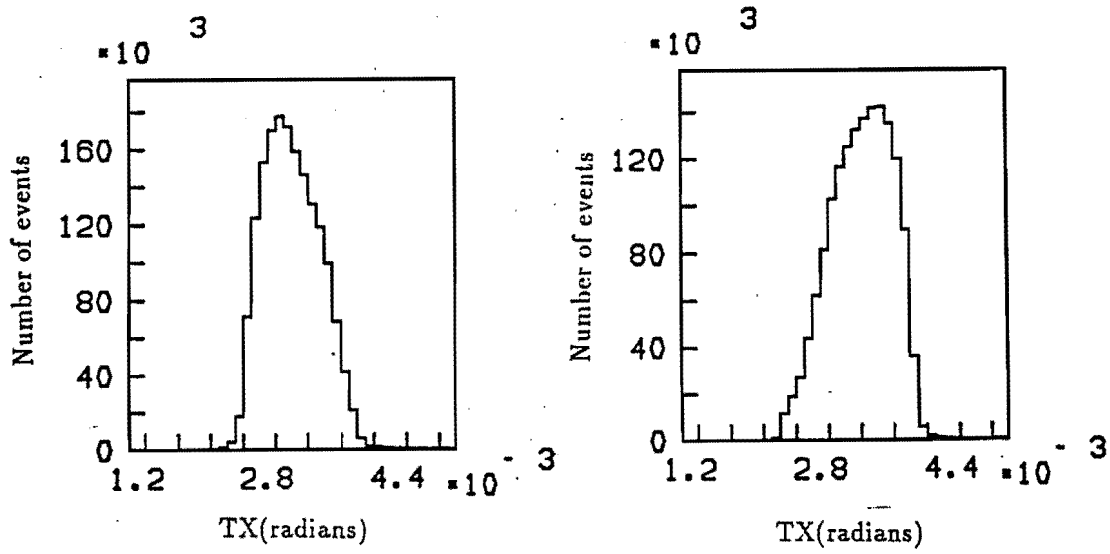

Figure 4.6: Distribution of TX angle (radians) of hyperon for positive(left) and negative(right) targeting angle.

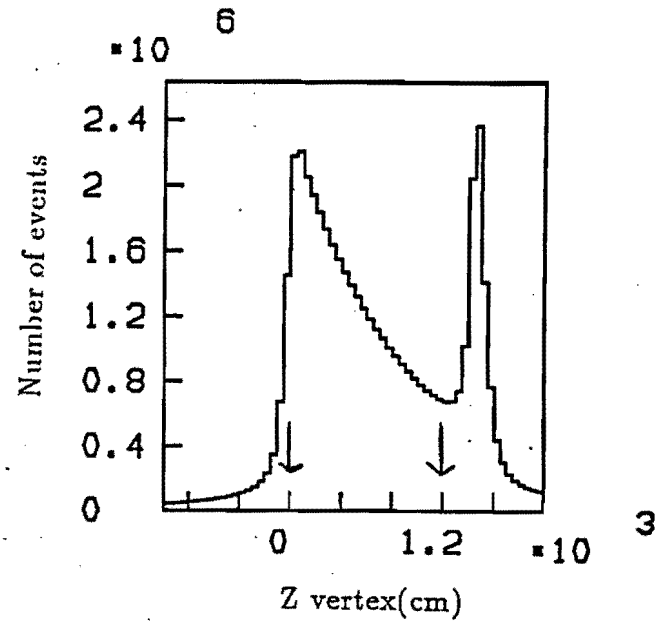

Figure 4.7: z vertex(cm) distribution of hyperon with respect to SD3. SD3 is at the origin on this plot. The peak at 1400 cm (WA) is due to decays downstream of WA for which the offline program assigned the wrong z vertex position. We make the cut shown by the arrows.

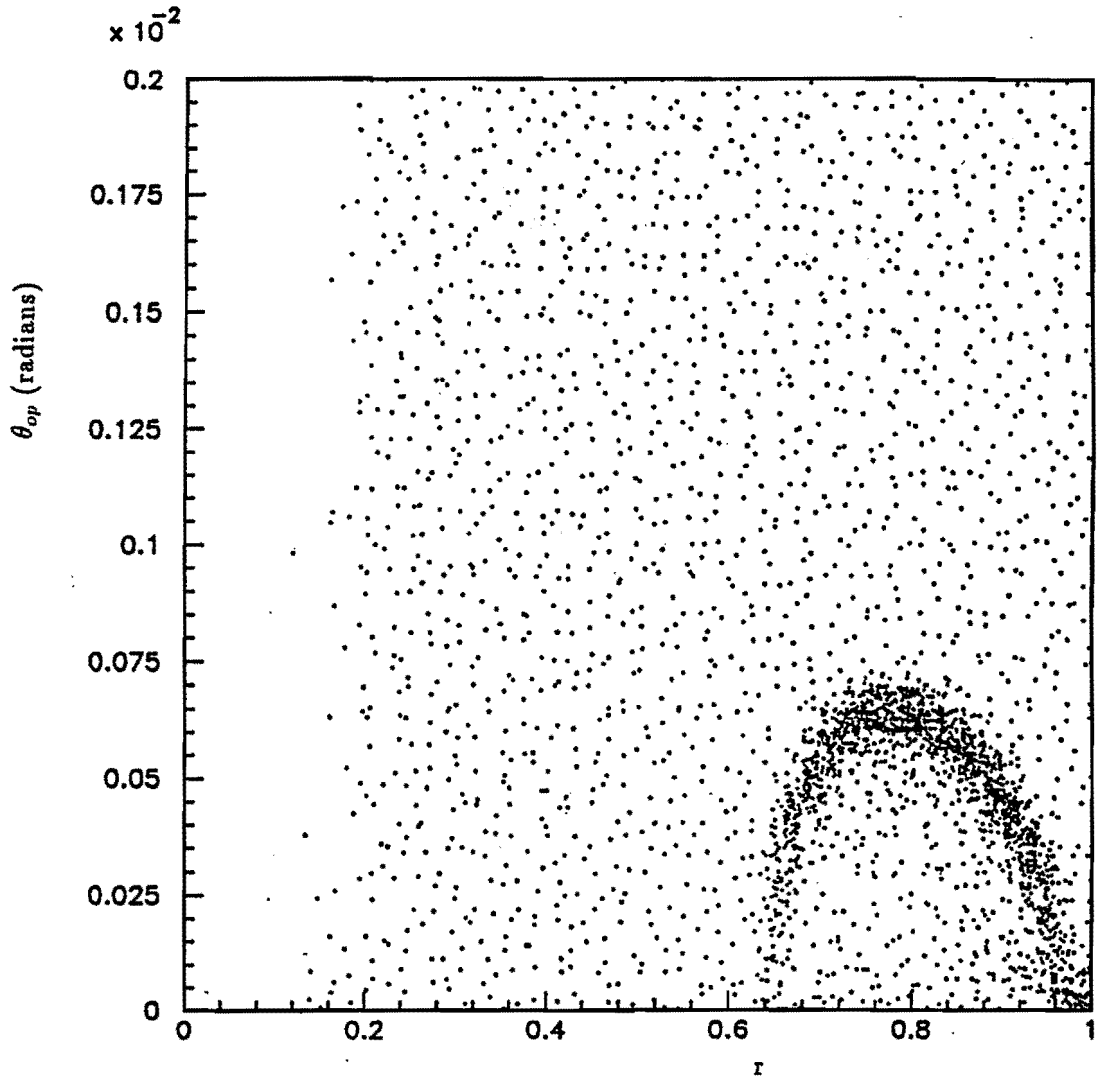

Figure 4.8: θ_{op} (radians) - versus - r for a small sample of our data. The curved band is the decay $\Sigma^+ \rightarrow p\pi^0$.

versus - r plot of the decays that are seen in these data. At the level of statistics shown in Fig. 4.8 we only see decay $\Sigma^+ \rightarrow p\pi^0$. We also see an excess of events near $\theta_{op} = 0$ and r = 1. These events are interactions that produced a low energy neutral particle that satisfied the trigger. Therefore we make the following cuts to remove them. $\theta_{op} \geq 100\mu$rad OR r ≤ 0.97. We also require that r < 1.

From the hyperon track and the baryon track we reconstruct the mass-squared of the missing neutral, m_x^2 assuming the decay hypothesis $\Sigma^+ \rightarrow pX$. Shown in Fig. 4.10 is the missing-mass-squared distribution for our full data sample. We see in this sample the main peak at $m_{\pi^0}^2 = 0.0182$ GeV$^2/c^4$ with 48×10^6 $\Sigma^+ \rightarrow p\pi^0$. There is a shoulder at $m_\gamma^2 = 0$. This shoulder contains 67×10^3 $\Sigma^+ \rightarrow p\gamma$. There is also a shoulder with 250×10^3 $K^+ \rightarrow \pi^+\pi^0$ events. For $\Sigma^+ \rightarrow p\gamma$ this number was determined by fitting the region around 0 to a Gaussian plus a background function. For $K^+ \rightarrow \pi^+\pi^0$ this number was determined by forming the missing-mass-squared assuming $K^+ \rightarrow \pi^+X$ and fitting the region around $m_{\pi^0}^2 = 0.0182$ GeV$^2/c^4$ to a Gaussian plus a background.

4.7 Data Samples

There was a total of 210×10^6 data events analyzed in the pass1 reconstruction. See Fig. 4.1 for a diagram of the analysis scheme. There were 97×10^6 candidate (CAND) events output from pass1. The two most important output data streams were PGAM and PRE. One out of every 50 candidate events went to a separate sample called the PRE sample for PREscaled candidates. There were 1.9×10^6 PRE events separated into 2 samples of positive and negative targeting angle. The PGAM sample was made by accepting only events with a missing-mass-squared around 0 where $\Sigma^+ \rightarrow p\gamma$ would be, $-0.01 < m_x^2 < 0.01$ GeV$^2/c^4$. This sample contained 3.3×10^6 events separated into 2 samples of positive and negative targeting angle.

From these two samples α_γ and Br($\Sigma^+ \rightarrow p\gamma$) were measured. Because α_γ and Br($\Sigma^+ \rightarrow p\gamma$) are two separate measurements which have different requirements the analysis for α_γ and Br($\Sigma^+ \rightarrow p\gamma$) divides into 2 different analyses.

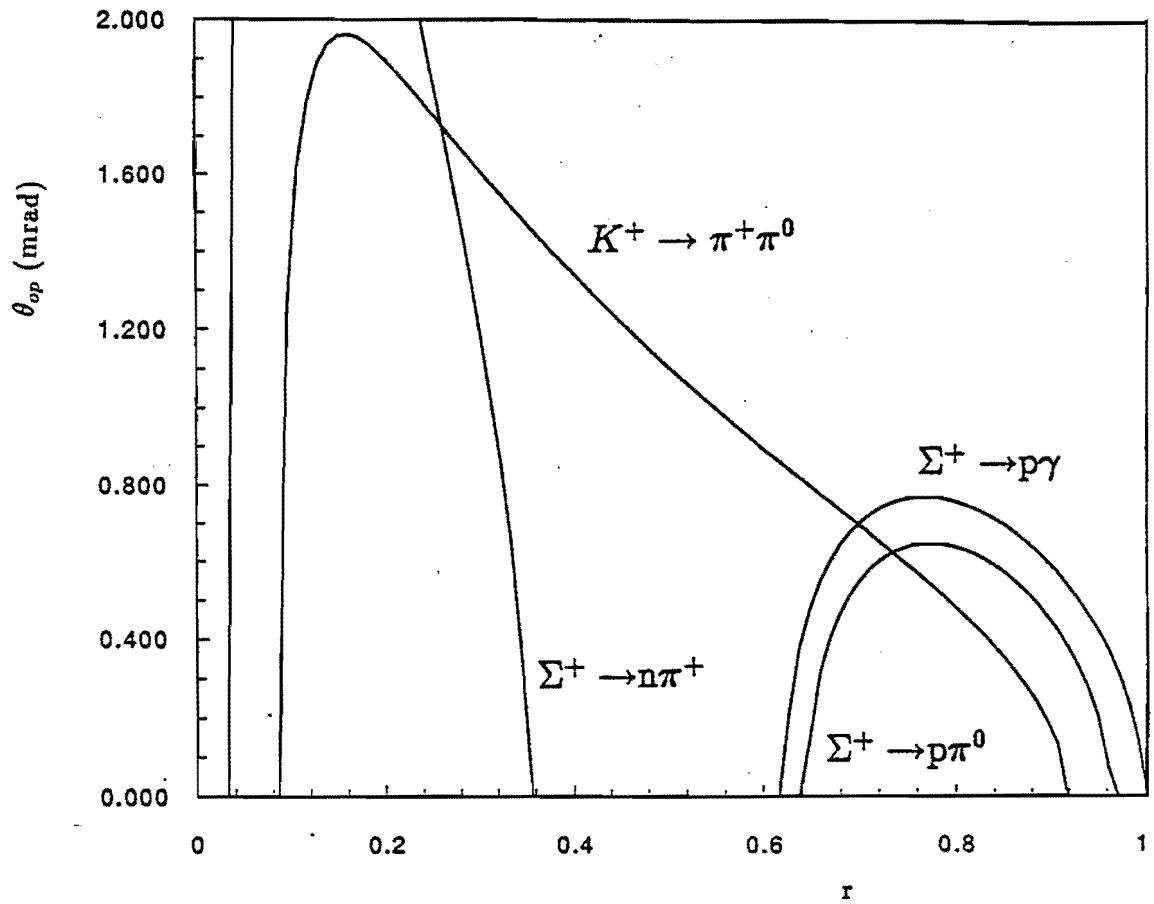

Figure 4.9: Schematic representation of θ_{op} (mrad) - versus - r plot for expected decay modes in E761. This is NOT data.

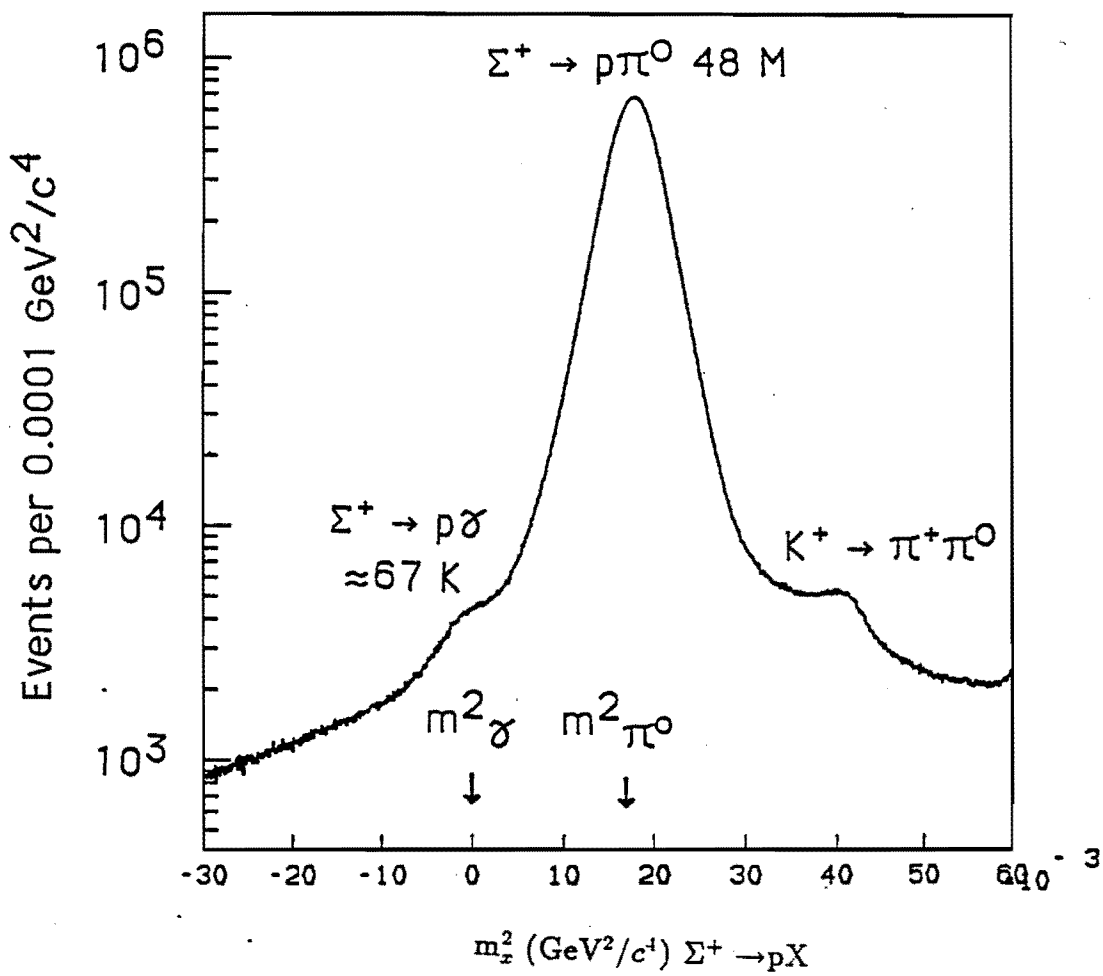

Figure 4.10: Missing-mass-squared (GeV^2/c^4) m_x^2 assuming $\Sigma^+ \rightarrow \mathrm{p}X$ for our full data sample. There are 48×10^6 $\Sigma^+ \rightarrow \mathrm{p}\pi^0$, 67×10^3 $\Sigma^+ \rightarrow \mathrm{p}\gamma$ and 250×10^3 $K^+ \rightarrow \pi^+\pi^0$.

Chapter 5

Asymmetry Parameter $\Sigma^+ \rightarrow p\gamma$

We determined α_γ using the "bias cancelling technique" [62]. The center of mass (CM) angular distributions we measured are the theoretically expected distributions multiplied by our experimental acceptance. We cancelled the acceptance using the bias cancelling technique by comparing two sets of data, spin up and spin down. We measured the polarization of the Σ^+ using the decay $\Sigma^+ \rightarrow p\pi^0$ and its known asymmetry parameter. From this we determined α_γ.

5.1 Bias Cancelling Technique

The Bias Cancelling Technique uses two data samples with the polarization in opposite directions to cancel the acceptance of the apparatus and changes in the beam phase space between the two data samples. The data samples are broken into bins of phase space and the asymmetry is extracted from each of these bins. The asymmetry is determined directly from the data by comparing spin up and spin down data. No Monte Carlo simulation was required or used in this analysis.

The expected CM angular distribution is given by equation 1.1 integrated over the azimuthal angle

$$\frac{1}{N_T}\frac{dN}{d\cos\theta} = \frac{1}{2}[1 + \alpha P_Y \cos\theta] \tag{5.1}$$

where N is the number of events, N_T is the total number of events, α is the asymmetry parameter for the decay under study, P_Y is the polarization of the hyperon, Y, and θ

is the CM angle between the outgoing baryon and the coordinate system directions. We did not measure equation 5.1 but equation 5.1 multiplied by our experimental acceptance, $\epsilon_A(\cos\theta^j$,TX,TY), which is a function of $\cos\theta^j$, TX and TY

$$\frac{1}{N_T}\frac{dN}{d\cos\theta^j} = \frac{\epsilon_A(\cos\theta^j, \mathrm{TX}, \mathrm{TY})}{2}[1 + \alpha P_Y^j \cos\theta^j] \tag{5.2}$$

where j = x, y or z signifies the direction in the Σ^+ center of mass. We collected two sets of data spin up, denoted by a $\Uparrow$, where the angular distribution is given by

$$\frac{1}{N_T \Uparrow}\frac{dN \Uparrow}{d\cos\theta^j} = \frac{\epsilon_A(\cos\theta^j, \mathrm{TX}, \mathrm{TY}) \Uparrow}{2}[1 + \alpha P_Y^j \cos\theta^j] \tag{5.3}$$

and spin down, denoted by $\Downarrow$, where we reversed the targeting angle and thus changed the sign of the polarization.

$$\frac{1}{N_T \Downarrow}\frac{dN \Downarrow}{d\cos\theta^j} = \frac{\epsilon_A(\cos\theta^j, \mathrm{TX}, \mathrm{TY}) \Downarrow}{2}[1 - \alpha P_Y^j \cos\theta^j] \tag{5.4}$$

To extract the asymmetry, A^j, we took the difference of the spin up and spin down data divided by their sum. In the limit that the acceptance for both spin up and spin down are the same.

$$A^j \cos\theta^j \equiv \frac{\frac{1}{N_T\Uparrow}\frac{dN\Uparrow}{d\cos\theta^j} - \frac{1}{N_T\Downarrow}\frac{dN\Downarrow}{d\cos\theta^j}}{\frac{1}{N_T\Uparrow}\frac{dN\Uparrow}{d\cos\theta^j} + \frac{1}{N_T\Downarrow}\frac{dN\Downarrow}{d\cos\theta^j}} = \alpha P_Y^j \cos\theta^j \tag{5.5}$$

We divided the middle expression by $\cos\theta^j$ to determine the asymmetry for each bin in $\cos\theta^j$. We averaged over all the asymmetries from each bin to determine the final asymmetry A^j.

$$A^j = \alpha P_Y^j \tag{5.6}$$

The acceptance of our apparatus was relatively high. Using a Monte Carlo simulation the acceptance as a function of $\cos\theta^y$ is shown in Fig. 5.1 and Fig. 5.2. The average acceptance for $\Sigma^+ \rightarrow p\gamma$ was 64% and 85% for $\Sigma^+ \rightarrow p\pi^0$. The acceptance falls off around $\cos\theta^y \sim 0$ for $\Sigma^+ \rightarrow p\gamma$ because these are events with the photon in the hole in the steel plates. These events can not be extracted using the TRD and are thus removed. The acceptance distribution is found by adding equation 5.3 and equation 5.4 where the polarization cancels and one is left with just the acceptance.

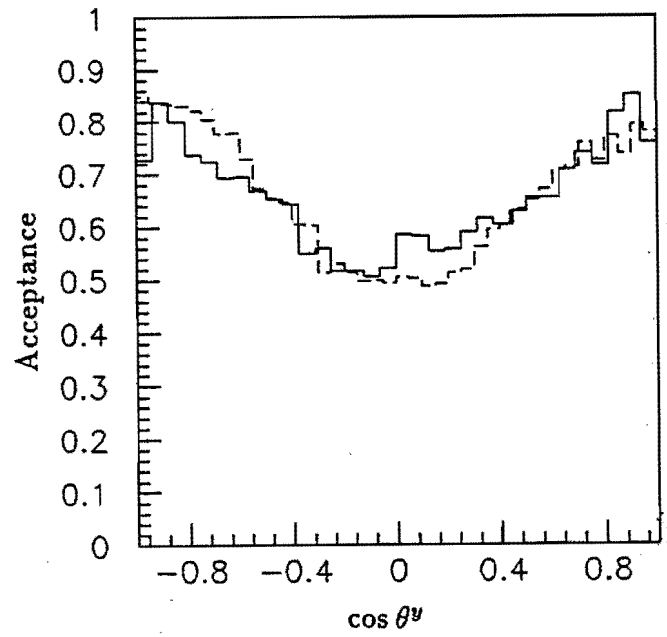

Figure 5.1: Acceptance as a function of $\cos\theta^y$ for $\Sigma^+ \rightarrow p\gamma$. Solid is data and dashed is Monte Carlo. The plots are normalized to equal area. The average acceptance is 64%.

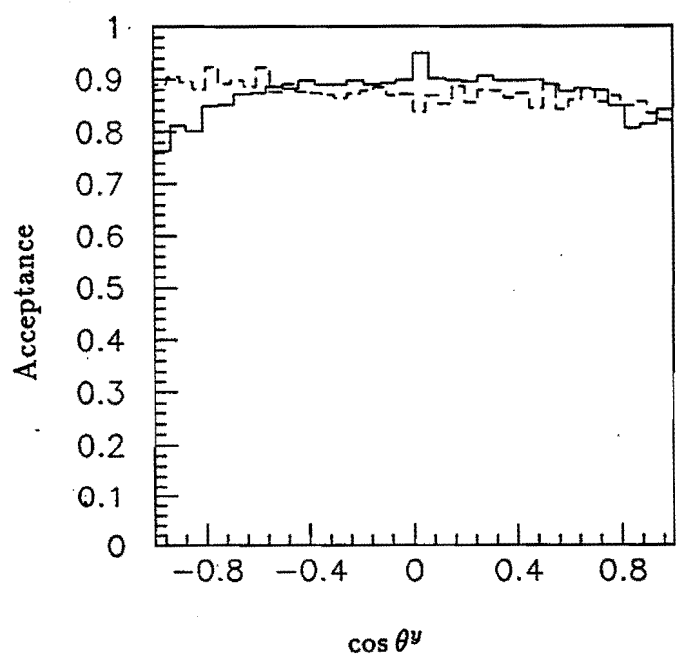

Figure 5.2: Acceptance as a function of $\cos\theta^y$ for $\Sigma^+ \rightarrow p\pi^0$. Solid is data and dashed is Monte Carlo. The plots are normalized to equal area. The average acceptance is 85%.

The polarization of the hyperon beam was along the y direction because we targeted the incoming proton beam horizontally. There was no polarization in the x or z direction. Therefore the asymmetry should be 0 in the x and z direction. When the analysis above was applied to the data sample a large non-zero x asymmetry was discovered. We call this a false asymmetry because the asymmetry should be zero but is not. This x false asymmetry was a result of the difference in TX shown in Fig. 4.6 between positive and negative targeting angle. To cancel this x false asymmetry we broke up the data into bins of TX and TY and analyzed the asymmetry as above for each bin of TX and TY. We then averaged the asymmetry to achieve the final result. We broke the data in bins of TY because other parts of the experiment used vertical targeting and thus had large y false asymmetries. One program was used to handle both horizontal and vertical targeting.

The bias cancelling technique was insensitive to differences in the magnitude of the polarization caused by the difference in targeting angles. We carried out an analysis where we allowed the asymmetry to vary between the 2 targeting angles and found it did not change the answer.

To determine α_γ we performed the bias cancelling technique for the two samples of data we collected $\Sigma^+ \rightarrow p\gamma$ and $\Sigma^+ \rightarrow p\pi^0$, ie

$$A_\gamma^y = \alpha_\gamma P_\Sigma \tag{5.7}$$

for $\Sigma^+ \rightarrow p\gamma$ and

$$A_0^y = \alpha_0 P_\Sigma \tag{5.8}$$

for $\Sigma^+ \rightarrow p\pi^0$ where α_γ is the asymmetry parameter of $\Sigma^+ \rightarrow p\gamma$ which we are measuring, α_0 is the asymmetry parameter [2] of $\Sigma^+ \rightarrow p\pi^0$, α_0 = -0.98, P_Σ is the polarization of the Σ^+, A_γ^y is y asymmetry of $\Sigma^+ \rightarrow p\gamma$ and A_0^y is the y asymmetry of $\Sigma^+ \rightarrow p\pi^0$. Remember the polarization was only along the y direction. We combined these two equations and solved for α_γ.

$$\alpha_\gamma = \frac{A_\gamma^y}{A_0^y}\alpha_0 \tag{5.9}$$

We measured A_γ^y and A_0^y from our data and used the known value of α_0 to determine α_γ.

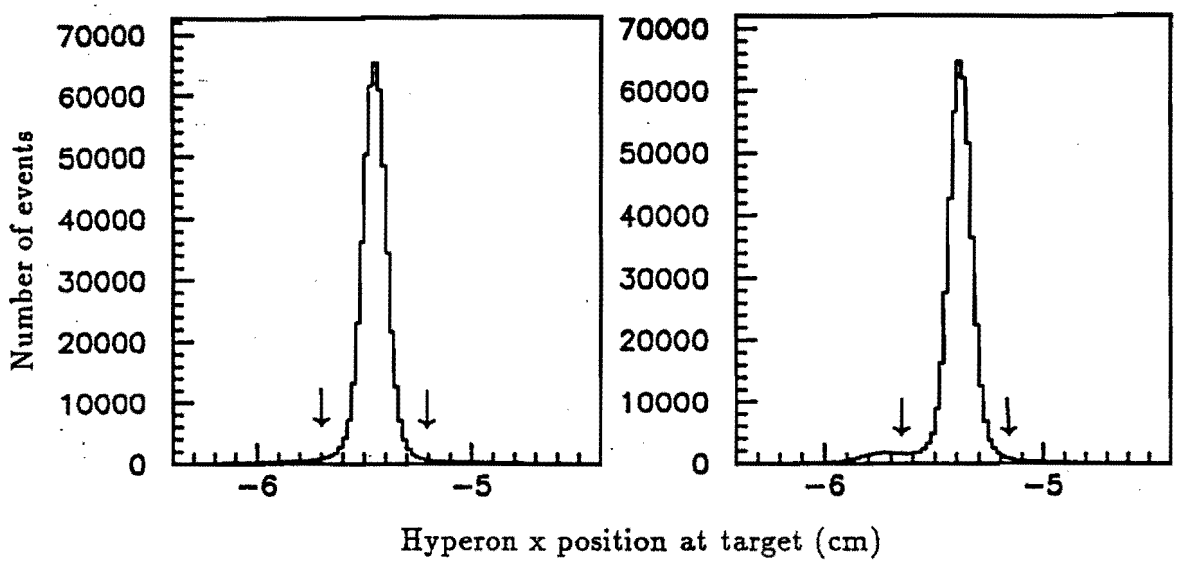

Figure 5.3: x position (cm) of the hyperon track at the target for positive (left) and negative (right) targeting angle for the PRE sample. The cuts shown by the arrows were made.

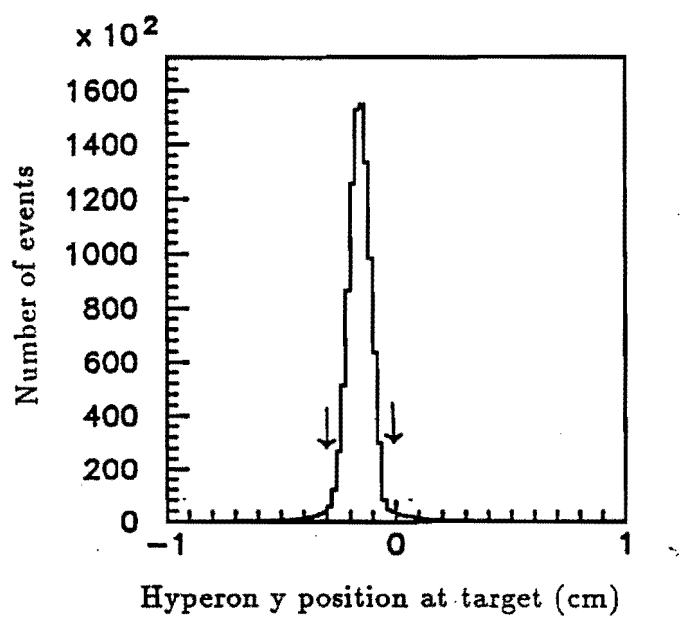

Figure 5.4: y position (cm) of the hyperon track at the target for the PRE sample. The cuts shown by the arrows were made.

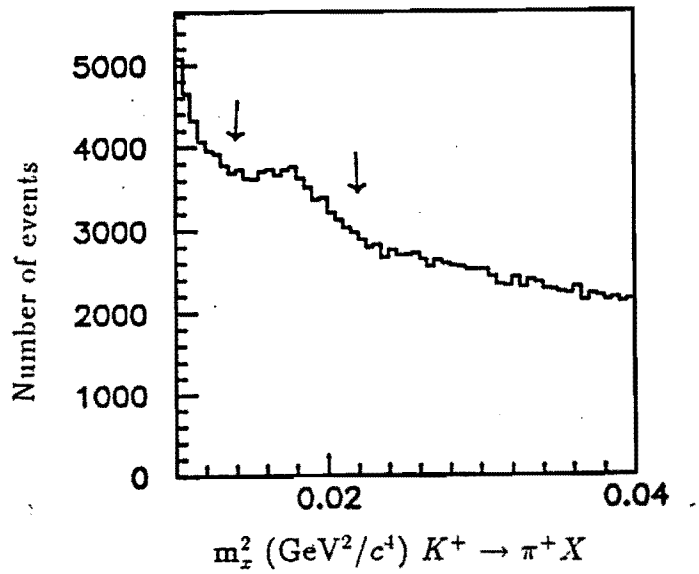

Figure 5.5: Missing-mass-squared (GeV$^2/c^4$) m_x^2 assuming $K^+ \rightarrow \pi^+ X$ for the PRE sample. We removed events between the arrows.

$$|m_x^2 - 0.018\ | > 0.004\ \mathrm{GeV}^2/c^4,\ K^+ \rightarrow \pi^+ X$$

See Fig. 5.5 for a plot of m_x^2 assuming $K^+ \rightarrow \pi^+ X$ from the PRE sample. The cut to remove $K^+ \rightarrow \pi^+\pi^0$ did not affect the asymmetry of $\Sigma^+ \rightarrow p\pi^0$. The K^+ is a spin zero particle and thus unpolarized. There was <0.5% $K^+ \rightarrow \pi^+\pi^0$ within the $\Sigma^+ \rightarrow p\pi^0$ sample. This contributed negligible to the asymmetry of $\Sigma^+ \rightarrow p\pi^0$.

The final cut to isolate a clean sample of $\Sigma^+ \rightarrow p\pi^0$ was to cut on the missing-mass-squared assuming $\Sigma^+ \rightarrow pX$ around $m_{\pi^0}^2$. We made the cut.

$$0.010 < m_x^2 < 0.026\ \mathrm{GeV}^2/c^4,\ \Sigma^+ \rightarrow pX$$

See Fig. 5.6 for the missing-mass-squared distribution for the PRE sample. The asymmetry, $A_0^{x,y,z}$ using the bias cancelling technique with 15 bins in $\cos\theta^{cm}$, 8 bins in TX and 2 bins in TY is given in Table 5.1.

5.3 A_γ^y, Asymmetry of $\Sigma^+ \rightarrow p\gamma$

We used the same cuts on $\Sigma^+ \rightarrow p\gamma$ as $\Sigma^+ \rightarrow p\pi^0$. To determine A_γ we analyzed the PGAM sample with the cuts shown in section 5.2. Here are the cuts restated.

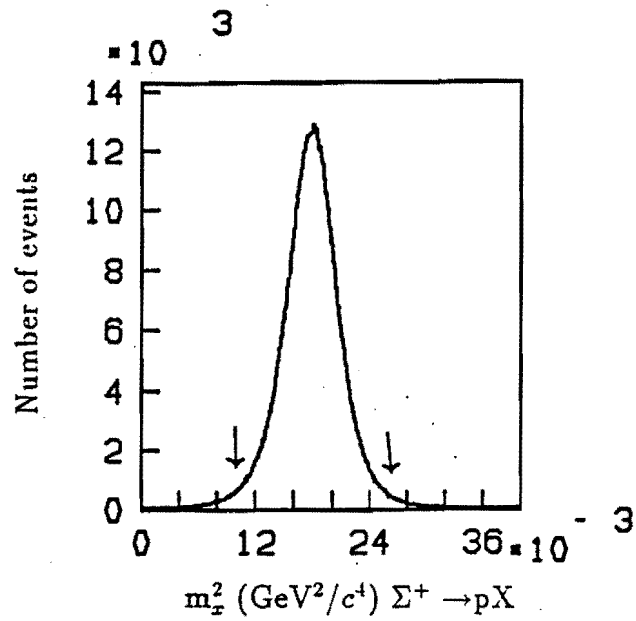

Figure 5.6: Missing-mass-squared (GeV$^2/c^4$) m_x^2 assuming $\Sigma^+ \rightarrow pX$ for the PRE sample. The cut shown by the arrows was made.

X	Y	Z
-0.0050 ± 0.0021	-0.1188 ± 0.0021	-0.0011 ± 0.0021

Table 5.1: Asymmetries of $\Sigma^+ \rightarrow p\pi^0$, A_0.

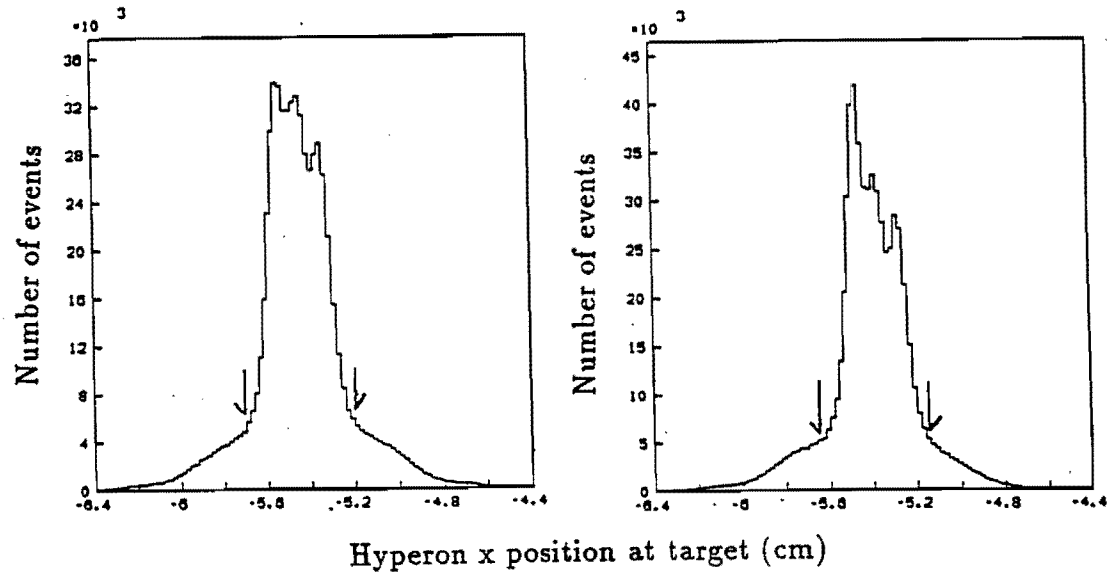

Figure 5.7: x position (cm) of the hyperon track at the target for positive (left) and negative (right) targeting angle for the PGAM sample. The cuts shown by the arrows were made.

$$\chi^2_{hyperon} < 4$$
$$\chi^2_{baryon} < 2$$
$$0 < \text{z vertex} \leq 1200 \text{ cm from SD3}$$
$$325 < \text{hyperon momentum} < 425 \text{ GeV/c}$$
$$\text{r(ratio of baryon momentum over hyperon momentum)} < 1$$
$$\theta_{op} \geq 100\ \mu\text{rad OR r} \leq 0.97$$
$$-5.65 < x_{hyperon} < -5.15 \text{ cm negative targeting angle}$$
$$-5.70 < x_{hyperon} < -5.20 \text{ cm positive targeting angle}$$
$$-0.28 < y_{hyperon} < -0.04 \text{ cm}$$

See Fig. 5.7 and Fig. 5.8 for the x hyperon distribution at the target for positive and negative targeting angle and the y hyperon distribution at the target for the PGAM sample. Compare the distributions in Fig. 5.7 and Fig. 5.3. The x distribution at the target for the PGAM sample is wider than for the PRE sample. The PGAM sample is mostly made up of $\Sigma^+ \rightarrow p\pi^0$ events whose missing-mass-squared has been calculated incorrectly due to an error in hyperon momentum. This error in the hyperon momentum causes an error in the extrapolated position at the target and

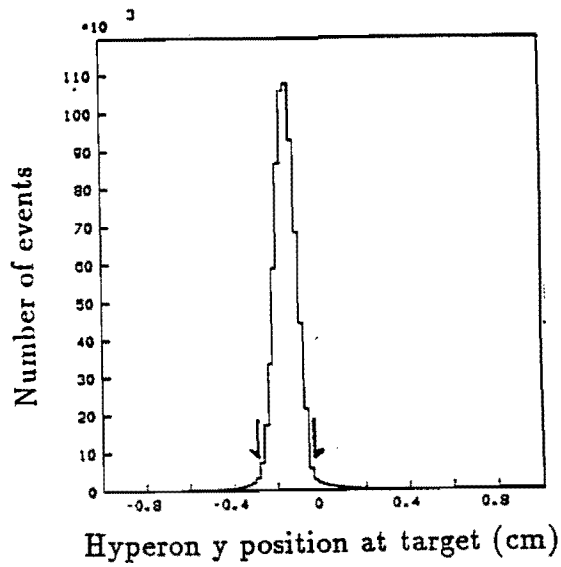

Figure 5.8: y position (cm) of the hyperon track at the target for the PGAM sample. The cuts shown by the arrows were made.

therefore the wider the distribution. This topic is discussed more fully in section 5.4.1.

We also made a cut to remove $K^+ \rightarrow \pi^+\pi^0$. We reconstructed the m_x^2 assuming the decay $K^+ \rightarrow \pi^+X$ and made a cut to remove events around $m_{\pi^0}^2 = 0.0182$ GeV^2/c^4.

$$|m_x^2 - 0.018\ | > 0.004\ \mathrm{GeV}^2/c^4,\ K^+ \rightarrow \pi^+X$$

See Fig. 5.9 for a plot of m_x^2 assuming $K^+ \rightarrow \pi^+X$ from the PGAM sample. The cut to remove $K^+ \rightarrow \pi^+\pi^0$ did affect the asymmetry of $\Sigma^+ \rightarrow p\gamma$. The K^+ is a spin zero particle and thus unpolarized. There was about 5% $K^+ \rightarrow \pi^+\pi^0$ within the $\Sigma^+ \rightarrow p\gamma$ sample. By removing these events with zero polarization the asymmetry of $\Sigma^+ \rightarrow p\gamma$ increased by about 4%. However increasing the size of the cut further did not change α_γ.

From Fig. 4.10 the dominant background to $\Sigma^+ \rightarrow p\gamma$ is $\Sigma^+ \rightarrow p\pi^0$. To separate $\Sigma^+ \rightarrow p\gamma$ from $\Sigma^+ \rightarrow p\pi^0$ we now use the photon spectrometer. To illustrate the procedure used to separate $\Sigma^+ \rightarrow p\gamma$ from $\Sigma^+ \rightarrow p\pi^0$ a single event display of one half (plan view) of the photon spectrometer is shown in Fig. 5.10 and Fig. 5.11 for

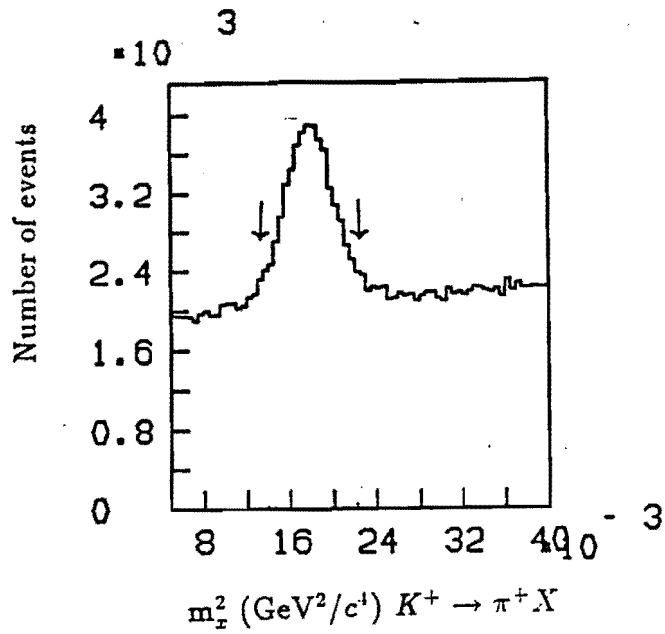

Figure 5.9: Missing-mass-squared (GeV^2/c^4) m_x^2 assuming $K^+ \rightarrow \pi^+ X$ for the PGAM sample. We removed events between the arrows.

a $\Sigma^+ \rightarrow p\gamma$ and $\Sigma^+ \rightarrow p\pi^0$ event respectively. Notice the two large clusters of hits on either side of the π^0 track from the two photons in Fig. 5.11. Remember that the TRD is sensitive to the high energy charged component of the electromagnetic shower. Notice in Fig. 5.10 and Fig. 5.11 that the TRD is insensitive to the proton track but the PWC has hits associated with the track.

The algorithm used to extract $\Sigma^+ \rightarrow p\gamma$ tests the hypothesis that the missing neutral was a single photon from $\Sigma^+ \rightarrow p\gamma$. The following is a summary of the TRD algorithm used to extract $\Sigma^+ \rightarrow p\gamma$ [63].

The data in the TRD was clusterized in space. A cluster is a group of hit wires bounded by 2 blank wires.

The center of the cluster is the weighted average of the hit wires. Remember that each wire in the TRD can have more than 1 pulse on it.

There is a quality factor associated with each cluster. This quality factor is the sum over all the wires in the cluster of the square of the number of pulses on each wire. For example, a cluster consists of 3 wires, first wire has 2 pulses on it, second wire has 3 pulses on it and third wire has 1 pulse on it. The quality factor for this cluster is $2^2 + 3^2 + 1^2 = 14$. An electron with an energy > 2.5 GeV from a shower will

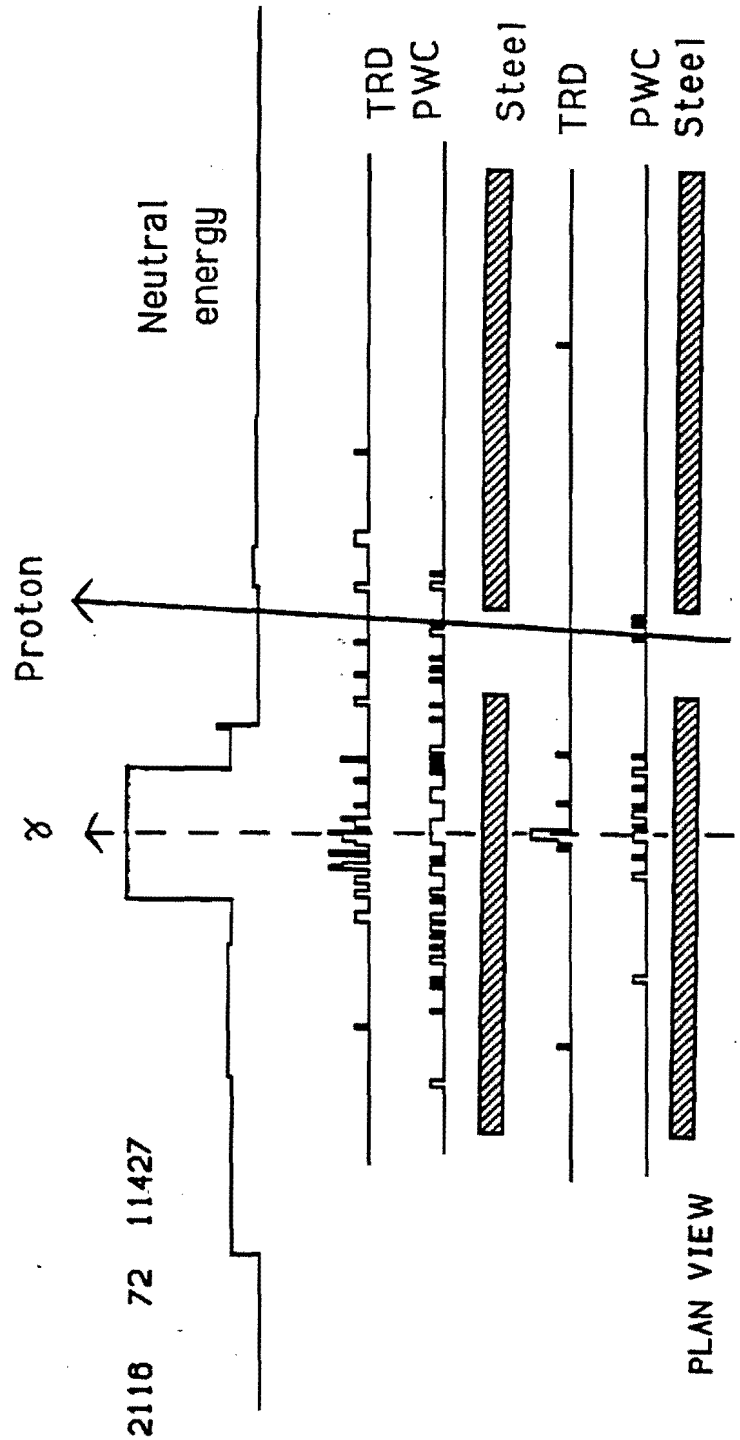

Figure 5.10: Single event display of half of the photon spectrometer for a $\Sigma^+ \rightarrow p\gamma$ event. The missing-mass-squared in the event is 7.43×10^{-4} GeV$^2/c^4$. The TRD χ^2 = 0.15. The solid line is the proton track and the dashed line is the missing neutral or photon in this case.

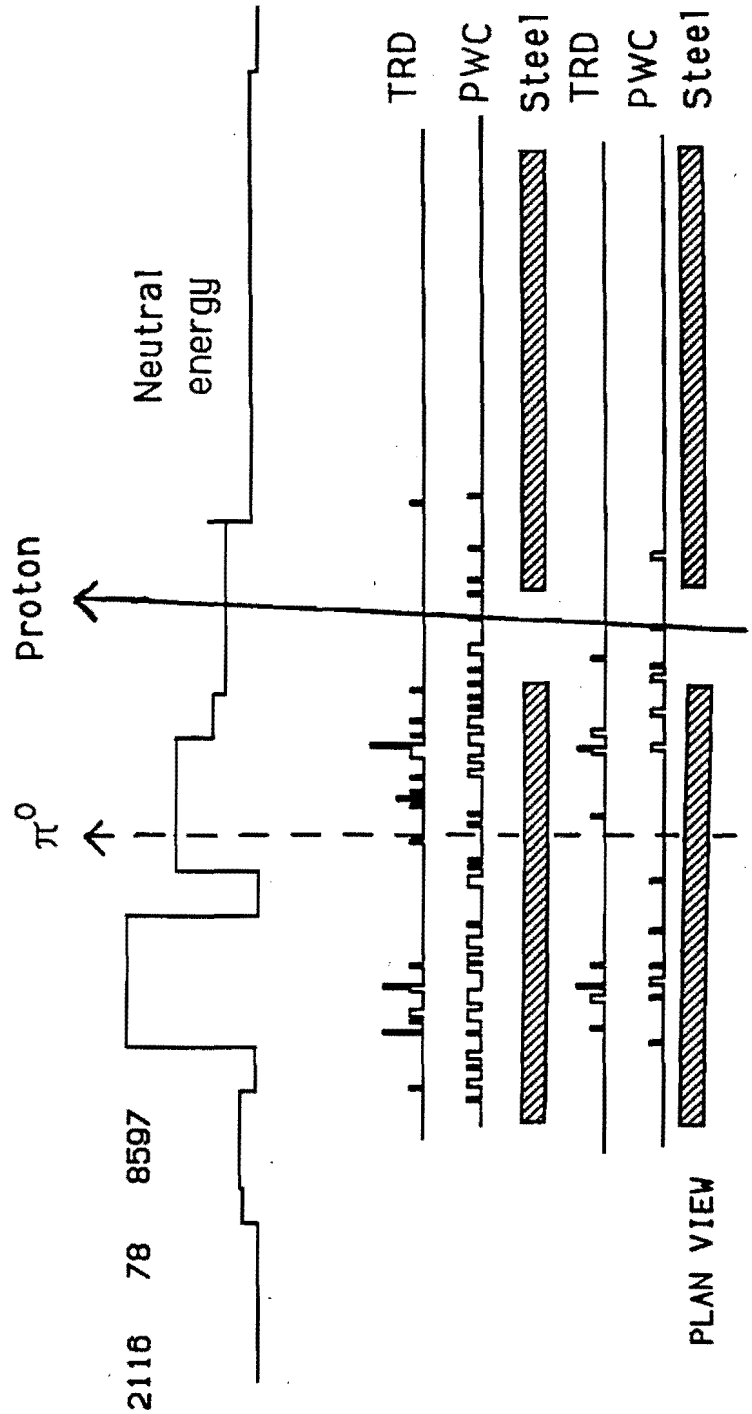

Figure 5.11: Single event display of half of the photon spectrometer for a $\Sigma^+ \rightarrow p\pi^0$ event. The missing-mass-squared in the event is 0.0164 GeV^2/c^4. The TRD $\chi^2 = 50$. The solid line is the proton track and the dashed line is the missing neutral or π^0 in this case.

give an average of 2 pulses on a wire. See Fig. 2.9. Therefore a cluster with a quality factor > 1 is probably an electron (or positron) from an electromagnetic shower.

The PWC before each TRD was essentially 100% efficient for charged particles in an electromagnetic shower. If there were no hits in this PWC associated with the cluster subtract 1 from the quality factor. This is used to remove noise hits in the TRD.

Within each event was a latch bit that signified whether the trigger was from a shower that initiated in the first steel plate or the second. For events that triggered in the second steel plate, only make clusters in the second set of TRD chambers. For events that triggered in the first steel plate make clusters in the first set of TRD chambers. For these events add to the quality factor of the cluster in the first set of TRD chambers 1/3 of the quality factor of the associated cluster in the second set of TRD chambers. The cluster in the second set of TRD chambers should have a quality factor greater than 1.

If there are 2 large clusters close together (< 1.6 cm), make this 1 cluster. The minimum opening angle of $\gamma\gamma$ from the highest energy $\pi^0 \rightarrow \gamma\gamma$ is 2 mrad. This corresponded to 4 cm at the first TRD. Therefore 2 large clusters close together was probably $\gamma \rightarrow e^+e^-$.

We formed a reduced TRD χ^2 by summing the square of the distances between the extrapolated neutral track to the largest cluster with a quality factor greater than 3. If there was no cluster with a quality factor greater than 3 then we used the nearest cluster. We only calculated the TRD χ^2 to the first TRD X and Y for events that began to shower in the first steel plate and to the second TRD X and Y for events that began to shower in the second steel plate. The error we assigned to calculate the reduced TRD χ^2 is the extrapolation error of the missing neutral ($\sim$3 mm) and an estimate of the resolution of the position of the photon as measured by the TRD and the algorithm used (7.7 mm.) The TRD χ^2 has typically 2 degrees-of-freedom. We set an upper limit of 50 on the TRD χ^2. If there are 2 large clusters that are far apart we set the TRD $\chi^2 = 50$. This type of event is probably $\Sigma^+ \rightarrow p\pi^0$, $\pi^0 \rightarrow \gamma\gamma$. The TRD χ^2 of rearphoton events was set to 50. We also required at least 70% of the energy deposited in the photon calorimeter be within 5 cm of the extrapolated neutral

Region	Neutral mass squared GeV^2/c^4	TRD χ^2
S	$-0.0040 \leq m_x^2 \leq 0.0040$	TRD $\chi^2 \leq 1$
B	$-0.0040 \leq m_x^2 \leq 0.0040$	TRD $\chi^2 \geq 4$
T	$+0.0072 \leq m_x^2 \leq 0.0100$	TRD $\chi^2 \leq 1$
N	$+0.0072 \leq m_x^2 \leq 0.0100$	TRD $\chi^2 \geq 4$

Table 5.2: Definition of the 4 regions S, B, N and T.

track (local energy cut.) This local energy cut was insensitive to the poor quality of the photon calorimeter resolution because it was a ratio of the energy measured in the calorimeter within 5 cm, over the the total energy measured by the calorimeter. $\Sigma^+ \rightarrow p\gamma$ should have low TRD χ^2 and $\Sigma^+ \rightarrow p\pi^0$ should have higher TRD χ^2 than $\Sigma^+ \rightarrow p\gamma$ because of the finite opening angle of two photons from the π^0 decay. The $\Sigma^+ \rightarrow p\gamma$ event shown in Fig. 5.10 has a TRD $\chi^2 = 0.15$. This event has a small TRD χ^2 because of the large cluster directly on the extrapolated neutral track. The $\Sigma^+ \rightarrow p\pi^0$ event shown in Fig. 5.11 has a TRD $\chi^2 = 50$ because of the 2 large well separated clusters in the TRD.

The distribution of TRD χ^2 versus missing-mass-squared for the PGAM sample is shown in Fig. 5.12. Fig. 5.13 shows the missing-mass-squared distribution for events with TRD $\chi^2 \leq 1$ and events with TRD $\chi^2 \geq 4$. The events with TRD $\chi^2 \geq 4$ model well the background under the signal peak. We define 4 regions in Fig. 5.12, S for Signal, B for Background, N and T are normalization regions. These regions are defined in Table 5.2 We normalized S and B to equal area in the normalization region $0.0072 \leq m_x^2 \leq 0.0100$ GeV^2/c^4 where the events in this region are dominated by $\Sigma^+ \rightarrow p\pi^0$. We defined a signal fraction, f, which is the number of $\Sigma^+ \rightarrow p\gamma$ events in the S region divided by the total number of events in the S region. This signal fraction, f, is given by

$$f = \frac{N_S - N_B \frac{N_T}{N_N}}{N_S} \tag{5.10}$$

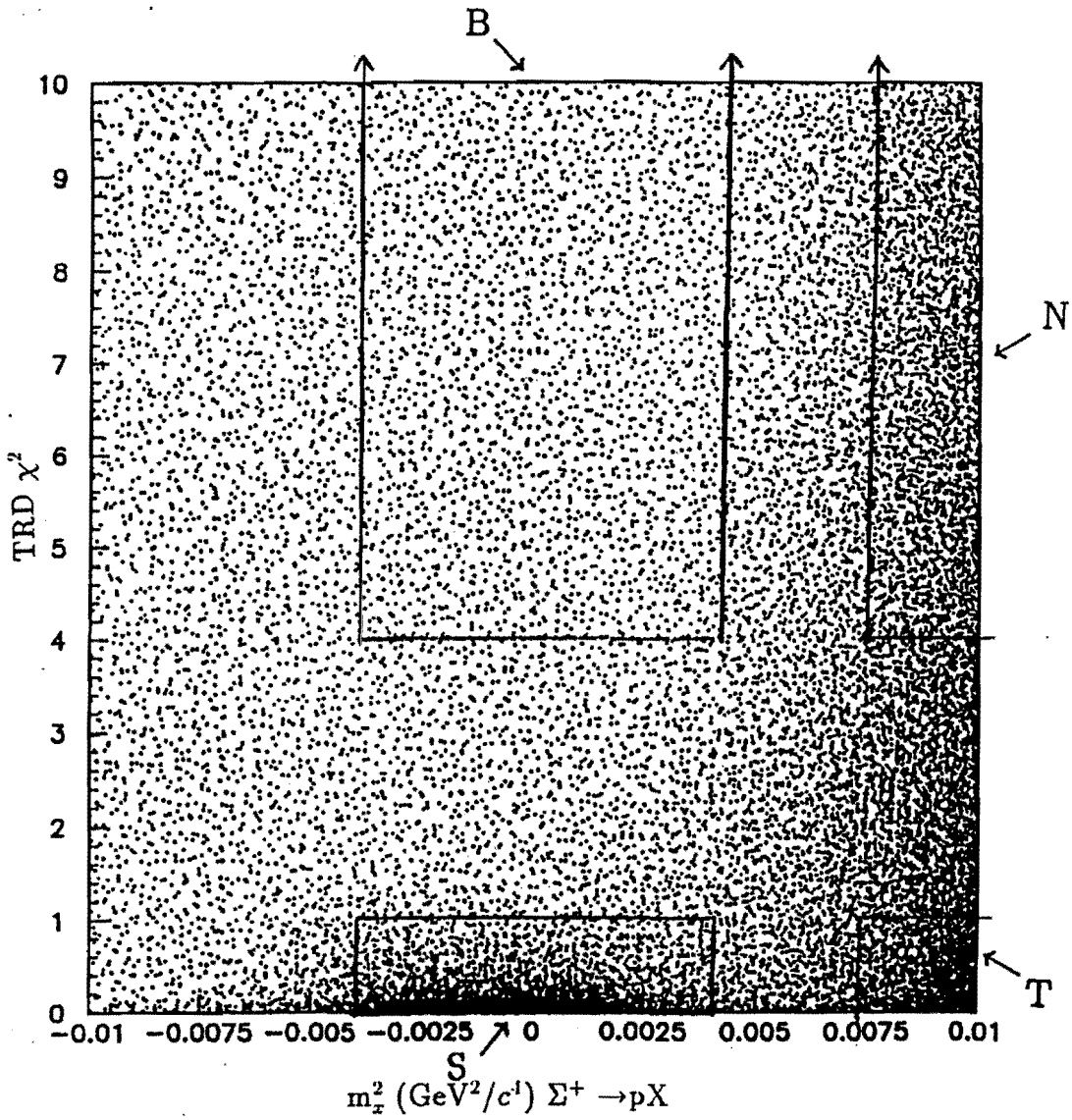

Figure 5.12: TRD χ^2 versus missing-mass-squared m_x^2 (GeV^2/c^4) assuming $\Sigma^+ \rightarrow pX$. There is a clear excess of events at $m_\gamma^2 = 0$. These are $\Sigma^+ \rightarrow p\gamma$. The 4 regions defined are used to extract the A_γ.

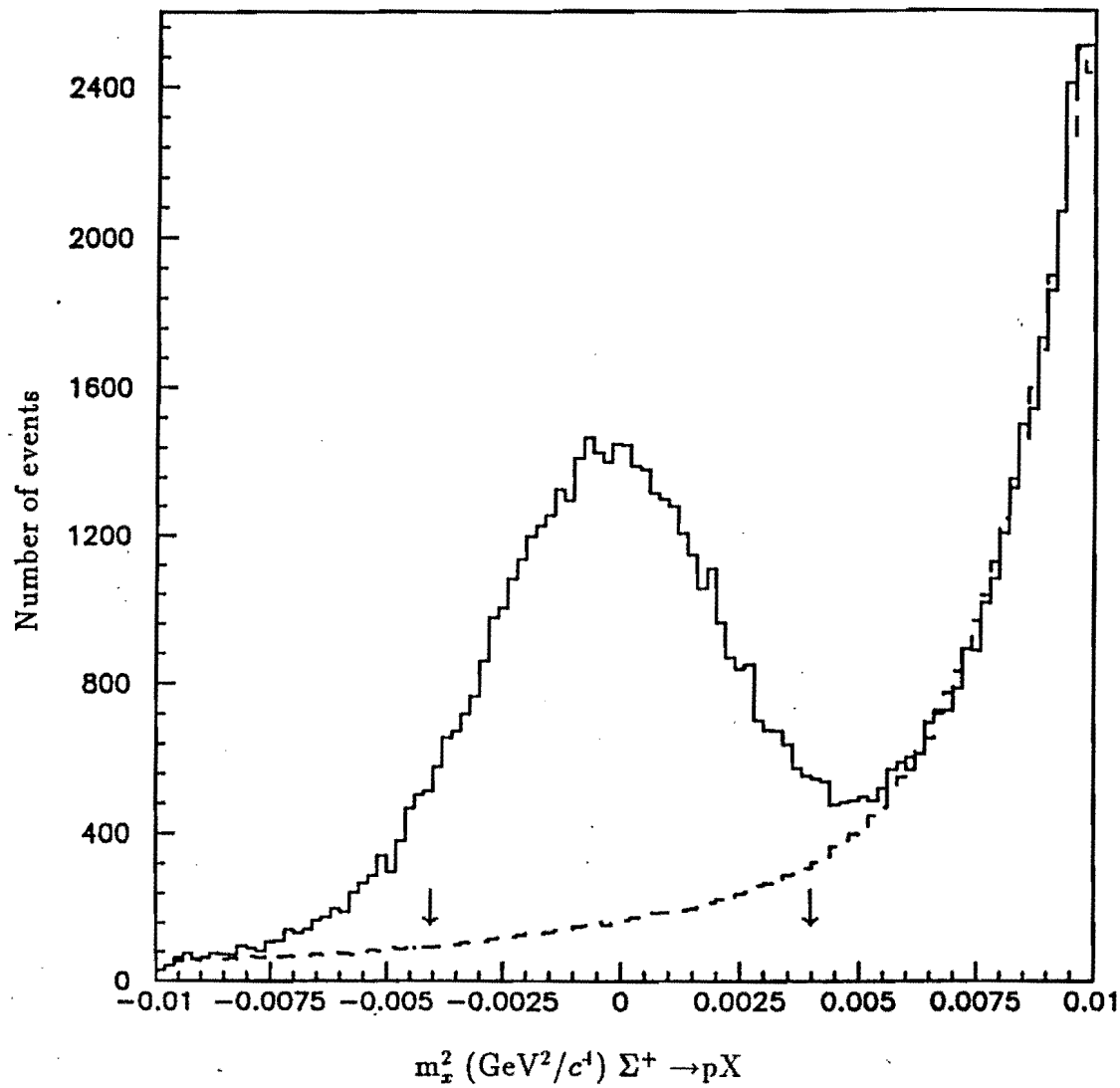

Figure 5.13: M_x^2 (GeV^2/c^4) assuming $\Sigma^+ \rightarrow pX$ for events with TRD $\chi^2 \leq 1$ (solid) and background TRD $\chi^2 \geq 4$. These 2 distributions are normalized to equal area in the region $0.0072 \leq m_x^2 \leq 0.0100$ GeV^2/c^4.

Sample	A^x	A^y	A^z
Signal S	0.0088 ± 0.0082	-0.0884 ± 0.0083	-0.0004 ± 0.0108
Background B	0.0121 ± 0.0073	-0.0938 ± 0.0081	-0.0373 ± 0.0064
$\Sigma^+ \rightarrow p\gamma$	0.0082 ± 0.0100	-0.0873 ± 0.0102	0.0070 ± 0.0130
$\Sigma^+ \rightarrow p\pi^0$	-0.0050 ± 0.0021	-0.1188 ± 0.0021	-0.0011 ± 0.0021

Table 5.3: Asymmetry components for each sample. The Σ^+ polarization is in the y direction so that A^x and A^z are false asymmetries which should be 0.

$$f = 1 - \frac{N_B N_T}{N_S N_N} \tag{5.11}$$

where N_S, N_B, N_T and N_N, are the number of events in each of the corresponding regions. We found in the S region $f = 0.8315 \pm 0.0016$ or a signal to noise ratio of 4.9 to 1. The number of $\Sigma^+ \rightarrow p\gamma$ events in the S region was $fN_S = 34754 \pm 212$. The sample defined by these cuts has a relatively small contribution from background. The asymmetry of this background is measured by analyzing events in the corresponding background region.

We started out in Fig. 4.10 with 67,000 $\Sigma^+ \rightarrow p\gamma$. Applying the TRD algorithm to extract $\Sigma^+ \rightarrow p\gamma$ reduces the sample to 43,000 or 64% efficiency. Requiring the hyperon come from the production target and removing $K^+ \rightarrow \pi^+\pi^0$ reduced this to 39,000 $\Sigma^+ \rightarrow p\gamma$. We then apply a missing-mass-squared cut of ± 0.004 GeV^2/c^4 to isolate a clean sample of 35,000 $\Sigma^+ \rightarrow p\gamma$.

To determine the asymmetries, A_γ, of $\Sigma^+ \rightarrow p\gamma$ we applied the bias cancelling technique in the S and B regions. We used the TRD χ^2 to statistically separate the signal from the background. We used the same number of bins as for A_0, 15 bins in $\cos\theta^{cm}$, 8 bins in TX and 2 bins in TY. The asymmetries are shown in Table 5.3 All of the x and z components are consistent with 0 except the z asymmetry of the background sample. It is not surprising that there is a residual bias in z in the background sample. Its correlation with A_γ^y (and thus α_γ) is small and is included in the systematic error estimate. The angular distribution in the signal region S is

made up of a linear combination of $\Sigma^+ \rightarrow p\gamma$ and background.

$$\frac{2dN}{N_T d\cos\theta^{x,y,z}} \equiv [1+A_S^{x,y,z}\cos\theta^{x,y,z}] = f[1+A_\gamma^{x,y,z}\cos\theta^{x,y,z}]+(1-f)[1+A_B^{x,y,z}\cos\theta^{x,y,z}] \tag{5.12}$$

where $A_S^{x,y,z}$ are the x, y, z asymmetries in the Signal region, $A_\gamma^{x,y,z}$ are the x, y, z asymmetries we are determining and $A_B^{x,y,z}$ are the x, y, z asymmetries in the Background region. This can be simplified.

$$A_S^{x,y,z} = fA_\gamma^{x,y,z} + (1-f)A_B^{x,y,z} \tag{5.13}$$

Solving for $A_\gamma^{x,y,z}$ yields.

$$A_\gamma^{x,y,z} = \frac{A_S^{x,y,z} - (1-f)A_B^{x,y,z}}{f} \tag{5.14}$$

The values of $A_\gamma^{x,y,z}$ are given in Table 5.3. Using the value of A_γ^y determined and A_0^y from the previous section we use equation 5.9 and find α_γ = -0.720 $\pm$ 0.086 (statistical).

5.4 Systematic Error

The systematic error in α_γ was estimated from 4 sources, the z false asymmetry in the Background sample, the difference in the TRD algorithm used to extract $\Sigma^+ \rightarrow p\gamma$, different binning used in the bias cancelling technique and variation of the answer with the cuts used. The experiment was designed to control systematic errors. We found that the result was stable to variation of any of the parameters used in the analysis.

5.4.1 A_B^z, z false asymmetry in background

From Table 5.3 A_B^z is -0.0373 $\pm$ 0.0064. Clearly this is non zero. Does this false asymmetry in the background sample affect α_γ? The answer is no. Its correlation with A_B^y (or A_S^y) is small. Even if there was a correlation the effect of the background correction on the $\Sigma^+ \rightarrow p\gamma$ asymmetry is small because f is large (signal to noise ratio

is high) and because $A_S^y \simeq A_B^y$. Notice that the z asymmetry of $\Sigma^+ \rightarrow p\gamma$ in Table 5.3 is still 0 even though there is the large z false asymmetry in the background.

The background sample is dominated by $\Sigma^+ \rightarrow p\pi^0$ events where we have incorrectly measured the missing-mass-squared. We believe this mistake in the missing-mass-squared is caused by an error in the measurement of the Σ^+ momentum. The hyperon spectrometer contains nine planes of silicon strip detector from which 5 parameter are determined for the hyperon track. This does not leave many planes for redundancy in the measurement of the Σ^+ track. Therefore if a plane has noise hits or a plane has no hits the Σ^+ track could be mismeasured. This z false asymmetry only affects the background sample. There is no false asymmetry for $\Sigma^+ \rightarrow p\pi^0$ or $\Sigma^+ \rightarrow p\gamma$. The center of mass angle $\cos\theta^z$ depends directly on the momentum of the Σ^+ while $\cos\theta^x$ and $\cos\theta^y$ depend on the angles TX and TY respectively.

We attempted and failed to simulate this phenomenon by taking real $\Sigma^+ \rightarrow p\pi^0$ events and changing the Σ^+ momentum and changing the hits on SD2X plane in the silicon strip detectors. We took these "broken" events that now had a missing-mass-squared near 0 and analyzed them for the asymmetry. We could not get $\cos\theta^z$ distributions that we could measure an asymmetry from.

To estimate the systematic error due to A_B^z we plot α_γ versus A_B^z for a representative sample of studies in Fig. 5.14 The different studies correspond to different cuts and algorithms used to analyze the data. The typical error bars on the plot on α_γ are $\pm$ 0.09 and $\pm$ 0.007 for A_B^z. The 3 studies for which A_B^z changed dramatically were, no bias cancelling in x to remove the x false asymmetry, a tighter momentum cut on the Σ^+, 355 $<$ momentum of the Σ^+ $<$ 405 GeV/c, and using 2 momentum bins to calculate α_γ in each bin and then averaging (an attempt to perform bias cancelling in momentum.) Note that 2 of these studies involved the hyperon momentum. The systematic error from A_B^z was estimated by taking the largest deviation (dashed line) from our measured value of α_γ (solid line) for the cases when A_B^z changed significantly. The systematic error from A_B^z is $\pm$ 0.020.

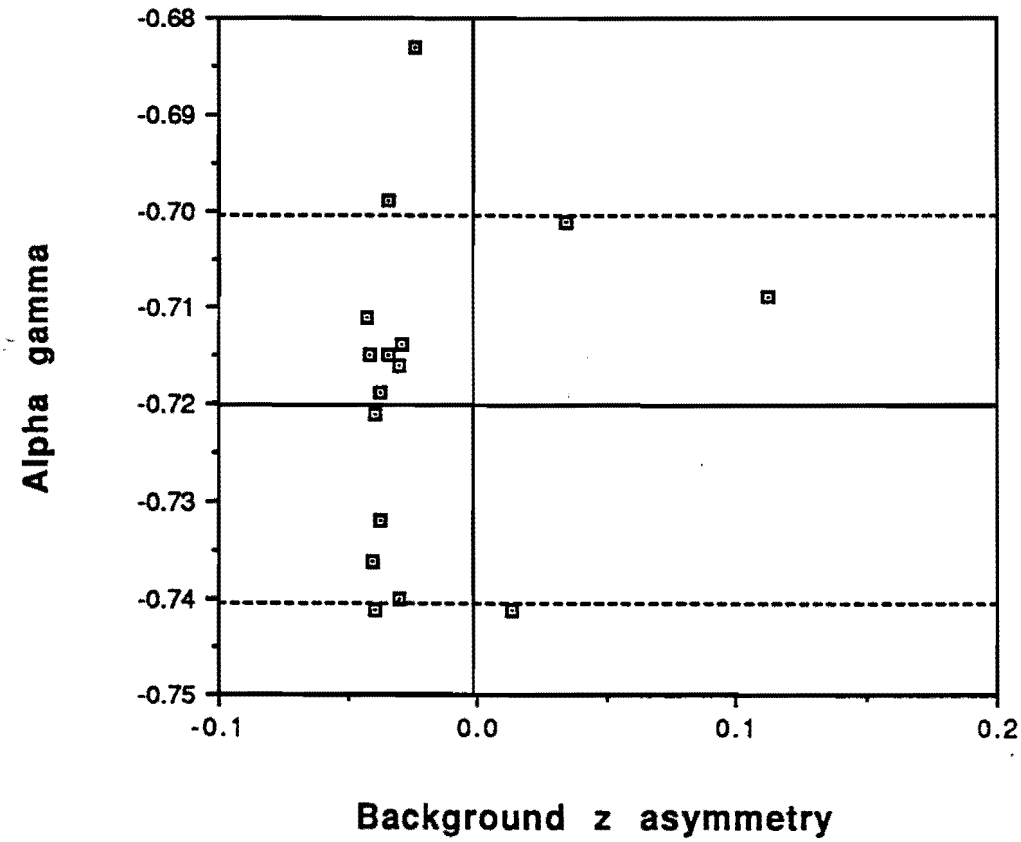

Figure 5.14: α_γ versus A_B^z. The typical error bars on each point are $\pm$ 0.09 for α_γ and $\pm$ 0.007 for A_B^z. The dashed line is the estimated systematic error from A_B^z. The solid line is our measured value of α_γ.

α_γ	TRD algorithm
-0.721 $\pm$ 0.084	Final TRD routine, incorrect x target extrapolation
-0.714 $\pm$ 0.088	Moriond TRD routine, nearest wire on
-0.740 $\pm$ 0.097	Calculate TRD χ^2 only with small pointing error
-0.699 $\pm$ 0.103	PSC TRD routine, large clusters in X and Y

Table 5.4: α_γ for different TRD algorithms.

5.4.2 TRD algorithm

To estimate the systematic error due to the TRD algorithm we reanalyzed the data with the same cuts but with a different TRD algorithm to extract the signal. We analyzed the data using the TRD algorithm described in section 5.3 with an incorrect set of parameters for the x extrapolation of the hyperon back to the target. We found for the final TRD algorithm with the wrong extrapolation back to the target α_γ = -0.721 $\pm$ 0.084. See Table 5.4 for a list of the TRD algorithms and their results. We used the incorrect parameters because the problem was discovered after the study was complete. There is no significant change in the answer with the correct parameters.

The second TRD routine we call the Moriond routine. This was the first TRD routine and was very simple. We calculated a TRD χ^2 by summing over all 8 planes in the photon spectrometer, the square of the distance between the extrapolated neutral and the nearest hit wire in each plane. We used for the error to normalize the TRD χ^2 the wire spacing divided by $\sqrt{12}$, or 577 μm. The value of α_γ from this algorithm is -0.714 $\pm$ 0.088

The third TRD algorithm calculated a TRD χ^2 for the event by taking the square of the distance between the extrapolated neutral and the nearest hit wire in each plane only if the error in the extrapolated neutral position on the TRD is less than 3 mm. That is, we use only events where we can predict well where the missing neutral went. For events that started to shower in the first steel plate sum the TRD χ^2 over the 8 planes downstream of the first steel plate. For events that started to shower in

the second steel plate sum the TRD χ^2 over the 4 planes downstream of the second steel plate. We use the neutral extrapolation error to normalize the TRD χ^2. This TRD algorithm yielded a value of α_γ = -0.740 $\pm$ 0.097.

The last TRD algorithm tested was the PSC algorithm. This algorithm clusterized the information in the TRD in a different way than the final TRD algorithm used to find α_γ. This algorithm required 1 large cluster in both the x and y TRD following the steel plate from which the shower started. A TRD χ^2 was calculated as the square of the distance from the extrapolated neutral track to each of these clusters. The error in the extrapolated neutral was used to normalize the TRD χ^2. This algorithm gave a value of α_γ = -0.699 $\pm$ 0.103. We estimated the systematic error due to the TRD algorithm as the difference between the final answer and the answer determined from the algorithm with the largest deviation from the final answer. Therefore the systematic error due to the TRD algorithm is $\pm$ 0.022.

5.4.3 Bias cancelling binning

To determine α_γ from the bias cancelling technique we binned the data in 15 $\cos\theta^{cm}$ bins , 8 TX bins and 2 TY bins. How does the answer vary when we use different binning? Shown in Fig. 5.15 is the number of cases for various α_γ for different number of bins used in the bias cancelling. We used all combination of 10, 15 and 30 bins in $\cos\theta^{cm}$; 8 and 16 bins in TX; and 1, 2, 4, 8, and 16 bins in TY for a total of 30 studies. The σ of the distribution is 0.025. Therefore the systematic error associated with the different binning is $\pm$ 0.025.

5.4.4 Variation of the cuts

The systematic error due to the variation of the cuts used was estimated by breaking up the data into 8 bins of approximately equal statistics in some cut parameter and determine α_γ for each of the 8 bins. For example, shown in Fig. 5.16 is the x position of the proton at the first steel plate in the photon spectrometer for the PGAM sample. This distribution has been divided into 8 equal bins shown. The asymmetry parameter for each of these bins has been calculated. This is shown in Fig. 5.17. The

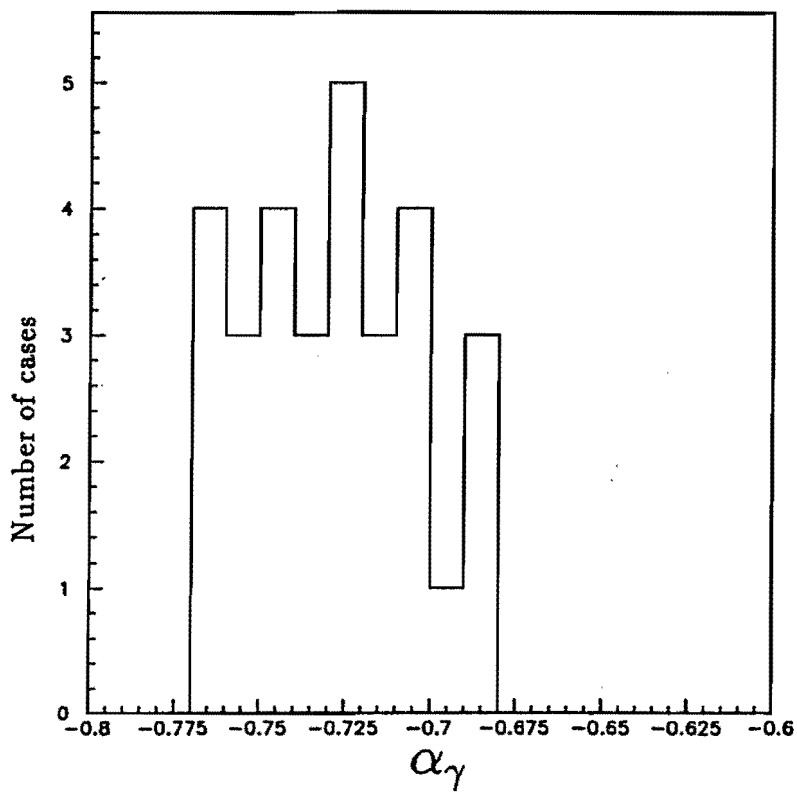

Figure 5.15: Number of cases versus α_γ for different number of bins used in the bias cancelling technique. The σ of the distribution is 0.025.

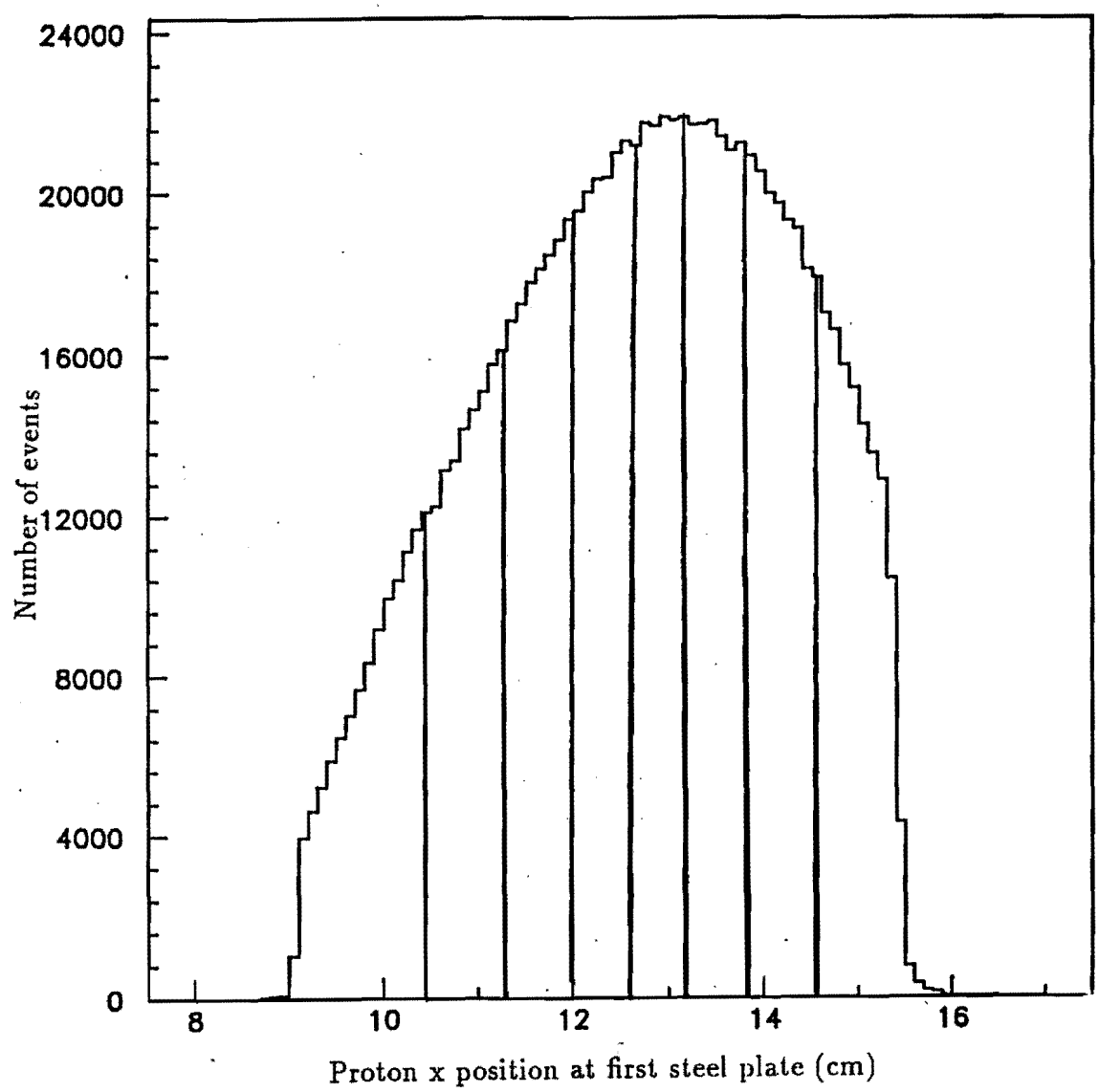

Figure 5.16: X position of the proton (cm) at the first steel plate in the photon spectrometer for the PGAM sample. This distribution has been divided into 8 bins shown by the lines.

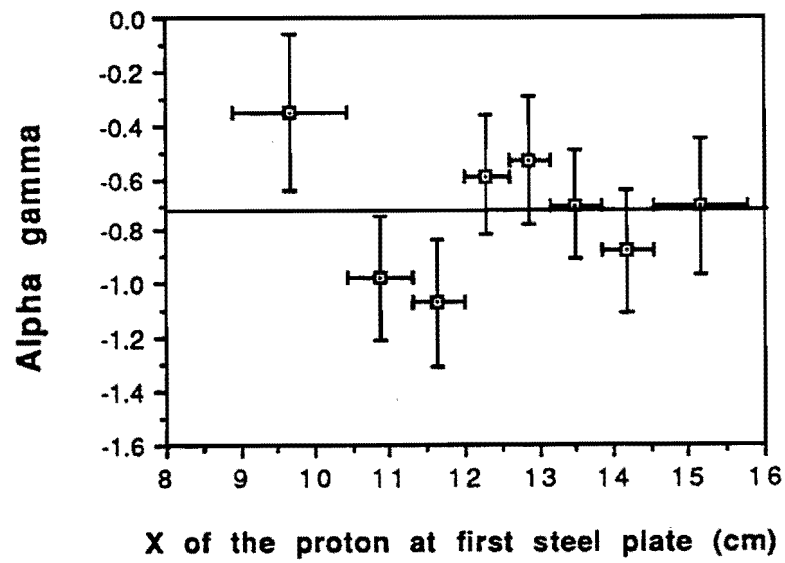

Figure 5.17: α_γ versus x position of the proton at the first steel plate. The weighted mean is the solid line. The χ^2 for the fit to a constant is 6.44 for $\nu = 7$ degrees-of-freedom.

asymmetry parameter is not a function of the x position of the proton at the first steel plate. The χ^2 for the fit to a constant is 6.44 for $\nu = 7$ degrees-of-freedom. Shown in Table 5.5 is a summary of the 17 studies performed and their χ^2. The number of degrees-of-freedom is 7. The 17 χ^2 values are plotted in Fig. 5.18 along with the expected χ^2 distribution for 17 studies and 7 degrees-of-freedom. The mean of the χ^2 distribution from the data is 7.50 $\pm$ 1.14. The mean of the expected curve is 7. These are consistent within statistics. To estimate a limit on the possible systematic error we took the mean of 7.5 and divided it by the number of degrees-of-freedom. This yielded a reduced χ^2 of 1.07. If there were no systematic error the reduced χ^2 would be 1. That is, the contribution to reduced χ^2 from statistics is 1. The rest we attribute to systematics. To estimate the systematic error we multiplied $\sqrt{0.07}$ times the statistical error of our final answer. Therefore the estimate of the systematic error from the variation of the answer with respect to the cuts is $\pm$ 0.023.

The summary of the four contributions to the systematic error of α_γ are given in Table 5.6. The final systematic error is just the sum in quadrature of these four, $\pm$ 0.045. Therefore the asymmetry parameter of $\Sigma^+ \rightarrow p\gamma$ is α_γ = -0.720 $\pm$ 0.086

α_γ versus	χ^2 for 7 degrees-of-freedom
x proton position	6.44
time(run number)	13.23
z vertex	4.91
TRD low χ^2	4.9
TRD high χ^2	0.0058
m_x^2 in S	12.21
local energy cut	7.52
Σ^+ momentum	12.4
proton momentum	13.47
$\chi^2_{hyperon}/\nu$	4.81
χ^2_{baryon}/ν	8.69
y_{Σ^+} at target	7.10
y proton position	3.12
x neutral position	5.18
m_x^2 $K^+ \rightarrow \pi^+ X$	1.29
y photon position	5.29
x_{Σ^+} at target	16.97

Table 5.5: List of χ^2 for variation of α_γ with the cuts listed. The number of degrees-of-freedom is $\nu = 7$.

Source	error
Background z false asymmetry	$\pm$ 0.020
TRD algorithms	$\pm$ 0.022
Bias cancelling technique	$\pm$ 0.025
Cuts	$\pm$ 0.023
added in quadrature	$\pm$ 0.045

Table 5.6: The four contributions to the systematic error of α_γ. The resultant systematic error is just the four errors added in quadrature, $\pm$ 0.045.

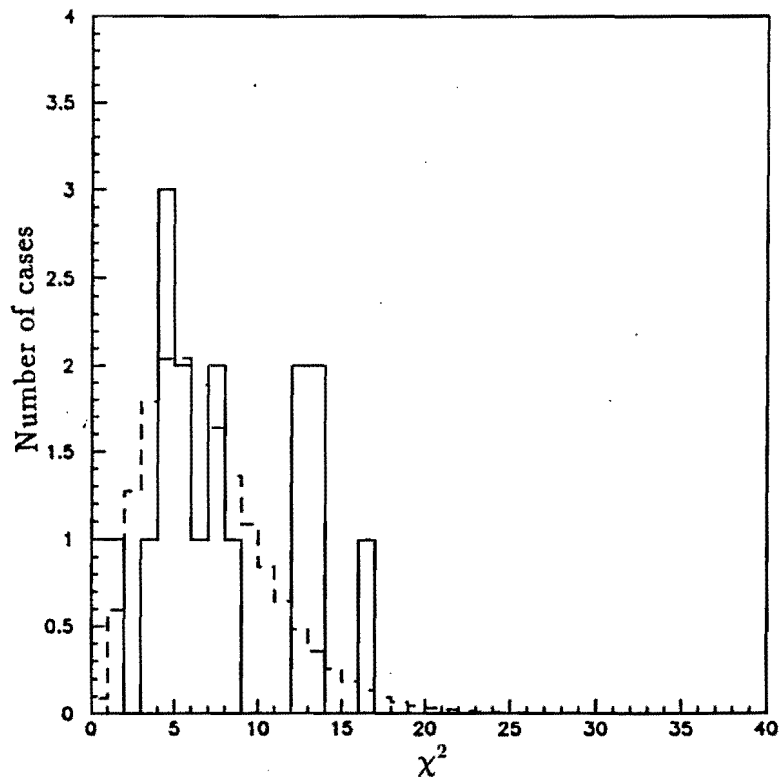

Figure 5.18: Ths χ^2 distribution for variation studies (solid line.) The dashed curve is the expected χ^2 distribution for 17 studies and 7 degrees-of-freedom. The mean of the data is 7.50 ± 1.14. The mean of the expected curve is 7.

(statistical) $\pm$ 0.045 (systematic).

Chapter 6

Branching Ratio $\Sigma^+ \rightarrow p\gamma$

We measured the branching ratio

$$\frac{\mathrm{Br}(\Sigma^+ \rightarrow p\gamma\ )}{\mathrm{Br}(\Sigma^+ \rightarrow p\pi^0\ )} = \frac{\left(\frac{N_\gamma}{\epsilon_\gamma^{full}}\right)}{\left(\frac{N_\pi}{\epsilon_\pi}\right)} \tag{6.1}$$

where N_γ is the number of $\Sigma^+ \rightarrow p\gamma$, N_π is the number of $\Sigma^+ \rightarrow p\pi^0$, ϵ_γ^{full} is the full efficiency for $\Sigma^+ \rightarrow p\gamma$ and ϵ_π is the efficiency for $\Sigma^+ \rightarrow p\pi^0$. The full efficiency, ϵ_γ^{full}, is the product of the geometrical efficiency (acceptance), trigger efficiency, software reconstruction efficiency and ϵ_γ^{TRD} which is the efficiency of the TRD algorithm to extract $\Sigma^+ \rightarrow p\gamma$. We separate ϵ_γ^{TRD} from ϵ_γ^{full} because it is a special efficiency relevant only for $\Sigma^+ \rightarrow p\gamma$ not $\Sigma^+ \rightarrow p\pi^0$. Therefore

$$\frac{\mathrm{Br}(\Sigma^+ \rightarrow p\gamma\ )}{\mathrm{Br}(\Sigma^+ \rightarrow p\pi^0\ )} = \frac{N_\gamma \epsilon_\pi}{N_\pi \epsilon_\gamma \epsilon_\gamma^{TRD}} \tag{6.2}$$

where ϵ_π and ϵ_γ are the combined geometrical efficiency, trigger efficiency and software reconstruction efficiency for $\Sigma^+ \rightarrow p\gamma$ and $\Sigma^+ \rightarrow p\pi^0$, respectively. We counted the number of events from the PRE and PGAM sample and the efficiency ϵ_π and ϵ_γ was measured by a Monte Carlo technique and ϵ_γ^{TRD} was measured using the data. We measured the branching ratio for positive and negative targeting angle separately. This is a preliminary result and work is continuing on this measurement.

6.1 Number of $\Sigma^+ \rightarrow p\pi^0$

We used the following cuts on both samples of $\Sigma^+ \rightarrow p\gamma$ and $\Sigma^+ \rightarrow p\pi^0$

$$\chi^2_{hyperon} < 4$$
$$\chi^2_{baryon} < 2$$
$$100 < \text{z vertex} \leq 1200 \text{ cm from SD3}$$
$$325 < \text{hyperon momentum} < 425 \text{ GeV/c}$$
$$\text{r(ratio of baryon momentum over hyperon momentum)} < 1$$
$$\theta_{op} \geq 100\ \mu\text{rad OR r} \leq 0.97$$
$$9.1 < \text{x of proton at first steel plate} < 15.1 \text{ cm}$$

The last cut on the position of the proton has been added to avoid any possible discrepancy between experimental and Monte Carlo simulation geometries. The z vertex cut was tightened because we know that there is some excess background near SD3 from interactions. We measured the branching ratio with events that showered in the first and second steel plate, no rear photon events. Shown in Fig. 6.1 is the x distribution of the proton at the first steel plate for positive targeting angle. The cut shown by the lines was made. The number of $\Sigma^+ \rightarrow p\pi^0$ in the sample was determined from the PRE sample. The PRE sample was analyzed using the above cuts. The missing-mass-squared distribution for positive targeting angle is given in Fig. 6.2. We assume there is a linear background under the peak shown in Fig. 6.2. The number of $\Sigma^+ \rightarrow p\pi^0$ is just the number in the histogram minus the background. We found in the PRE sample for positive targeting angle 392810 $\pm$ 630 $\Sigma^+ \rightarrow p\pi^0$ and for negative targeting angle 392290 $\pm$ 630 $\Sigma^+ \rightarrow p\pi^0$. The background was a 3% correction to the number of $\Sigma^+ \rightarrow p\pi^0$. To determine the number of $\Sigma^+ \rightarrow p\pi^0$ in the full data sample, N_π, we need to know the prescale factor with the cuts used. This was the factor to multiply the number of $\Sigma^+ \rightarrow p\pi^0$ in the PRE sample to determine, N_π. A positive and negative targeting angle run were taken and analyzed with the above cuts to determine the number of $\Sigma^+ \rightarrow p\pi^0$. The PRE samples from those same runs were analyzed to determine the number of $\Sigma^+ \rightarrow p\pi^0$. Their ratio is the prescale factor. The prescale factor for positive targeting angle is 44.61 $\pm$ 0.79 and negative

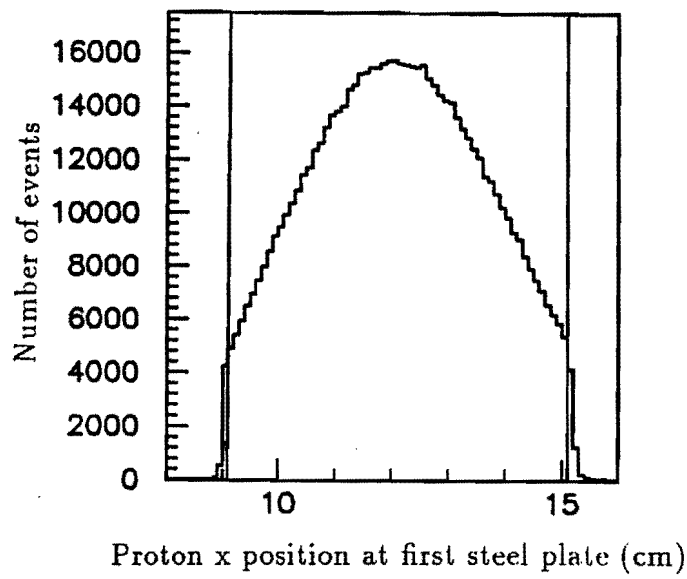

Figure 6.1: x distribution (cm) of the proton at the first steel plate for positive targeting angle for $\Sigma^+ \rightarrow p\pi^0$. The cut shown by the lines was made.

targeting angle is 46.90 ± 0.86. Therefore the number of $\Sigma^+ \rightarrow p\pi^0$, N_π for positive targeting angle was $(1.752 \pm 0.034) \times 10^7$ $\Sigma^+ \rightarrow p\pi^0$ and for negative targeting angle was $(1.845 \pm 0.037) \times 10^7$ $\Sigma^+ \rightarrow p\pi^0$.

6.2 Efficiency for $\Sigma^+ \rightarrow p\pi^0$ and $\Sigma^+ \rightarrow p\gamma$

The efficiencies for $\Sigma^+ \rightarrow p\pi^0$ and $\Sigma^+ \rightarrow p\gamma$, ϵ_π and ϵ_γ were determined by Monte Carlo techniques. The Monte Carlo calculation is a computer program that simulates the experiment as closely as possible. We used GEANT [64] 3.14 to model the experiment. We started the Monte Carlo calculation from beam tracks that we reconstructed from the data. These Σ^+ beam tracks were allowed to decay by the decay mode of our choosing. For the charged particles, Σ^+ and proton, hits were placed on the SSD and PWC wires. For the neutral particle, the photon, electromagnetic showers were simulated. Multiple Coulomb scattering was also simulated. At the end of each generated event we wrote out the information in E761 data format. We then analyzed these Monte Carlo events using the same program used to analyze the real data. Shown in Fig. 6.3, Fig. 6.4, Fig. 6.5 and Fig. 6.6 are the comparison of the

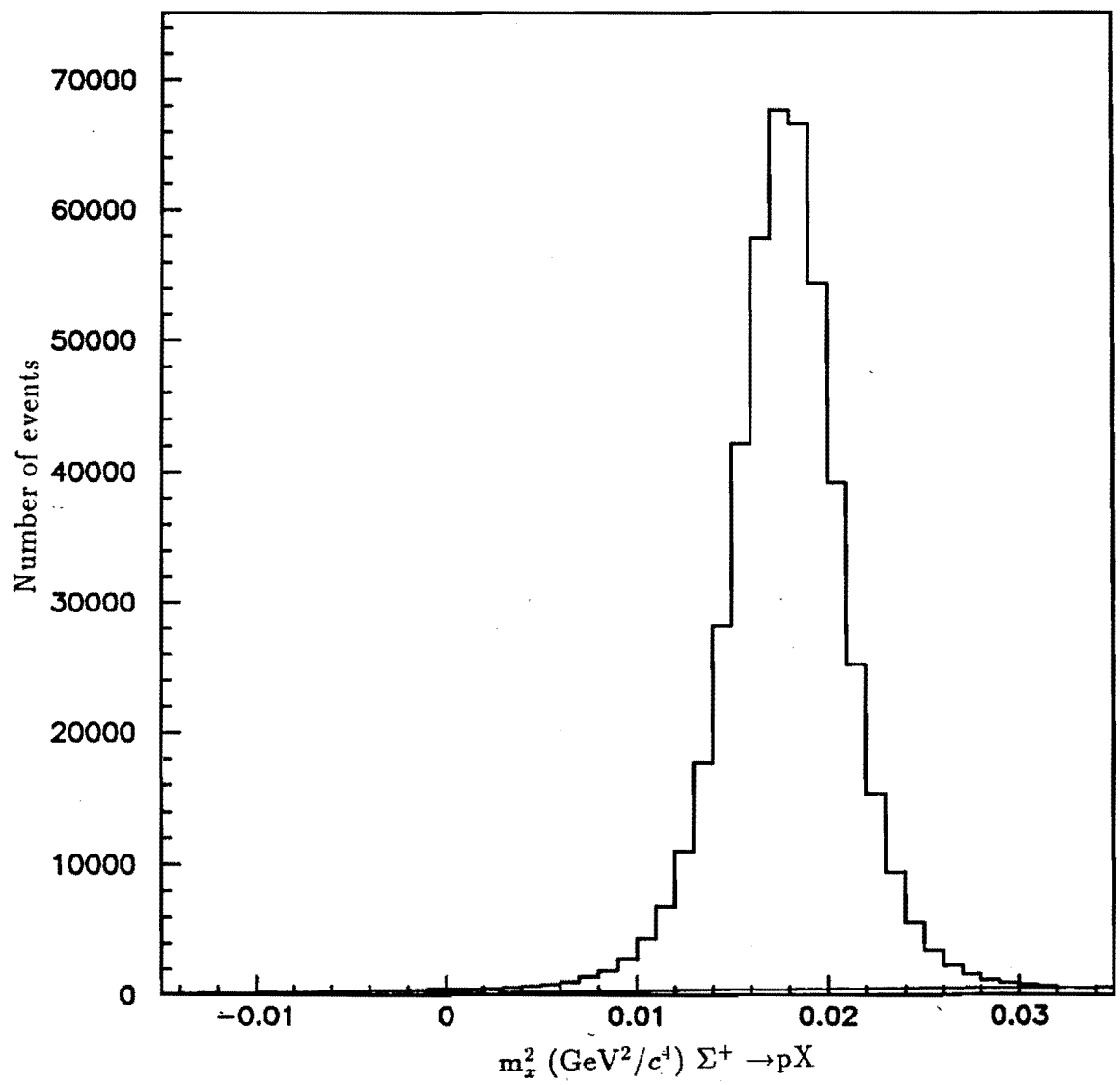

Figure 6.2: Missing-mass-squared distribution (GeV$^2/c^4$) m_x^2, $\Sigma^+ \rightarrow$pX , for positive targeting angle. The linear background is shown.

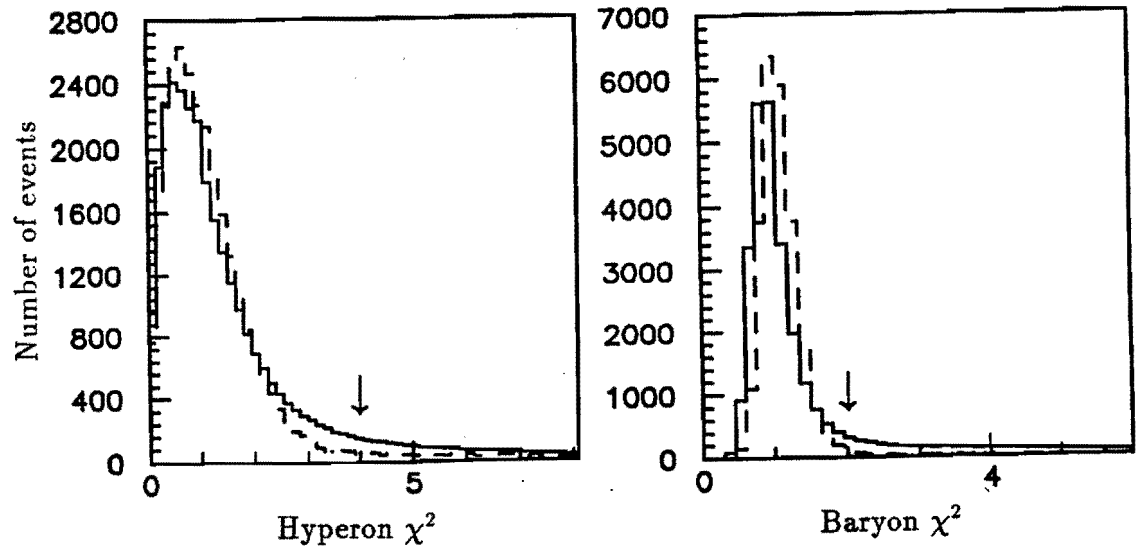

Figure 6.3: $\Sigma^+ \rightarrow p\pi^0$ data versus Monte Carlo positive targeting angle, Hyperon reduced χ^2 distribution (left) and baryon reduced χ^2 distribution (right.) Solid is data and dashed is Monte Carlo. We make the cuts and normalization at the arrows.

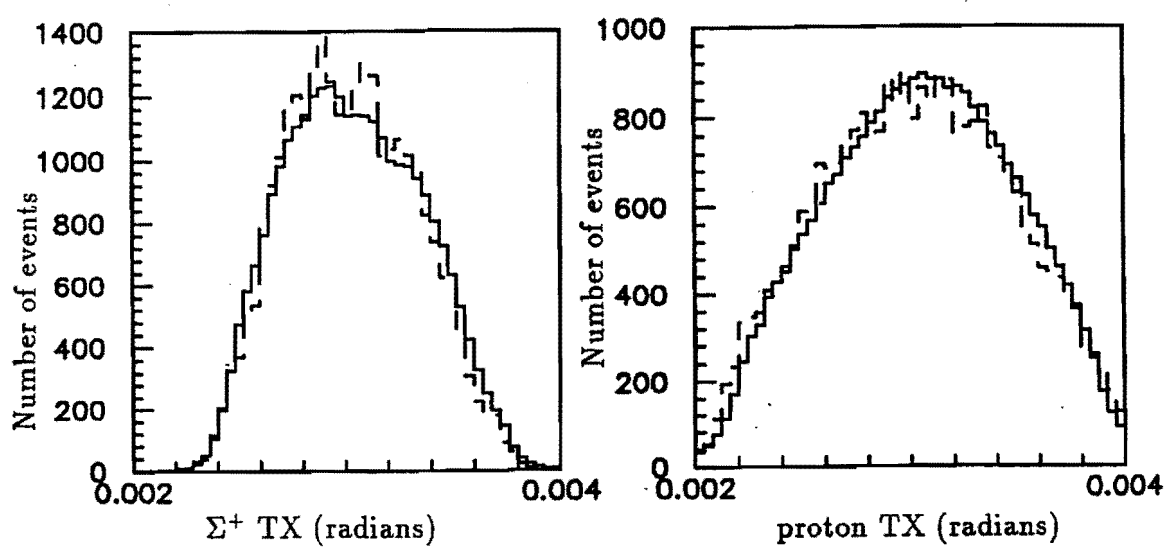

Figure 6.4: $\Sigma^+ \rightarrow p\pi^0$ data versus Monte Carlo positive targeting angle, TX (radians) of Σ^+ (left) and TX (radians) of proton (right.) Solid is data and dashed is Monte Carlo.

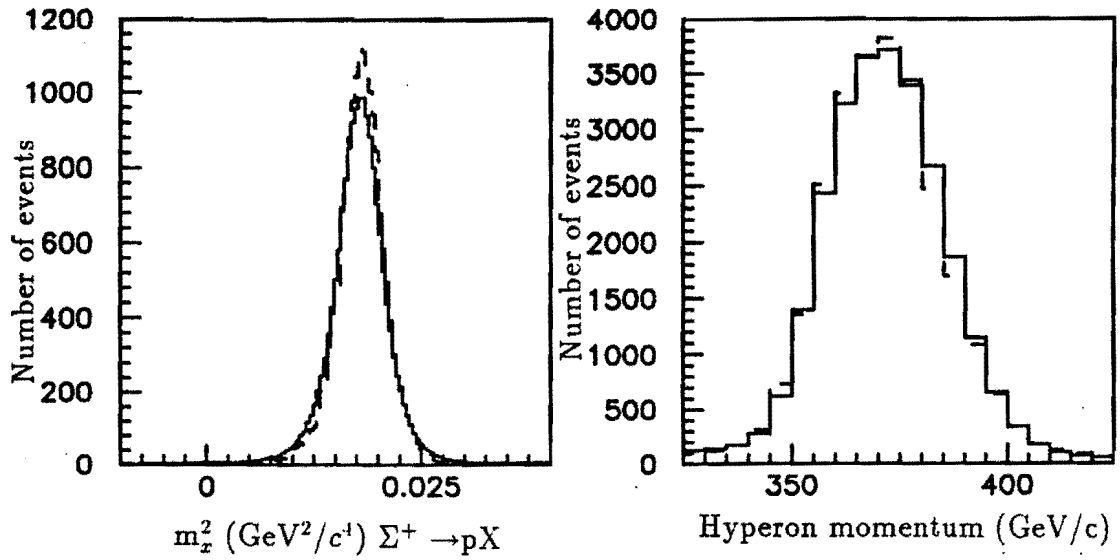

Figure 6.5: $\Sigma^+ \rightarrow p\pi^0$ data versus Monte Carlo positive targeting angle, m_x^2 (GeV^2/c^4) $\Sigma^+ \rightarrow pX$ (left) and momentum (GeV/c) of Σ^+ (right.) Solid is data and dashed is Monte Carlo.

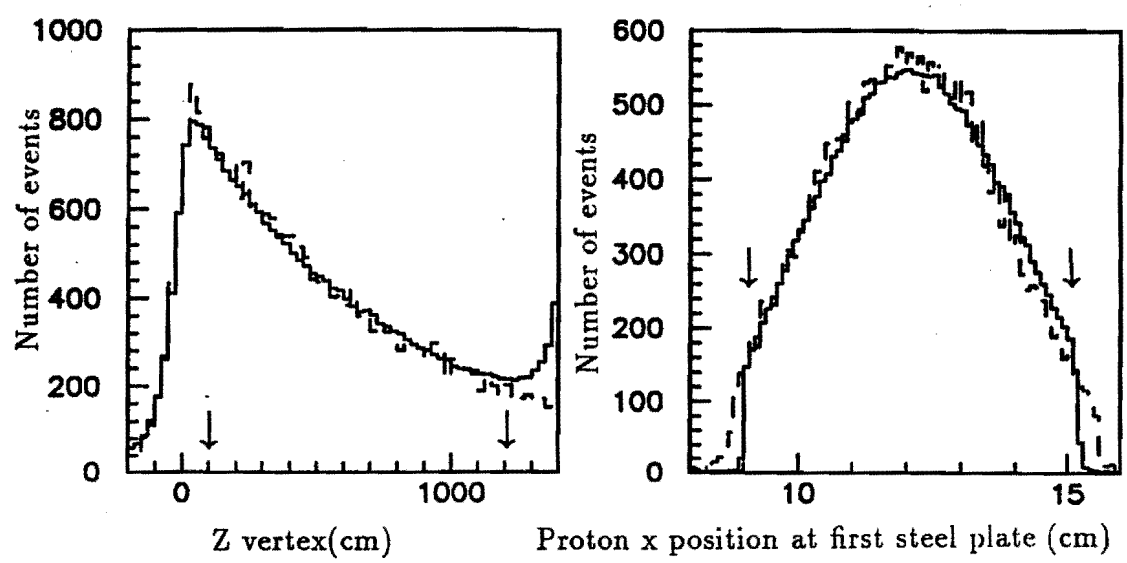

Figure 6.6: $\Sigma^+ \rightarrow p\pi^0$ data versus Monte Carlo positive targeting angle, z vertex (cm) distribution (left) and x position (cm) of proton at the first steel plate (right.) Solid is data and dashed is Monte Carlo. We make the cuts and normalization at the arrows.

data with the Monte Carlo calculation for some of the measured quantities for positive targeting angle $\Sigma^+ \rightarrow p\pi^0$ events. Solid lines represent the data and dashed lines the Monte Carlo simulation. The distributions are normalized to equal area within the cut area. From studies of the trigger rates using $\Sigma^+ \rightarrow p\pi^0$ from the beam we believe we can model the absolute efficiency of $\Sigma^+ \rightarrow p\pi^0$ to a few percent. Therefore we can determine the ratio of efficiencies, $\epsilon_\pi/\epsilon_\gamma$ to better than a few percent. The hyperon and baryon reduced χ^2 distributions do not quite match the Monte Carlo simulation. The data of course has more events at higher χ^2 than the Monte Carlo simulation. The z vertex distributions agree within the cut region,despite the peak in the data at 1400 cm. This peak was caused by decays downstream of WA for which the offline reconstruction incorrectly assigned the z vertex at WA (1400cm.) The Monte Carlo simulation does not show this feature because the decays were forced to occur from -150 cm to 1500 cm. We found for the efficiency of $\Sigma^+ \rightarrow p\pi^0$, $\epsilon_\pi = 0.4018 \pm 0.0026$ for positive targeting angle and $\epsilon_\pi = 0.3879 \pm 0.0026$ for negative targeting angle. These efficiencies are the efficiencies relative to a Monte Carlo sample created with a set of cuts looser than that used to measure the branching ratio. For example the generated z vertex is from -150 to 1500 cm, whereas for the branching ratio sample we cut z vertex from 100 to 1200 cm.

We applied this same Monte Carlo technique to determine the efficiency for $\Sigma^+ \rightarrow p\gamma$, ϵ_γ. Shown in Fig. 6.7, Fig. 6.8, Fig. 6.9, Fig. 6.10 and Fig. 6.11 are the comparison of the data with the Monte Carlo calculation for some of the measured quantities for positive targeting angle $\Sigma^+ \rightarrow p\gamma$ events. Solid lines represent the data and dashed lines the Monte Carlo simulation. The distributions are normalized to equal area within the cut area. An additional cut on the position of the photon at the TRD was made. Shown in Fig. 6.12 is the position of the cut used. The photon must be well within the TRD (5cm inside the active area of the TRD aperture) and outside (3 cm) the edge of the hole in the steel plate. This is to assure that we measure well the efficiency, ϵ_γ, by not having any systematic error due to events with the photon near the edge of the hole. We find for positive targeting angle $\epsilon_\gamma = 0.2034 \pm 0.0020$ and for negative targeting angle $\epsilon_\gamma = 0.1929 \pm 0.0020$.

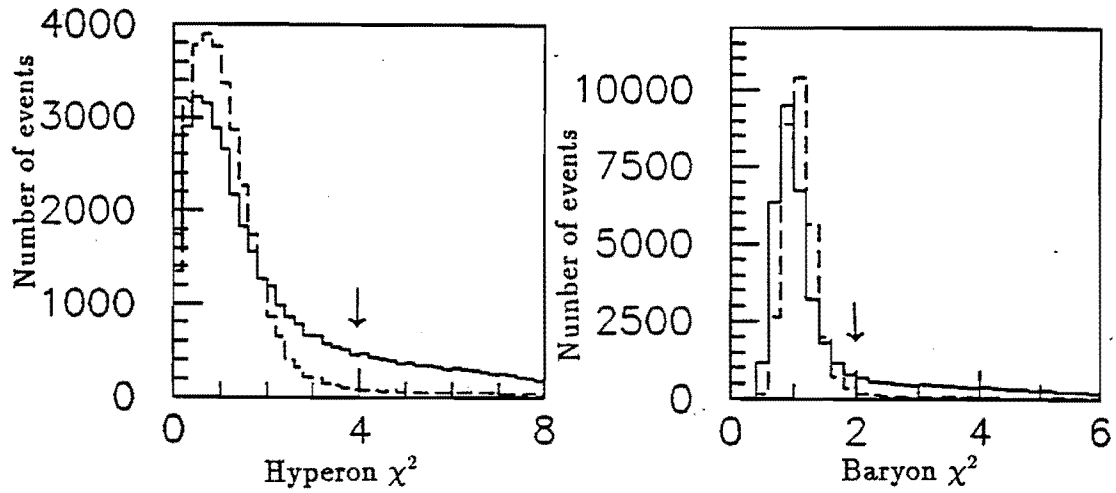

Figure 6.7: $\Sigma^+ \rightarrow p\gamma$ data versus Monte Carlo positive targeting angle, Hyperon reduced χ^2 distribution (left) and baryon reduced χ^2 distribution (right.) Solid is data and dashed is Monte Carlo. We make the cuts and normalization at the arrows.

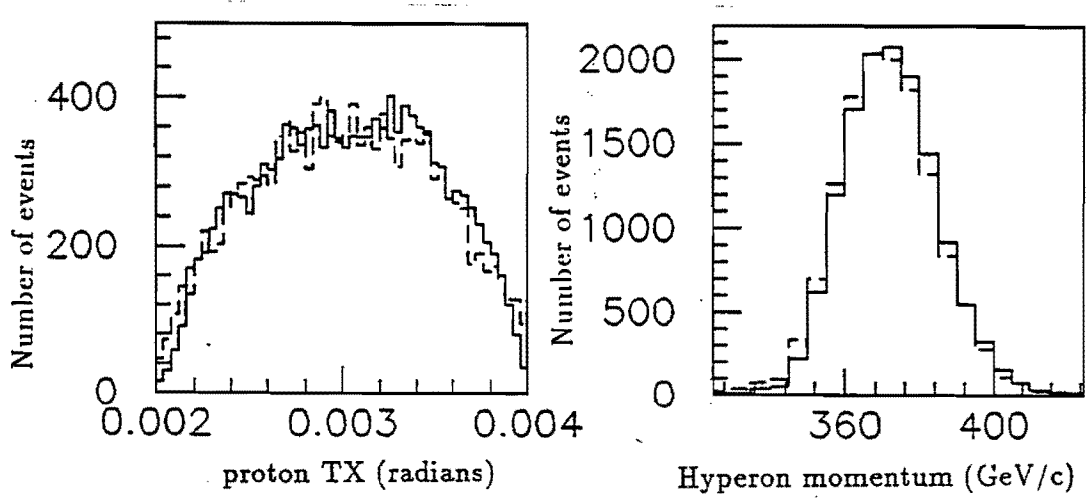

Figure 6.8: $\Sigma^+ \rightarrow p\gamma$ data versus Monte Carlo positive targeting angle, TX (radians) of proton (left) and momentum (GeV/c) of Σ^+ (right.) Solid is data and dashed is Monte Carlo.

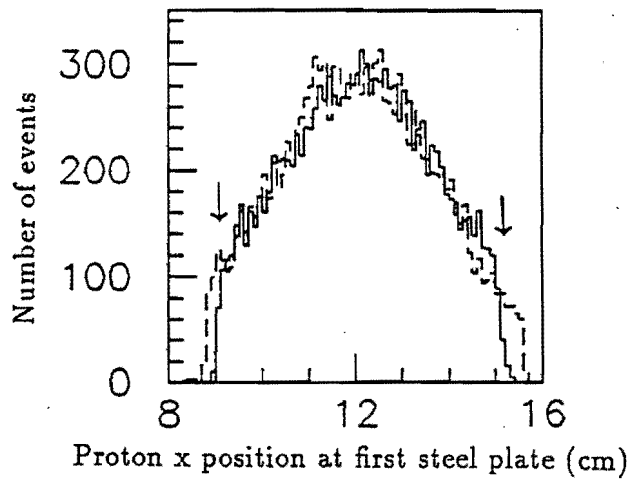

Figure 6.9: $\Sigma^+ \rightarrow p\gamma$ data versus Monte Carlo positive targeting angle, x position (cm) of proton at the first steel plate. Solid is data and dashed is Monte Carlo. We make the cuts and normalization at the arrows.

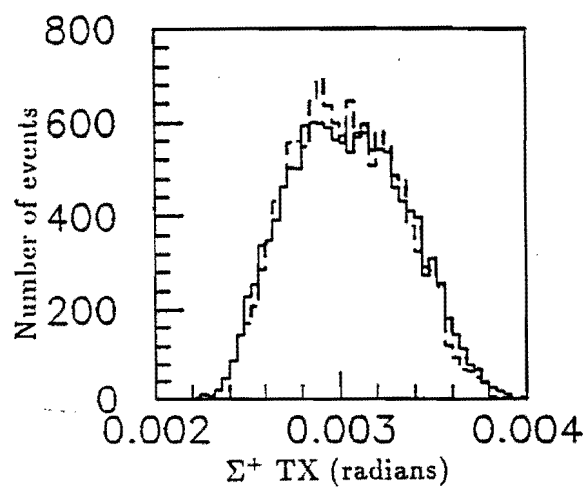

Figure 6.10: $\Sigma^+ \rightarrow p\gamma$ data versus Monte Carlo positive targeting angle, TX (radians) of Σ^+. Solid is data and dashed is Monte Carlo.

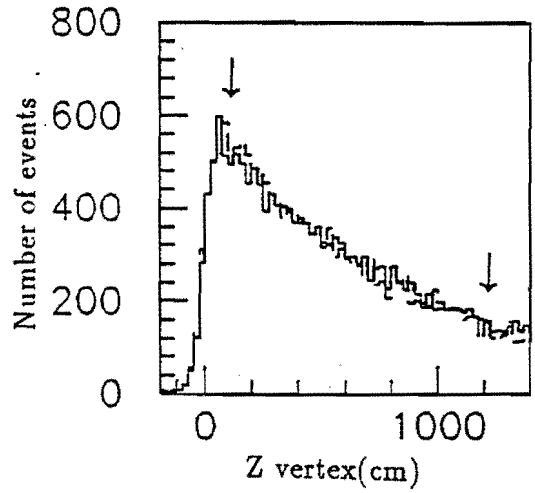

Figure 6.11: $\Sigma^+ \rightarrow p\gamma$ data versus Monte Carlo positive targeting angle, z vertex (cm) distribution. Solid is data and dashed is Monte Carlo. We make the cuts and normalization at the arrows.

6.3 Number of $\Sigma^+ \rightarrow p\gamma$

To find the number of $\Sigma^+ \rightarrow p\gamma$ in the sample we applied the same cuts used in the $\Sigma^+ \rightarrow p\gamma$ Monte Carlo simulation as to the PGAM data sample. To improve the signal to noise we apply 2 more cuts. These 2 cuts are from the TRD algorithm used to extract $\Sigma^+ \rightarrow p\gamma$. We used the Moriond TRD algorithm defined in Section 5.4.2. The TRD algorithm starts by calculating the neutral track (X particle) from the decay $\Sigma^+ \rightarrow pX$ from the charged tracks Σ^+ and proton. We call this track the extrapolated neutral track. We projected this track onto the photon spectrometer. The first cut required at least 50% of the energy in the photon calorimeter be within 5 cm of the extrapolated neutral track. We called this the local sum cut. We looked in a window ± 5 cm wide around the extrapolated neutral track and formed a TRD χ^2 of the miss distance from the neutral track to the closest wire on. We summed this χ^2 over the 8 planes in the photon spectrometer. We used the wire spacing divided by $\sqrt{12}$ to normalize the TRD χ^2. To isolate $\Sigma^+ \rightarrow p\gamma$ we made a cut TRD $\chi^2 \leq 500$. The missing-mass-squared distribution for these 2 cuts is shown in Fig. 6.13.

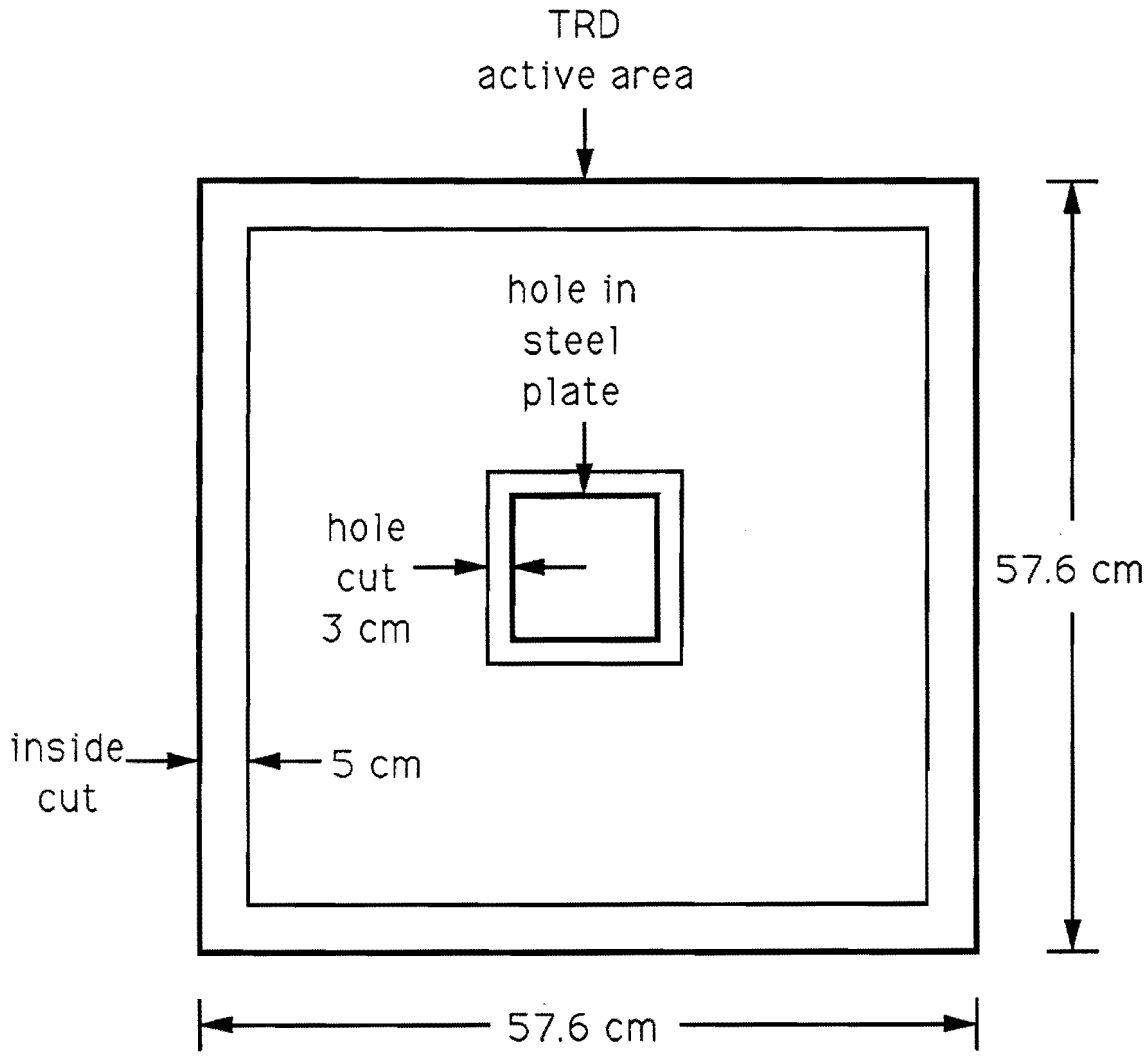

Figure 6.12: Position cut on the photon from $\Sigma^+ \rightarrow p\gamma$. The photon had to be inside of 5 cm of the outer edge of the TRD active area and outside of 3 cm of the hole in the steel plate.

There is a clear peak at 0 indicating $\Sigma^+ \rightarrow p\gamma$. To determine the number of $\Sigma^+ \rightarrow p\gamma$ we fitted Fig. 6.13 to the functional form

$$\frac{P_1}{\sqrt{2\pi}P_3}e^{-\frac{1}{2}\frac{(x-P_2)^2}{P_3^2}} + P_4 + P_5x + e^{(P_6 + P_7x + P_8x^2)} \tag{6.3}$$

where x is the missing-mass-squared and P_i are the parameters that are allowed to vary. First the region -0.0100 $\rightarrow$ -0.0060 GeV$^2/c^4$ was fitted to

$$P_4 + P_5x \tag{6.4}$$

only. Then the region 0.0060 $\rightarrow$ 0.0100 GeV$^2/c^4$ was fitted to

$$P_4 + P_5x + e^{(P_6 + P_7x + P_8x^2)} \tag{6.5}$$

with parameters P_4 and P_5 fixed. The final fit was performed to the full function with P_6, P_7 and P_8 fixed. Shown in Fig. 6.13 is the fit of the Gaussian plus background (solid line through all data points) and just the background with Gaussian (solid line underneath $\Sigma^+ \rightarrow p\gamma$ peak.) The background extrapolates smoothly under the peak. The number of $\Sigma^+ \rightarrow p\gamma$ for positive targeting angle is given by the parameter P_1. We found P_1 = 15,630 $\pm$ 330 $\Sigma^+ \rightarrow p\gamma$. The fit χ^2/ν was 1.4 for ν = 42 degrees-of-freedom. To take into account that the reduced χ^2 is not 1 we increase the error in the number of $\Sigma^+ \rightarrow p\gamma$ by the square root of reduced χ^2. We found for positive targeting angle 15,630 $\pm$ 390 $\Sigma^+ \rightarrow p\gamma$ and for negative targeting angle 16,950 $\pm$ 560 events.

6.4 Efficiency of TRD algorithm

We need to know the efficiency of the 50% local sum cut and the TRD $\chi^2 \leq 500$ cut. To determine this we needed a sample of single photon events where we know the position of the photon on the TRD. We used events $\Sigma^+ \rightarrow p\pi^0$, $\pi^0 \rightarrow \gamma_1\gamma_2$, where γ_1 went into the hole in the photon spectrometer and γ_2 went into the steel/TRD/photon calorimeter. This type of event is illustrated in Fig. 6.14. From the Σ^+ and proton track the complete information on the π^0can be reconstructed. The WD1XY and

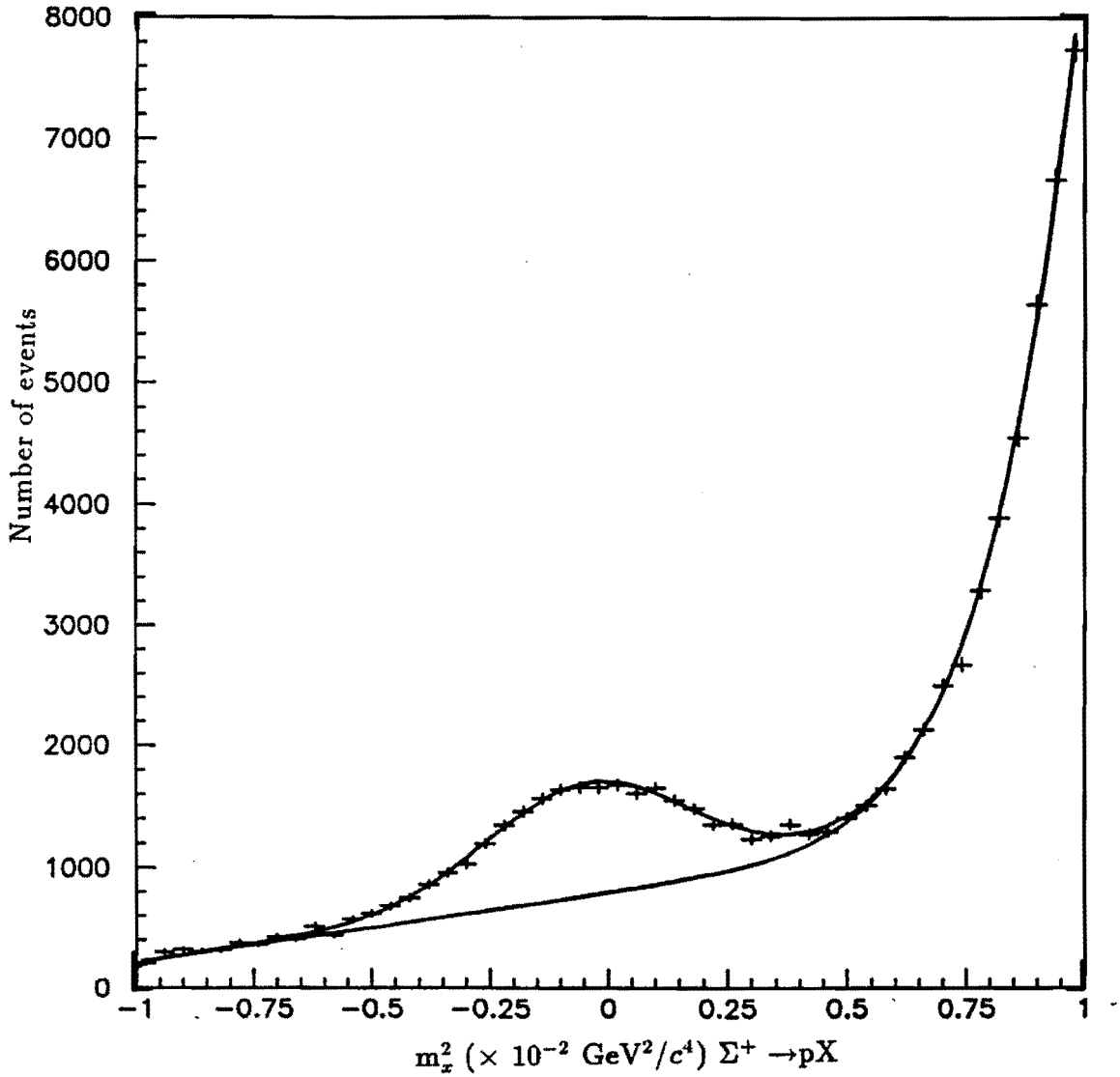

Figure 6.13: Missing-mass-squared distribution (GeV$^2/c^4$) m_x^2, $\Sigma^+ \rightarrow$pX , for a TRD $\chi^2 \leq 500$ and local sum cut of 50% for positive targeting angle (data points with error bars.) The fit with gaussian is the curve through the points.

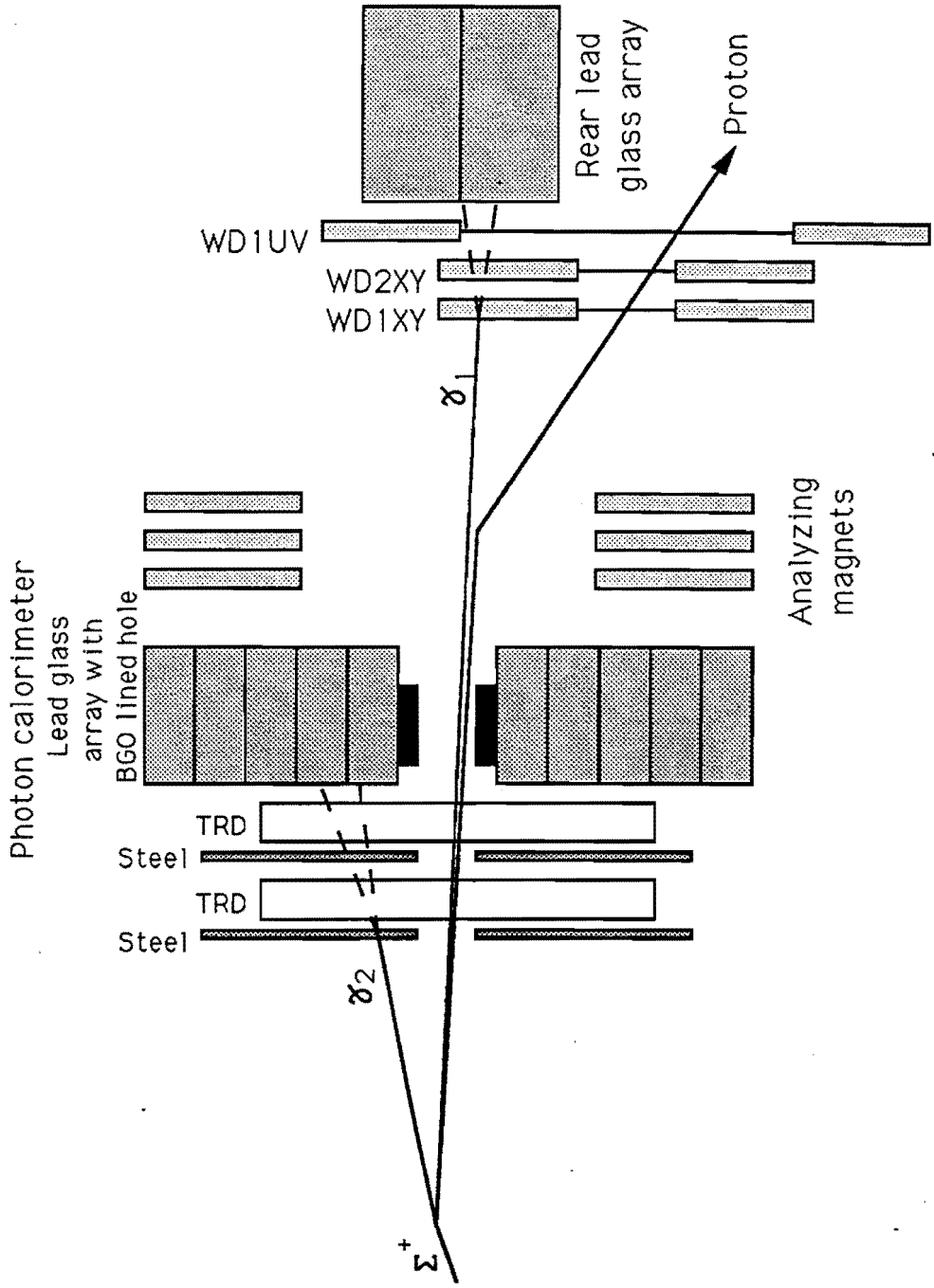

Figure 6.14: Single photon event topology. The event is a $\Sigma^+ \rightarrow p\pi^0$, $\pi^0 \rightarrow \gamma_1\gamma_2$ where one photon goes into the rear lead glass array and one photon goes into the photon calorimeter.

	Positive targeting angle	Negative targeting angle
N_π	$(1.752 \pm 0.034) \times 10^7$	$(1.845 \pm 0.037) \times 10^7$
ϵ_π	0.4018 ± 0.0026	0.3879 ± 0.0026
N_γ	$15{,}630 \pm 390$	$16{,}950 \pm 560$
ϵ_γ	0.2034 ± 0.0020	0.1929 ± 0.0020
ϵ_γ^{TRD}	0.838 ± 0.021	0.838 ± 0.021
$Br(\Sigma^+ \rightarrow p\gamma)/Br(\Sigma^+ \rightarrow p\pi^0)$	$(2.104 \pm 0.088) \times 10^{-3}$	$(2.206 \pm 0.100) \times 10^{-3}$

Table 6.1: The branching ratio $Br(\Sigma^+ \rightarrow p\gamma)/Br(\Sigma^+ \rightarrow p\pi^0)$ for positive and negative targeting angle.

WD2XY wire chamber frames partially covered the area where the photons that went into the hole would go. Some of these photons initiated showers in the frames of WD1XY and WD2XY. Behind WD1XY and WD2XY was the WD1UV plane rotated 45° with respect to WD1XY and WD2XY. The position of the photon was measured in WD1UV and the energy was measured in the rear lead glass array. We knew the position of the decay vertex $\Sigma^+ \rightarrow p\pi^0$, $\pi^0 \rightarrow \gamma_1\gamma_2$. Therefore we know the complete 4-vector of the π^0 and γ_1. We then reconstructed the 4-vector of γ_2. Using this single photon sample, γ_2, we measured the efficiency of the TRD algorithm and local sum cut, ϵ_γ^{TRD}. We find for the efficiency $\epsilon_\gamma^{TRD} = 0.838 \pm 0.021$.

6.5 Branching ratio $\Sigma^+ \rightarrow p\gamma$

We can now combine all the numbers to determine the branching ratio $Br(\Sigma^+ \rightarrow p\gamma)/Br(\Sigma^+ \rightarrow p\pi^0)$. The results for positive and negative targeting angle are shown in Table 6.1. We found for the combined positive and negative targeting angle $Br(\Sigma^+ \rightarrow p\gamma)/Br(\Sigma^+ \rightarrow p\pi^0) = (2.147 \pm 0.068) \times 10^{-3}$. This is a preliminary result. We have only performed preliminary systematic studies, varying the cuts and fitting procedure. We estimate our systematic error to be $(\pm\ 0.107) \times 10^{-3}$ in the ratio of branching

ratios. Therefore the branching ratio $Br(\Sigma^+ \rightarrow p\gamma)/Br(\Sigma^+ \rightarrow p\pi^0) = (2.147 \pm 0.068 \pm 0.107) \times 10^{-3}$ where the first error is statistical and the second systematic. Using the known value [2] of $Br(\Sigma^+ \rightarrow p\pi^0) = 0.5157 \pm 0.0030$, we find $Br(\Sigma^+ \rightarrow p\gamma) = (1.107 \pm 0.035 \pm 0.055) \times 10^{-3}$ where the first error is statistical and the second is systematic.

The improvement of this result is continuing. From Table 6.1 the most significant contributions to the error in the branching ratio are N_γ, ϵ_γ^{TRD} and N_π. To better determine N_γ we can try to improve the fitting procedure. We will also use the TRD algorithm used to determine the asymmetry parameter. The efficiency, ϵ_γ^{TRD}, must be measured for this algorithm. N_γ and ϵ_γ^{TRD} are highly related. If we tighten the cut in the TRD algorithm to improve the signal to noise the error in N_γ will decrease. Unfortunately the efficiency, ϵ_γ^{TRD}, will drop and become harder to measure. We also can put the target in the hyperon track fitting. This we have seen can give us an enormous improvement in the separation of $\Sigma^+ \rightarrow p\gamma$ and $\Sigma^+ \rightarrow p\pi^0$. It is possible that we can measure the branching ratio without using the TRD. This will be a good cross check on the result. To reduce the uncertainty on N_π we will go back and measure the prescale factor over a larger sample of the data possibly the whole sample. Systematic studies will continue. The stability of the result will be checked with respect to the cuts. Of course we will try to improve the agreement between the data and the Monte Carlo simulation. In my opinion we can probably achieve no more than a factor of 2 improvement in the error.

Chapter 7

Conclusion

We have performed a high statistics measurement of the asymmetry parameter in the hyperon radiative decay $\Sigma^+ \rightarrow p\gamma$ in Fermilab experiment 761. We find for the asymmetry parameter -0.720 $\pm$ 0.086 $\pm$ 0.045 where the first error is statistical and the second is systematic. Shown in Fig. 7.1 is a comparison of our measurement with the previous measurements. Our result agrees well with previous experiments with a $\chi^2 = 1.43$ for 3 degrees-of-freedom. The new world average for the asymmetry parameter for $\Sigma^+ \rightarrow p\gamma$ is -0.764 $\pm$ 0.076.

We have also measured the branching ratio $Br(\Sigma^+ \rightarrow p\gamma)/Br(\Sigma^+ \rightarrow p\pi^0) = (2.147 \pm 0.068 \pm 0.107) \times 10^{-3}$ where the first error is statistical and the second is systematic. Using the known value [2] of $Br(\Sigma^+ \rightarrow p\pi^0)/Br(\Sigma^+ \rightarrow \text{all})$ of 0.5157 $\pm$ 0.0030 the branching ratio $Br(\Sigma^+ \rightarrow p\gamma)/Br(\Sigma^+ \rightarrow \text{all})$ is $(1.107 \pm 0.035 \pm 0.055) \times 10^{-3}$ where the first error is statistical and the second is systematic. This is a preliminary measurement of the branching ratio and more work is currently in progress. Shown in Fig. 7.2 is a comparison of our measurement with the previous measurements. Our result agrees with previous experiments with a $\chi^2 = 8.00$ for 7 degrees-of-freedom. Combining our preliminary result with the previous measurements yields a branching ratio $Br(\Sigma^+ \rightarrow p\gamma)/Br(\Sigma^+ \rightarrow \text{all})$ of $(1.173 \pm 0.048) \times 10^{-3}$.

Many of the models discussed in chapter 1 have been ruled out by these measurements. Some of the models are able to predict the correct branching ratio and asymmetry parameter of $\Sigma^+ \rightarrow p\gamma$ but fail to reproduce the branching ratios and

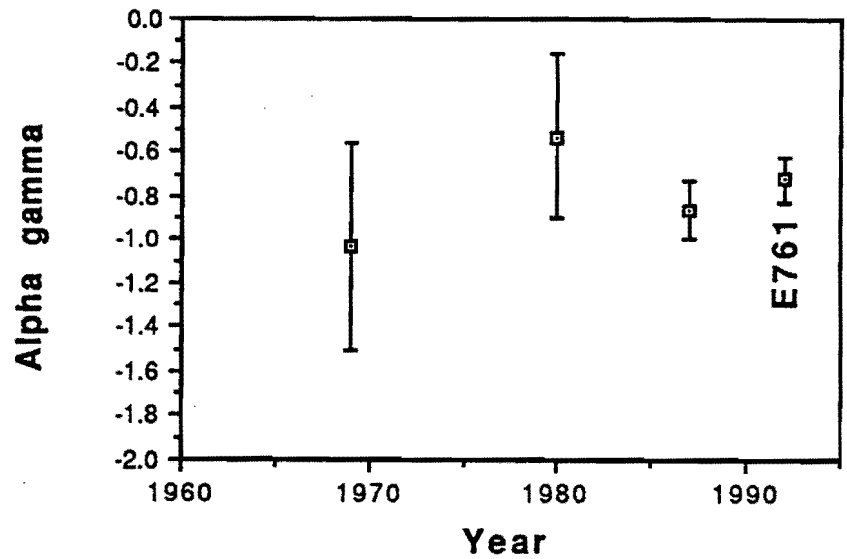

Figure 7.1: Comparison of our asymmetry parameter of $\Sigma^+ \rightarrow p\gamma$ result with the 3 previous experiments.

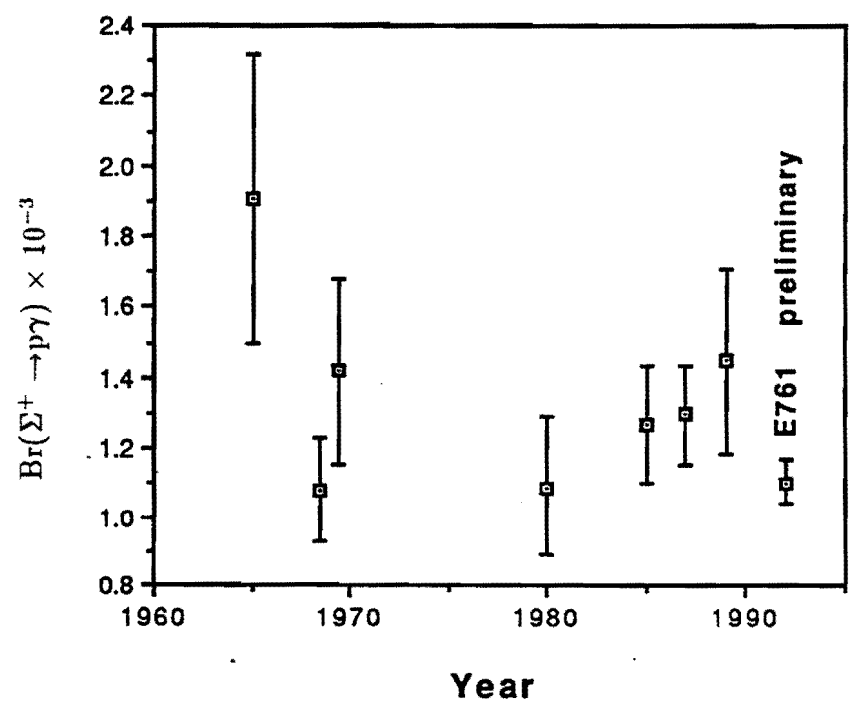

Figure 7.2: Comparison of our branching ratio $\Sigma^+ \rightarrow p\gamma$ result with the previous experiments. The units are 10^{-3}.

asymmetry parameters of the other hyperon radiative decays that have been measured. Clearly the origin of the large negative asymmetry parameter is not some naive breaking of SU(3) which predicts a small positive value for the asymmetry. Single quark transitions and two quark transitions can not be the only mechanism involved because they gave branching ratios and asymmetry parameters that are too small. The model of Balitsky *et al* [38], using QCD sum rules, shows agreement with these results. They predicted $Br(\Sigma^+ \rightarrow p\gamma) = (0.5 - 1.5) \times 10^{-3}$ and an asymmetry parameter of -0.85 $\pm$ 0.15. They do not make any predictions on any of the other hyperon radiative decays. It would be interesting to see this model used to predict the branching ratio and asymmetry parameters of the other hyperon radiative decays. Close and Rubinstein [17] using a pole model also predicted the asymmetry parameter in agreement with these measurements. They predicted the asymmetry parameter for $\Sigma^+ \rightarrow p\gamma$ to be -0.6 $\rightarrow$ -1.0. However they didn't make a prediction of the branching ratio. Żenczykowski [39] using a combined symmetry/vector dominance model also predicted the branching ratio and the asymmetry parameter in relative agreement with our measurement. He predicted the asymmetry parameter of $\Sigma^+ \rightarrow p\gamma$ to be -0.96 and the branching ratio to be 1.33×10^{-3}. He believes these numbers are good to $\sim$15%. He also made predictions of other hyperon radiative decays in Table 1.11. We hope to test this model further by measuring the asymmetry parameter and branching ratio of $\Xi^- \rightarrow \Sigma^-\gamma$.

This experiment has provided new high quality data in the field of hyperon radiative decays. It confirms a large negative asymmetry for $\Sigma^+ \rightarrow p\gamma$ and the branching ratio of $\Sigma^+ \rightarrow p\gamma$ as measured by previous low statistics experiments. The results presented here have helped to clarify two important measurements in hyperon radiative decays. It is hoped that they can point the way to a clearer understanding of these decays. We also look forward to publishing new measurements on other hyperon radiative decays with the rest of the data we collected. We hope that these new high quality data will stimulate progress in this area.

Bibliography

[1] Particle Data Group, Phys. Lett. B **170**, 154(1986).

[2] Particle Data Group, Phys. Lett. B **239**, 1(1990).

[3] M. Kobayashi *et al*, Phys. Rev. Lett. **59**, 868(1987).

[4] A. Manz *et al*, Phys. Lett. **96B**, 217(1980).

[5] L. K. Gershwin *et al*, Phys. Rev. **188**, 2077(1969).

[6] N. P. Hessey *et al*, Z. Phys. C **42**, 175(1989).

[7] S. F. Biagi *et al*, Z. Phys. C **28**, 495(1985).

[8] G. Ang *et al*, Z Phys. **228**, 151(1969).

[9] M. Bazin *et al*, Phys. Rev. Lett. **14**, 154(1969).

[10] A. A. Vorobyov *et al*, Fermilab proposal 761, submitted April 1985.

[11] R. R. Marshak *et al*, Theory of Weak Interactions in Particle Theory, Wiley-Interscience, New York 660(1969)

[12] Y. Hara, Phys. Rev. Lett. **12**, 378(1964).

[13] N. Vasanti, Phys. Rev. D **13**, 1889(1976).

[14] R. H. Graham and S. Pakvasa, Phys. Rev. **140**, 1144 (1965).

[15] G. Farrar, Phys. Rev. D **4**, 212(1971).

[16] M. D. Scadron and L. R. Thebaud, Phys. Rev. D, **8**, 2190(1973).

[17] F. E. Close and H. R. Rubinstein, Nucl. Phys. B, **173**, 477(1980).

[18] M. B. Gavela *et al*, Phys. Lett. **101B**, 417(1981).

[19] K. G. Rauh, Z. Phys. C **10**, 81(1981).

[20] M. D. Scadron and M. Visinescu, Phys. Rev. D **28**, 1117(1983).

[21] G. Nardulli, Nuovo Cimento **100A**, 485(1988).

[22] F. J. Gilman and M. B. Wise, Phys. Rev. D **19**, 976(1979).

[23] Ya. I. Kogan and M. A. Shifman, Yad. Fiz. **38**, 1045(1983) [Sov. J. Nucl. Phys. **38**, 628(1983)].

[24] Lo Chong-Huah, Phys. Rev. D **26**, 199(1982).

[25] A. N. Kamal and Ramesh C. Verma, Phys. Rev. D **26**, 190(1982).

[26] R. C. Verma and Avinash Sharma, Phys. Rev. D **38**, 1443(1988).

[27] A. I. Vainshtein, V. I. Zakharov and M. A. Shifman, Pis'ma Zh. Eksp. Teor. Fiz **22**, 123(1975) [Sov. Phys. JETP Lett. **22**, 55(1975)].

[28] M. A. Shifman, A. I. Vainshtein and V. I. Zakharov, Nucl. Phys. B **120**, 316(1977).

[29] A. I. Vainshtein, V. I. Zakharov and M. A. Shifman, Zh. Eksp. Teor. Fiz. **72**, 1275(1977) [Sov. Phys. JETP **45**, 670(1977)].

[30] F. J. Gilman and M. B. Wise, Phys. Lett. B **83**, 83(1979).

[31] B. Guberina and R. D. Peccei, Nucl. Phys. B **163**, 289(1980).

[32] S. G. Kamath, Nucl. Phys. B **198**, 61(1982).

[33] J. O. Eeg, Z. Phys. C **21**, 253(1984).

[34] M. K. Gaillard, X. Q. Li and S. Rudaz, Phys. Lett. B **158**, 158(1985).

[35] C. Goldman and C. O. Escobar, Phys. Rev. D **40**, 106(1989).

[36] V. M. Khatsymovsky, Yad. Fiz. **45**, 181(1987) [Sov. J. Nucl. Phys. **45** 116(1987)], Erratum, Yad. Fiz. **46**, 1312(1987) [Sov. J. Nucl. Phys. **46**, 768(1987)].

[37] V. M. Khatsymovsky, Yad. Fiz. **46**, 896(1987) [Sov. J. Nucl. Phys. **46** 496(1987)].

[38] I. I. Balitsky, V. M. Braun and A. V. Kolesnichenko, Nucl. Phys. B **312**, 509(1989).

[39] P. Żenczykowski, Phys. Rev. D **44**, 1485(1991).

[40] M. A. Ahmed and G. G. Ross, Phys. Letts. B **59**, 293(1975).

[41] M. A. Shifman, A. I. Vainshtein and V. I. Zakharov, Phys. Rev. D **18**, 2583(1978).

[42] G. Bunce *et al*, Phys. Rev. Letts. **36**, 1113(1976).

[43] L. G. Pondrom, Phys. Reports **122**, 57(1985).

[44] C. Wilkinson *et al*, Phys. Rev. Letts. **58**, 855(1987).

[45] C. Ankenbrandt *et al*, Phys. Rev. Letts. **51**, 863(1983).

[46] C. Wilkinson *et al*, Phys. Rev. Letts. **46**, 803(1981).

[47] V. W. Hughes, P. Huber and K. P. Meyer, editors, Proceedings of the International Symposium on Polarization Phenomena of Nucleons, Helv. Phys. Acta Suppl. VI 436(1960).

[48] T. R. Cardello *et al*, Phys. Rev. D **32**, 1(1985).

[49] A. Denisov *et al*, *Performance of the E715 Transition Radiation Detector*, Proceedings of Santa Fe Meeting, World Scientific Publishing Co. Pte. Ltd. 358(1984).

[50] Lecroy Nuclear Products Catalog (1989).

[51] S. Hansen and S. Bracker, *Smart Camac Controller (SCC) Specifications*, Fermilab HN0063 (1987).

[52] S. Hansen *et al*, IEEE Transactions on Nuclear Science, **NS-34**, 1003(1987); Fermilab PN333 (1987).

[53] M. Bernett *et al*, *Smart Crate Controller Operating System Users Reference Guide*, Fermilab PN0314 (1988).

[54] M. Bernett *et al*, *Software for the Fermilab Smart Crate Controller*, Fermilab PN0330 (1987).

[55] *VME Readout Buffer (RBUF) Specifications*, Fermilab HN0082, (1989).

[56] R. Vignoni *et al*, *Fermilab Fast Parallel Readout System for Data Acquisition*, Fermilab PN331 (1987).

[57] *ACP68020 CPU Module 68KCPU*, Fermilab HN0071, (1986).

[58] *ACP User's Guide for Utilities*, Fermilab GA0002, (1987).

[59] P. Gouffon *History of E761 Alignments*, internal unpublished memorandum, H-note 494 (1 July 1991).

[60] T. Dubbs *TRD, WT Alignment Procedure*, internal unpublished memorandum, H-note 504 (29 July 1991).

[61] Particle Data Group, Phys. Lett. B **239**, III.22(1990).

[62] P. S. Cooper *et al*, Proceedings of the High Energy Spin Physics, Brookhaven National Laboratory, American Institute of Physics, 102(1982).

[63] A. Vorobyov and N. Kuropatkin *Some Ideas about building the TRD Algorithm*, internal unpublished memorandum, H-note 515 (18 September 1991).

[64] R. Brun *et al*, *GEANT 3*, Fermilab PM0062 (1987).